RIGA TECHNICAL UNIVERSITY

Vsevolod Burenin

RESEARCH, DEVELOPMENT, AND EVALUATION OF A CONTROL SYSTEM FOR ELECTRIC TRACTION DRIVES IN RAILWAY APPLICATIONS

Doctoral Thesis

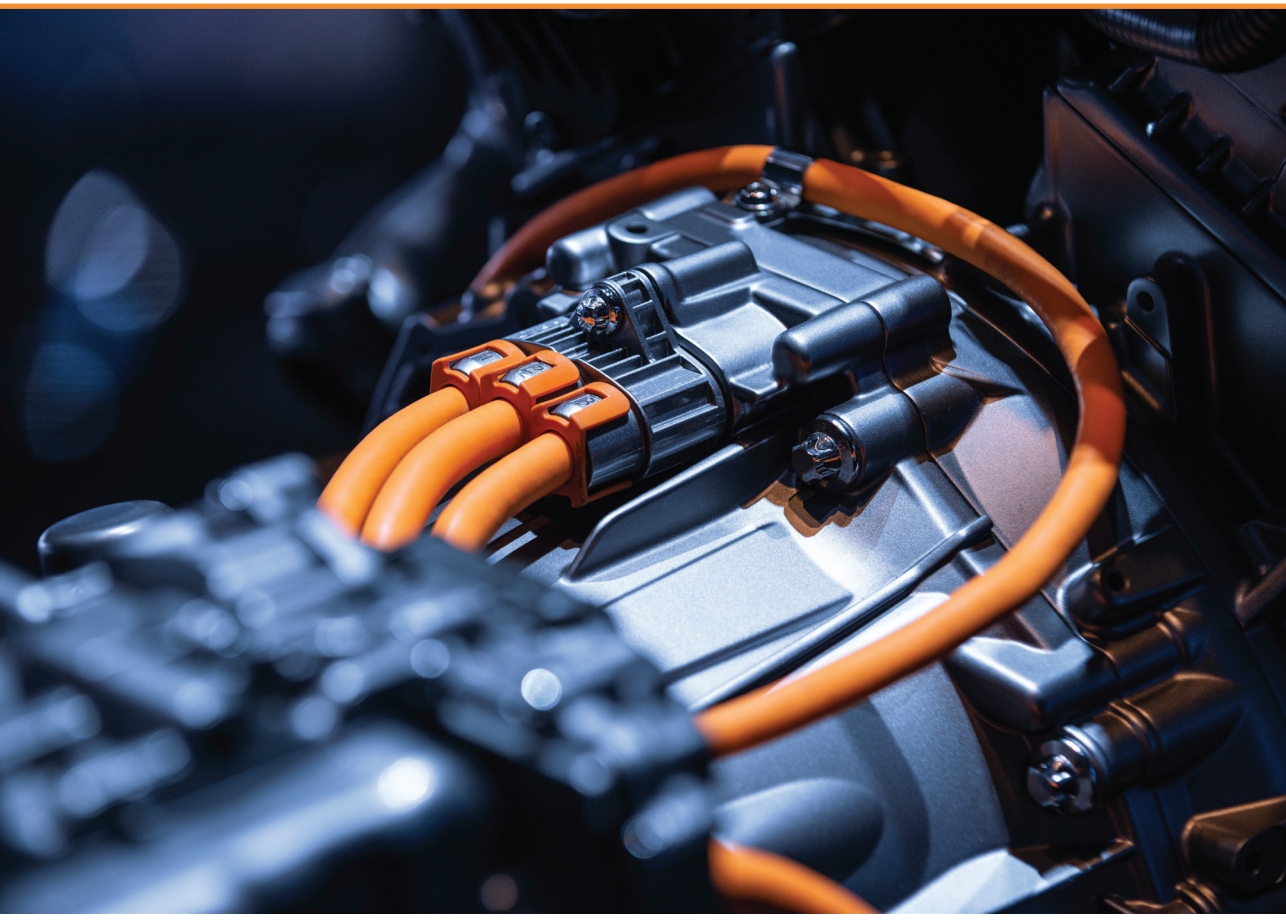

RTU Press
Riga 2025

RIGA TECHNICAL UNIVERSITY
Faculty of Computer Science, Information Technology and Energy
Institute of Industrial Electronics, Electrical Engineering and Energy

Vsevolod Burenin
Doctoral Student of the Study Programme "Computerized Control of Electrical Technologies"

RESEARCH, DEVELOPMENT, AND EVALUATION OF A CONTROL SYSTEM FOR ELECTRIC TRACTION DRIVES IN RAILWAY APPLICATIONS

Doctoral Thesis

Scientific supervisor
Professor Dr. sc. ing. OSKARS KRIEVS

RTU Press
Riga 2025

Abstract

The PhD thesis is titled “Research, Development, and Evaluation of a Control System for Electric Traction Drives in Railway Applications”. This PhD thesis aims to develop and validate a control system for railway traction electric drives using a downscaled laboratory prototype based on a 2-level inverter. The primary objective is to create a control system incorporating a low switching frequency hybrid pulse-width modulation (PWM).

Chapter 1 introduces the pre-programmed PWM, with a detailed focus on selective harmonic elimination PWM (SHE PWM). It outlines the principles of SHE and derives a mathematical approach to determine switching angles for harmonic elimination. The chapter concludes by presenting the advantages and disadvantages of the optimized algorithm in solving the SHE/SHM problem.

Chapter 2 provides a step-by-step methodology for developing the control system for railway applications. It covers the selection of parameters for the electric multiple unit (EMU), traction motor, and power converter, followed by the development of the hybrid PWM module, the implementation of a fundamental current hybrid observer, and the design of the control system.

Chapter 3 simulates the developed traction electric drive in Simulink under static and dynamic operating conditions, as well as with a model of an EMU. It highlights the advantages of SHE over synchronous PWM in low switching frequency regimes, focusing on total harmonic distortion (THD), weighted total harmonic distortion (WTHD), and power module losses. Additionally, it examines the differences between SHE solutions.

Chapter 4 describes the laboratory setup and the process of downscaling the developed model for practical testing. It includes static and dynamic tests, comparing THD, WTHD, and induction motor losses across different modulation and operational regimes.

The Doctoral Thesis has been written in English. It consists of an Introduction, 4 chapters, Conclusions, 83 figures, 56 tables, and 4 appendices; the total number of pages is 169, including appendices. The Bibliography contains 108 titles.

Anotācija

Šīs doktora disertācijas nosaukums ir “Research, Development, and Evaluation of a Control System for Electric Traction Drives in Railway Applications”. Darba uzdevums ir izstrādāt un verificēt dzelzceļa vilces piedziņas vadības sistēmu, izmantojot samazināta mēroga divu līmeņu invertora laboratorijas prototipu. Primārais darba mērķis ir radīt vadības sistēmu ar zemas komutācijas frekvences hibrīdu impulsa platuma modulāciju (PWM).

Darba pirmajā nodaļā ir iztirzāti PWM algoritmi īpašu uzmanību veltot selektīvās harmonisko komponenšu novēršanas PWM metodēm. Tajā ir izklāstīti selektīvās harmonisko komponenšu novēršanas PWM pamatprincipi un dota matemātiskā metode harmonisko komponenšu novēršanas komutācijas leņķu noteikšanai. Nodaļas noslēgumā tiek prezentētas optimizētā algoritma priekšrocības un trūkumi selektīvās harmonisko komponenšu novēršanas PWM problēmas risināšanā.

Darba otrajā nodaļā ir dota metodika dzelzceļa vilces piedziņas vadības sistēmas izstrādei. Tajā aplūkota elektrovilciena, tā vilces dzinēju un enerģijas pārveidotāju parametru izvēle, kā arī hibrīdā IPM moduļa izstrāde, strāvas pamata harmoniskās komponentes novērotāja un vadības sistēmas izveide.

Trešā nodaļa ir veltīta izstrādātās vilces piedziņas sistēmas un visa elektrovilciena datormodelēšanai “Simulink” vidē statiskos un dinamiskos darba režīmos. Tajā ir izceltas selektīvās harmonisko komponenšu novēršanas PWM priekšrocības salīdzinājumā ar sinhrono PWM zemu komutācijas frekvenču režīmos, īpašu uzmanību veltot harmoniskajiem kropļojumiem un enerģijas pārveidotāja zudumiem. Nodaļā ir analizētas atšķirības starp dažādiem selektīvās harmonisko komponenšu novēršanas PWM risinājumiem.

Ceturtajā nodaļā ir aplūkots izmantotais laboratorijas aprīkojums un samazināta mēroga sistēmas prototipa izstrāde eksperimentālajai testēšanai. Nodaļā ir ietverti sistēmas statisko un dinamisko pārbaužu rezultāti, salīdzinot harmoniskos kropļojumus un asinhronā dzinēja zudumus dažādos modulācijas un darba režīmos.

Promocijas darbs ir uzrakstīts angļu valodā, tajā ir ievads, četras nodaļas, secinājumi, literatūras saraksts, 83 attēli, 56 tabulas, četri pielikumi, kopā 169 lappuses, ieskaitot pielikumus. Literatūras sarakstā ir 108 nosaukumi.

Preface

This PhD thesis was conducted as part of the European project Nr. 1.1.1.1/20/A/068 titled “Development of Electric Train Electrical Equipment Set with Improved Characteristics” (Latvian: “Elektrovilciena elektroaprīkojuma komplekta izstrāde ar uzlabotām īpašībām”). The project spanned from January 1, 2021, to November 30, 2023.

The support from this project was instrumental in shaping the final direction of the research. It provided the necessary resources and a collaborative environment that were crucial for the completion of this PhD thesis, even beyond the official project end date.

Acknowledgments

I would like to express my deepest gratitude to my scientific supervisor, Prof. Dr. sc. ing. Oskars Krievs, for his unwavering support, invaluable comments, and positive attitude throughout my entire PhD research.

I am profoundly thankful to my colleague and scientific advisor, Dr. sc. ing. Jaroslavs Zarembo, for his continued support and extensive conceptual and scientific guidance during both my master's thesis and PhD thesis.

I would also like to acknowledge JSC “Rīgas elektromašīnbūves rūpnīca,” especially Dr. sc. ing. Olegs Sliskis, for their continued support and for providing invaluable data and insights into the railway industry.

In the preparation of this PhD thesis, the capabilities of ChatGPT (GPT-4o) by OpenAI were utilized to improve the quality of the text. The AI tool assisted in refining the language and checking for grammar and style. This acknowledgment ensures transparency in the use of technology.

Table of Contents

List of Figures

List of Tables

List of Abbreviations

DUT – device under test

EMU – electric multiple unit

FOC – field-oriented control

FPGA – field programmable gate array

HIL – hardware-in-the-loop

IGBT – insulated gate bipolar transistor

LUT – look-up table

MPC – model predictive control

OPP – optimized pulse pattern

PPWM – pre-programmed pulse width modulation

PWM – pulse width modulation

SHE – selective harmonic elimination

SHM – selective harmonic mitigation

SPWM – sinusoidal pulse width modulation

SVPWM – space vector pulse width modulation

THD – total harmonic distortion

V/f control – volt-hertz/scalar control

VSI – voltage source inverter

WTHD – weighted total harmonic distortion

General description of the Thesis

Research relevance

Railway traction electric drives are used in widely different types of electrification systems, with most of them being attributed to the high-power medium voltage category. Most of these systems are customized to specific types or series of rail transport, with traction electric motor and power converter being two of the most important components.

Traction electric motors enable the mechanical propulsion of the train. Currently, the most widely used type of motor is the squirrel cage induction motor [1], [2], [3], although there is increasing adoption of permanent magnet synchronous machines [4]. Leading producers of traction electric motors for the railway industry include TSA, ABB, Mitsubishi, Siemens, Alstom, and Škoda. In Baltic countries, Latvian factory JSC "Rīgas elektromašīnbūves rūpnīca" stands as a prominent producer of traction electric motors for trains, trams, and subways.

Power converters are another fundamental component of traction electric drives. They are used to ensure power efficiency and density, controllability and stability of electric drive operation. Power converters heavily rely on power semiconductors. Currently, insulated gate bipolar transistors (IGBTs) dominate the space of traction electric drives, utilized extensively across a spectrum of power levels from a few kilowatts to several megawatts [4]. Despite significant development and investment in silicon carbide (SiC) semiconductor technologies, SiC semiconductors for medium to high-power applications are still in the developmental phase. Recently, a SiC module prototype for a frequency converter with a rated voltage of 10 kV was reported by Cree/Wolfspeed as part of a project sponsored by the U.S. Department of Energy for use with MW class motors [5], [6].

Currently, the most commonly used IGBTs in the railway industry have blocking voltages of 3300 VDC [7], 4500 VDC and 6500 VDC [8], [9], with some solutions utilizing 1700 VDC [3]. SiC devices have currently proven reliability for commercial automotive use and are available in both pure SiC and hybrid configurations with a 1200 VDC blocking voltage [10], [11], [12], while the 1700 VDC variants are just entering the market. These devices are increasingly being used in light vehicle applications, such as electric cars [13], [14], [15]. The introduction of high-power applications for railways is underway, with the expectation that SiC power semiconductors with a 3300 VDC blocking voltage will start entering the market between 2026 and 2030 [12], [14], [15].

Currently, the primary producers of power IGBTs for the railway industry include ABB, Infineon, Mitsubishi Electric, Hitachi, and Fuji Electric, among others [4].

Over the years, technological advancements in the field of power semiconductors improved the controllability and stability of power semiconductors within a specific temperature range. However, switching and ON-state losses at high powers still result in excessive junction temperatures that lead to reduced service life and reliability of the device. Therefore, it is common practice to employ low switching frequencies in rail traction systems to reduce IGBT switching losses, thereby enhancing their life expectancy [16], [17]. 2-level topology, commonly used in high-power applications, typically limits the switching frequency of the converter to a range from a few hundred hertz up to 1 kHz [8], [18], [19], [20], [21], [22], whereas the 3-level topology is reported to operate up to 2 kHz [8], [23]. The choice of topology depends on various parameters, with no single option deemed universally superior.

Operating at reduced frequencies presents its own set of challenges, including increased harmonic distortion in the stator current. This is particularly undesirable as higher current harmonics can significantly increase losses in the induction motor [24], [25]. Additionally, some countries impose limits on the permissible values of harmonics in a DC catenary, where applicable [26].

To mitigate harmonic distortion while maintaining a low switching frequency, specialized modulation techniques are employed. Since their inception, pulse width modulation (PWM) techniques have undergone rapid evolution. General PWM techniques have been extensively studied and compared for induction motor drives. These techniques aim to achieve better DC bus voltage utilization, optimize converter harmonics and losses, and enhance the output frequency spectrum of three-phase converters and other indicators [16].

There exists a multitude of PWM approaches. Commonly utilized methods include sinusoidal PWM (SPWM), space vector PWM (SVPWM) and discontinuous PWM, among others. However, there are also pre-programmed PWM techniques, such as selective harmonic elimination (SHE), selective harmonic mitigation (SHM) PWM, and optimized pulse pattern (OPP). These pre-programmed techniques are aimed at improving the current waveform at very low switching frequencies, enabling the elimination or minimization of predetermined harmonics while maintaining the fundamental current harmonic at the predefined level of the modulation index. Among these techniques, selective harmonic elimination (SHE) stands out as the most well-known strategy [27], [26], [16], [19].

The prevailing approach to modulation in railway traction electric drives involves a combination of asynchronous and synchronous PWM at lower frequencies, transitioning to variations of SHE/SHM approaches, and potentially shifting to square wave modulation at higher speeds if necessary. This amalgamation of modulation techniques is referred to as a hybrid PWM. An illustrative example of the hybrid PWM mode transitions is depicted below.

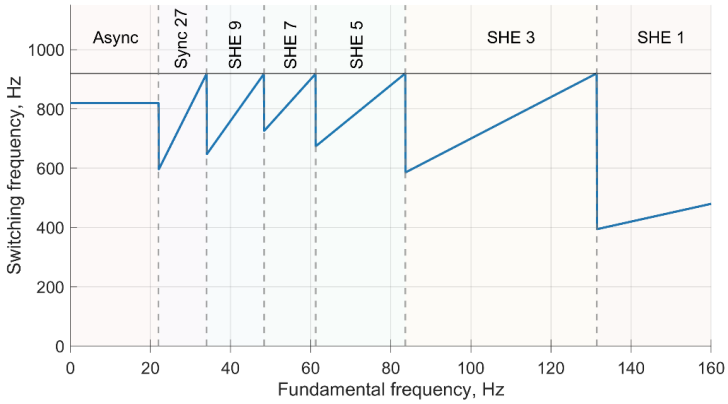

Visualization of the Hybrid PWM mode transitions

Similarly, pre-programmed PWM approaches have also been proposed for use in the automotive industry, particularly when the traction motor has numerous pole pairs, resulting in a fundamental current frequency reaching values of 1200 Hz, while the switching frequency limit is 10 kHz [28], [29]. At these values the ratio of switching to fundamental frequency also falls below the desirable minimum value of 10.

The primary objective of this research is to develop a control system for a traction induction motor, incorporating a low switching frequency hybrid PWM. The proposed system will be rigorously tested on a downscaled laboratory prototype to assess its performance and stability, offering a comprehensive evaluation within the context of railway applications.

Aim, research methods, and novelty of the Thesis

The aim of the research

Developing and validating a control system for railway traction electric drives using a downscaled laboratory prototype based on a 2-level inverter.

Research tasks

1. Investigate control and PWM strategies applicable to railway applications.
2. Develop a modulation algorithm based on the selected PWM strategy.
3. Design the traction drive field-oriented control system, integrating the chosen PWM strategy.
4. Create and simulate an electric drive model to analyse expected operational regimes.
5. Develop a testing setup for the control system.
6. Conduct tests on the control system using a 2-level inverter in a downscaled laboratory setup.
7. Analyse and evaluate the results of laboratory testing.

Research tools and methods

- MATLAB was used in this study for the calculation of SHE-PWM solutions. It played a vital role in processing recorded data, conducting thorough data analysis, and creating visualizations to support the findings.
- Simulink was used for the creation and simulation of the electrical drive model. Both built-in library blocks and custom-developed MATLAB functions were used in a Simulink model.
- MS Excel was used as a storage for traction characteristic reference and equivalent circuit reference as part of model initialization. MS Excel was also used for miscellaneous intermediary calculations.
- RT-LAB was used for the adaptation of the developed control system for deployment to the OPAL-RT OP4510.
- A variety of laboratory equipment was used during the development process, testing and experimental verification in different configurations. The laboratory setup is described during work.

Scientific novelties

- Development of an optimized Newton–Raphson-based technique for solving the selective harmonic elimination and selective harmonic mitigation problem for both 2-level and 3-level inverters, improving the accuracy and convergence speed.
- Modification and enhancement of a fundamental current hybrid observer for railway traction drive applications, accompanied by the analysis of its robustness and stability. These modifications extend the work by Prof. J. Holtz [30].
- Introduction and detailed description of a control system that seamlessly transitions between modulation regimes while analysing practical dynamic limits.
- Development of a fully functional control system with low switching frequency specifically designed for railway traction drive applications. The system demonstrates good performance achieved through the implementation of a novel control algorithm.
- Numerical comparison of power module and motor losses in synchronous PWM and selective harmonic elimination PWM.

Hypotheses

- The train traction power converter is hypothesized to reliably operate at a very low switching frequency with a field-oriented control system. This operation is expected to maintain an acceptable level of stator current harmonic distortion while ensuring that the power module losses remain within acceptable limits.
- Selective harmonic elimination PWM is hypothesized to reduce power module and motor losses in comparison to synchronous PWM when subject to a low ratio of switching to fundamental frequencies.

Approbation of research results

Scientific articles and conference papers

1. K. Gulbis, U. Brakanskis, E. Kamolins, M. Gorobecs, A. Potapovs, K. Sejejs, J. Zarembo, and V. **Burenin**, "Analysis of Test Results of the Developed Synchronous Reluctance Motor for Public Transport Application", Latvian Journal of Physics and Technical Sciences, vol. 59, no. 4, 2022, pp. 36–52.
2. A. Suzdalenko, **V Burenin,** J. Zarembo, J. Zakis,. Modelling of Bidirectional Three-Phase Four-Wire Three-Level NPC MLC under Single-Loop Current Sensorless Control. Energies 2023, 16, 4599.
3. **V. Burenin**, J. Zarembo, G. Kobenkins, and O. Krievs, "Implementation of Hybrid PWM with Smooth Transitions between Modulation Modes for Railway Traction Field-Oriented Control System", 2023 IEEE 64th International Scientific Conference on Power and Electrical Engineering of Riga Technical University (RTUCON), Riga, Latvia, 2023, pp. 1–7.
4. **V. Burenin**, J. Zarembo, O. Krievs, and L. Ribickis, "Comparison of Synchronous Reluctance Motor and Induction Motor Efficiency Maps for Traction Application," 2021 IEEE 62nd International Scientific Conference on Power and Electrical Engineering of Riga Technical University (RTUCON), Riga, Latvia, 2021, pp. 1–5.
5. **V. Burenin**, J. Zarembo, A. Žiravecka and L. Ribickis, "Model of Laboratory Test Bench Setup for Testing Electrical Machines," 2020 IEEE 61st International Scientific Conference on Power and Electrical Engineering of Riga Technical University (RTUCON), Riga, Latvia, 2020, pp. 1–5.
6. E. Kamolins, M. Gorobecs, **V. Burenin**, K. Gulbis, A. Potapovs, U. Brakanskis, J. Zarembo, K. Sejejs, "180 kW Synchronous Reluctance Motor for Mass Transit Electrical Traction Application," 2021 23rd European Conference on Power Electronics and Applications (EPE'21 ECCE Europe), Ghent, Belgium, 2021, pp. 1–8.
7. G. Kobenkins, M. Marinbahs, A. Bizans, **V. Burenin,** and O. Sliskis, "Evaluation of the Strength of Traction Geared Motor Units by Permissible Stresses and the Level of Vibration Activity," 2022 International Conference on Electrical, Computer and Energy Technologies (ICECET), Prague, Czech Republic, 2022, pp. 1–6.
8. G. Kobenkins, M. Marinbahs, A. Bizans, N. Rilevs, **V. Burenin,** and O. Sliskis, "Carrying Out of Strength Control of Mutual Loaded Traction Geared Motor Boxes as a Part of

Industrial Tests," 2022 9th International Conference on Electrical and Electronics Engineering (ICEEE), Alanya, Turkey, 2022, pp. 185–189.

9. G. Kobenkins, M. Marinbahs, **V. Burenin**, J. Zarembo, A. Bizans, and O. Sliskis, "Determination of the Level of Own Vibration of Geared Motor Boxes in Industrial Conditions," 2021 IEEE 62nd International Scientific Conference on Power and Electrical Engineering of Riga Technical University (RTUCON), Riga, Latvia, 2021, pp. 1–6.
10. G. Kobenkins, M. Marinbahs, **V. Burenin**, J. Zarembo, and O. Sliskis, "Carrying Out of Strenght Tests of Geared Motor Box as Part of a Frequency-Controlled Traction Electric Drive," 2021 17th Conference on Electrical Machines, Drives and Power Systems (ELMA), Sofia, Bulgaria, 2021, pp. 1–4.

1. Description of the Pre-Programmed PWM

The software of the power traction converter is a complex, interconnected system consisting of control systems, a PWM modulator, communication protocols, various service tools, and more. The PWM technique within the PWM modulator is a critical component, with the two most prominent methods being carrier-based SPWM and SVPWM [27]. However, in high-power applications such as those in railway traction electric drive systems, the switching frequency must be constrained to low values to prevent overheating and premature failure of high-power semiconductors, as the high-power semiconductors have high switching losses at elevated frequencies.

Reducing the switching frequency is a feasible strategy, but the ratio of the switching frequency to the fundamental frequency ($m_f = \frac{f_{sw}}{f_1}$) for SPWM and SVPWM typically does not drop below $m_f = 9$ [31], [32]. Considering that induction motors in traction applications usually have two or three pole pairs with a fundamental frequency reaching 160–180 Hz, this limitation means the switching frequency exceeds 1000 Hz. Yet, usually, the switching frequency for high-power semiconductors is limited to a few hundred hertz up to 1 kHz [8], [18], [19], [20], [21].

A low m_f ratio can degrade the current regulating performance of variable frequency inverters, potentially leading to instability [33]. Moreover, with conventional PWM, the proximity of harmonic orders to the fundamental frequency necessitates bulky filtering devices and can increase losses and torque oscillations in the induction motor, especially prominent for harmonics less than the 10th order [24], [25].

These challenges necessitate specialized PWM techniques to limit or eliminate specific harmonics using a low switching frequency, thereby extending the life of the traction converter and reducing motor losses. The main method to limit switching frequency and keep a focus on the output harmonic spectrum is pre-programmed PWM (PPWM). Common variations are selective harmonic elimination (SHE), selective harmonic mitigation (SHM), a hybrid of SHE and SHM, and PPWM with optimized switching pulse patterns/sequences [17].

Distinct from conventional modulation strategies like SPWM and SVPWM, which are carrier based, PPWM instead utilizes gating signals (or switching angles) pre-calculated based on fundamental Fourier transformations and elimination of predetermined harmonics. These switching angles are calculated by solving a system of nonlinear equations offline and stored in a look-up table for use during operation [27]. This method's main advantage is the generation of higher quality current waveforms at low m_f values. However, it is primarily suited for low-dynamic power systems, such as trains in this case, due to the limited controller bandwidth [34].

Fig. 1.1 shows the classification of common PPWM types and formulations.

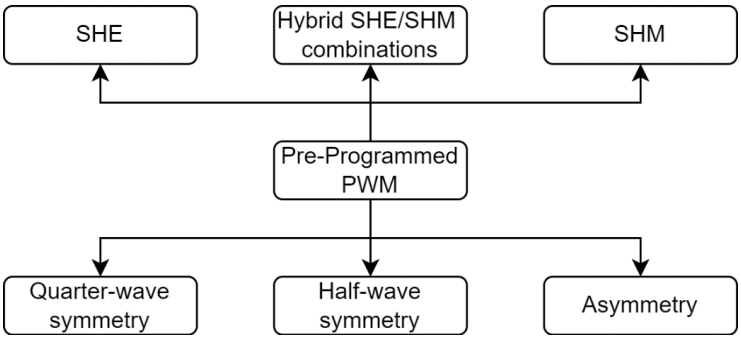

Fig. 1.1. Classification of common PPWM types and formulations.

Selective harmonic elimination PWM (SHE-PWM) is the most widely used approach, which eliminates pre-defined harmonics fully from output waveform by switching at specific points in time.

Selective harmonic mitigation PWM (SHM-PWM) is very similar in nature to the SHE-PWM. In general it is a variation of SHE-PWM, where not specific harmonics are eliminated, but overall THD is limited, or specific harmonics have their upper limit different from zero [16], [18], [35]. This method is reported to be used to limit grid codes in accordance with regulations [18], [26], [35], [36]. In other literature a variation of selective harmonic mitigation method is called optimized pulse pattern (OPP-PWM), introduced and mainly used by the ABB [37], [38], [39].

The hybrid SHE/SHM combination is used when there is a possibility to switch between these two methods, or if there is another goal besides maintaining the current waveform. It was reported to be used in a 3-phase 3-level 4-leg inverter for mitigation of harmonics and dc-link voltage balancing [40], [41], and with NPC 3-phase 3-level inverter [42].

For this research, SHE-PWM was selected which prioritizes the elimination of the lowest harmonic, as harmonics closest to fundamental have the highest effect on current quality and motor losses [24], [25].

The selective harmonic elimination as a technique of inverter or rectifier modulation gained more attention after the study by Patel and Hoft [43], [44]. Due to the limited technological capabilities of the power electronics of that time, the described method was difficult to implement and develop. The progress in technology of high-power semiconductor switches, digital signal processing, and control algorithms for hardware implementation have revitalized interest in SHE [17], [26].

This chapter aims to detail the concept and mathematical framework underlying the SHE PWM technique.

1.1. Principle of selective harmonic elimination

The principle of selective harmonic elimination (SHE) is applied to the output of each phase leg of an inverter, which can be switched an arbitrary number of times per cycle to adjust the fundamental voltage component applied to the load and to minimize the harmonic content of the output voltage waveform. As depicted in Fig. 1.2 shows a generalized output waveforms with N notches per half cycle (equating to 2N+1 switching events) can be achieved. It is crucial to note that switching events are presupposed to occur at half cycle points—0°, 180°, and 360°—stemming from basic square-wave switching and are not considered part of the notching process.

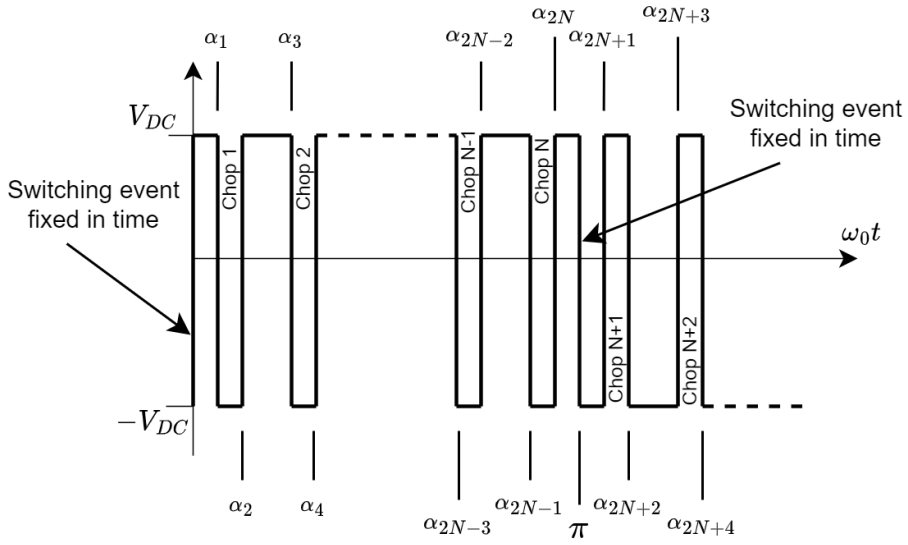

Fig. 1.2. Generalized output waveform of inverter.

When N is odd, a notch of opposite polarity to the desired fundamental peak invariably appears at the centre of each half cycle, symmetrically around the 90° and 270° points of the fundamental waveform. Such configurations lead to impractical solutions, necessitating the use of an even N for viable applications [32].

With a scenario devoid of notches, the resulting square wave inherently comprises all odd harmonics (h = 1, 3, 5, 7, 9, ...). Furthermore, in the context of a three-phase inverter with the load connected in a wye configuration, it's pertinent to highlight that only non-triplen harmonics (harmonics that are not multiples of three) will induce currents in the load [32].

1.2. Mathematical basis of the pre-programmed PWM

In scientific and technical literature, the formulations of selective harmonic elimination PWM (SHE-PWM) are based on decomposing voltage PWM waveforms using Fourier series expansion. The formulation of SHE-PWM typically depends on the characteristics of a given waveform, such as unipolar, bipolar, stepped, multilevel, symmetrical, and asymmetrical waveforms. These features are equally important in analysing and determining the complexity and form of the solution space [17].

This section summarizes the mathematical description of SHE-PWM calculation for a traction electric drive with an induction motor and a 3-phase, 2-level voltage source inverter. In this scenario, three types of symmetry can be assumed: quarter-wave, half-wave symmetry, and a non-symmetrical waveform. The function describing these waveform types can be represented as a Fourier series, expressed by the following relation [16], [26], [43]:

$$f(\omega t) = a_0 + \sum_{n=1}^{\infty} [a_n \sin(n\omega t) + b_n \cos(n\omega t)], \tag{1.1}$$

where a_0, a_n, and b_n are the coefficients described by Euler's formulas.

$$a_0 = \frac{1}{2\pi} \int_0^{2\pi} f(\omega t) d\omega t, \tag{1.2}$$

$$a_n = \frac{1}{\pi} \int_0^{2\pi} f(\omega t) \sin(n\omega t)\, d\omega t, \tag{1.3}$$

$$b_n = \frac{1}{\pi} \int_0^{2\pi} f(\omega t) \cos(n\omega t)\, d\omega t. \tag{1.4}$$

For the simplification of solutions, half-wave and quarter-wave symmetry simplify the Fourier representation of the waveform by eliminating even harmonics, $a_n = 0$ and $b_n = 0$ for even n.

To achieve half-wave symmetry, a function describing the waveform must satisfy the condition:

$$f(\omega t) = -f(\omega t + \pi). \tag{1.5}$$

For quarter-wave symmetry, both the condition for half-wave symmetry (1.5) and the following condition must be met:

$$f(\omega t) = f(\pi - \omega t). \tag{1.6}$$

For a waveform with quarter-wave symmetry, Fourier's series coefficients assume the following values:

$$a_n = \begin{cases} \frac{2U_{dc}}{n\pi}\left[1 + 2\sum_{i=1}^{N} (-1)^i \cos(n \cdot \alpha_i)\right], & \text{for odd } n \\ 0, & \text{for even } n \end{cases} \tag{1.7}$$

$$b_n = \begin{cases} 0, & \text{for odd } n \\ 0, & \text{for even } n \end{cases} \tag{1.8}$$

where U_{dc} is the DC-link voltage, N is the number of switching angles in a quarter period, α_i is the ith switching angle of an inverter's transistor, and n is the harmonic order.

It follows that in a wave symmetrical relative to $\pi/2$, only the a_n coefficient for odd harmonics has a non-zero value. In a symmetrical three-phase system, triplen harmonics of phase voltage are co-phasal and equal in magnitude. Thus, for a star-connected motor with an insulated neutral point, the phase voltages will cancel out the line-to-line voltage, and no line current of triplen harmonics will result. These assumptions and physical properties greatly simplify the solutions process, as in this case, the a_n coefficient is a relative value of harmonics amplitudes of output phase voltage of $n = 5, 7, 11, 13$ ... order [26].

Upon determining whether the obtained voltage waveform fulfils the conditions of a quarter-wave symmetry (1.5), (1.6) and consists of an N number of switching angles α in each quarter of a period, based on dependence (1.7), it is possible to create a system of N equations (1.9) [26].

$$\begin{cases} \frac{4}{n_1\pi}[1 - 2\cos(n_1\alpha_1) + 2\cos(n_1\alpha_2) - \cdots \pm 2\cos(n_1\alpha_N)] = M_1 \\ \frac{4}{n_2\pi}[1 - 2\cos(n_2\alpha_1) + 2\cos(n_2\alpha_2) - \cdots \pm 2\cos(n_2\alpha_N)] = 0 \\ \vdots \\ \frac{4}{n_N\pi}[1 - 2\cos(n_N\alpha_1) + 2\cos(n_N\alpha_2) - \cdots \pm 2\cos(n_N\alpha_N)] = 0 \end{cases}. \quad (1.9)$$

Each of the above-mentioned equations is used to fix an amplitude for a selected voltage harmonic. This set of equations for N switching angles allows for eliminating $N - 1$ voltage harmonics and determining the M_1 value of a basic component, defined by the relation:

$$M_1 = \frac{2 \cdot V_{ph}}{U_{dc}}, \quad (1.10)$$

where V_{ph} is the eligible amplitude of an output voltage basic component.

In Formula (1.9), Equations 2–N have their right sides compared to zero, which is equivalent to the application of the SHE method. If the right sides of a set of equations (1.9) are replaced by the vector of values of the selected harmonics, there is an opportunity to set values of the selected harmonics (SHM technique). Using the method of SHM gives a wide range of shaping opportunities for an inverter's output voltage harmonics and, consequently, the DC-link current harmonics spectrum [26].

1.3. Overview of solving algorithms for PPWM techniques

Finding feasible solutions for the PPWM methods is a critical task. Over the past few decades, scientists and research groups have made significant efforts to develop and enhance various solving algorithms. These efforts aim to find the unique optimal solution or multiple optimal solutions within

PPWM formulations, such as numerical methods, algebraic methods, and intelligent optimization methods. The classification of commonly used methods is presented in Fig. 1.3 [17].

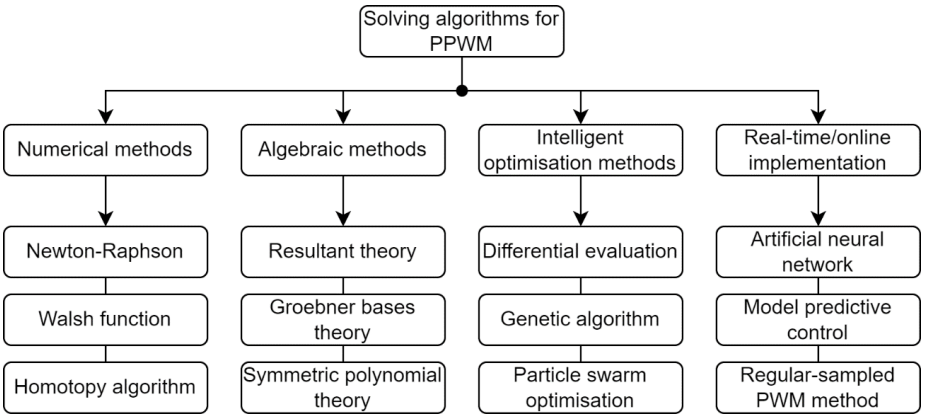

Fig. 1.3. Classification of PPWM solving algorithms and methods.

❖ **Numerical methods**

Normally there are two main factors to consider in solving PPWM with numerical methods: the iteration efficiency of algorithm and the determination of initial values for algorithm.

With advancements in computational power, iteration efficiency has become less critical. The determination of initial values has emerged as the primary challenge in solving PPWM formulations. An accurate estimate of the initial values can significantly ensure the convergence of the final solutions. However, while initial values may be predictable for output waveforms with a small number of switching angles, they become difficult to predict or ineffective for waveforms with a large number of switching angles [17].

❖ **Algebraic methods**

Algebraic methods offer a solution to the constraints posed by numerical methods, presenting viable solutions to the PPWM equations without the requirement for initial values. These methods leverage trigonometric identities to convert the nonlinear and transcendental PPWM equations into an equivalent set of polynomial equations. Subsequently, the derived theory is employed to compute the resulting system of polynomial equations, aiming to identify all feasible solutions for switching angles based on the given PPWM formulation.

There has been done extensive research employing different algebraic methods, such as resultant theory [45], Groebner bases theory [46] and symmetric polynomial theory [47] among others. A significant drawback of these methods is the increase in polynomial complexity as more harmonics are eliminated, leading to a heavier computational load [17].

❖ **Intelligent optimization methods**

Presently, an increasing number of researchers are exploring and embracing intelligent optimization methods to address PPWM problems. The PPWM problem can be reformulated as an optimization problem, aiming for minimization through both the fitness function and constraint functions. The popularity of intelligent optimization methods can be attributed to several factors such as reduced dependency on initial values and ease of understanding and implementation.

Advances in machine learning have simplified the understanding and implementation of these methods.

Research employing intelligent optimization methods, such as differential evaluation [48], genetic algorithm [49], particle swarm optimization methods [50], and grasshopper optimization algorithm [51] among other research. However, the real-time application of these methods faces challenges in ensuring the existence of a feasible solution. It remains unclear whether the inability to attain a feasible solution stems from the selection of algorithm parameters or the genuine absence of a valid solution for the PPWM equations [17].

❖ **Real-time/Online implementation**

Although many solution algorithms are based on offline computing, there is a growing demand for online/real-time solutions. Online implementation has been reported on microcontrollers and FPGA [52], [53], using artificial neural networks [54] and model predictive control [55] techniques.

For applications within the railway industry, offline solutions with precalculated solutions stored in lookup tables (LUTs) are often sufficient. For this research, the numerical Newton-Raphson method was chosen due to its extensive usage and detailed descriptions in the scientific literature, making it suitable for solving transcendental nonlinear systems of equations.

1.4. Development of solving algorithm

The numerical method for the solution of a set of nonlinear transcendental equations is based on the study [43] with several modifications, and is a use-case of a Newton–Raphson method.

1.4.1. Mathematical formulation

The system of nonlinear equations in N variables can be represented as

$$f_i(\alpha_1, \alpha_2, \dots, \alpha_N) = M \quad , i = 1,2, \dots, N, \tag{1.11}$$

where M is the vector of values of selected harmonics. Equations themselves are as shown in (1.9). Equation (1.11) is written in vector notation as

$$f(\alpha) = M, \tag{1.12}$$

where f and α are as shown below:

$$f = [f_1, f_2, \dots, f_N]^T, as\ N \times 1\ matrix,$$

$$\alpha = [\alpha_1, \alpha_2, \dots, \alpha_N]^T, as\ N \times 1\ matrix,$$

where N is the number of $f_1 \dots f_N$ are the switching angles allow for eliminating $N-1$ voltage harmonics, $f_1 \dots f_N$ are N equations to solve with trigonometric components for each α_i ith switching angle α.

Equation (1.12) can be solved by using a linearization technique, where the nonlinear equations are linearized about an approximate solution. The steps involved in computing a solution are as follows.

1) Guess a set of values for α; call them an initial guess,

$$\alpha^0 = [\alpha_1^0, \alpha_2^0, \dots, \alpha_N^0]^T. \tag{1.13}$$

2) Determine the values of a set of equations,

$$f(\alpha^0) = f^0. \tag{1.14}$$

3) Linearize (1.12) about α^0

$$f^0 + \left[\frac{\partial f}{\partial \alpha}\right]^0 d\alpha = M. \tag{1.15}$$

Where partial derivative is represented as

$$\left[\frac{\partial f}{\partial \alpha}\right]^0 = \begin{bmatrix} \frac{\partial f_1}{\partial \alpha_1} & \frac{\partial f_1}{\partial \alpha_2} \cdots & \frac{\partial f_1}{\partial \alpha_N} \\ \frac{\partial f_2}{\partial \alpha_1} & \frac{\partial f_2}{\partial \alpha_2} \cdots & \frac{\partial f_2}{\partial \alpha_N} \\ & \vdots & \\ \frac{\partial f_N}{\partial \alpha_1} & \frac{\partial f_N}{\partial \alpha_2} \cdots & \frac{\partial f_N}{\partial \alpha_N} \end{bmatrix}.$$

Evaluated at α^0 and $d\alpha = [d\alpha_1, d\alpha_2, \dots, d\alpha_N]^T$

4) Solve (1.15) for $d\alpha$

5) Repeat 1) – 4) using, as improved guesses,

$$\alpha^1 = \alpha^0 + d\alpha. \tag{1.16}$$

The process is repeated until (1.12) is satisfied to the desired degree of accuracy. If the previous method converges, it will give a solution to (1.12). In case of divergence from the initial guess, it is necessary to make a new initial guess. The process is a trial-and-error method. The correct solution must satisfy the condition stated below:

$$0 < \alpha_1 < \alpha_2 < \cdots < \alpha_N < 90°. \tag{1.17}$$

This condition is crucial as it ensures physical feasibility and non-singularity of the solution.

In solving a set of nonlinear equations numerically, the primary concern is the convergence of the method used. Unlike solving a single nonlinear equation, where many methods exist for obtaining a priori information on the root's location, there is no single approach for determining an initial guess

in a system of nonlinear equations. Without a way to obtain a priori information, convergence becomes an issue, as the solving process often leads to divergence. It is usually a trial-and-error process, and no general method exists that can guarantee convergence to a solution [43].

1.4.2. Computer algorithm for solving a system of nonlinear equations

Let $n_1, n_2, \dots, n_N$ be the N harmonics to be set to be eliminated or set to a predefined level, expressed as a vector $M = [M_1, M_2, \dots, M_N]^T$ [43], [26]. Then a set of equations as in (1.9) are created. While the derivative matrix, $\partial f / \partial \alpha$ of (1.15) is obtained by partial derivation from (1.9).

$$\frac{\partial f}{\partial \alpha} = \begin{bmatrix} 2n_1 \sin n_1\alpha_1 - 2n_1 \sin n_1\alpha_2 \cdots \pm 2n_1 \sin n_1\alpha_N \\ 2n_2 \sin n_2\alpha_1 - 2n_2 \sin n_2\alpha_2 \cdots \pm 2n_2 \sin n_2\alpha_N \\ \vdots \\ 2n_N \sin n_N\alpha_1 - 2n_N \sin n_N\alpha_2 \cdots \pm 2n_N \sin n_N\alpha_N \end{bmatrix}. \tag{1.18}$$

The elements of the last column of the matrix in (1.18) are positive if M is odd, and negative if it is even. Using the described numerical method the computer MATLAB script was created.

To solve the N-linear equations (1.15), the $N \times N$ matrix of (1.18) must be non-singular. This condition is violated if any one of $\alpha_1, \alpha_2, \dots, \alpha_N$ is equal to zero, assuming the domain of the solution is the closed interval $(0, \pi/2)$. Also, if any two α are equal, two columns of the matrix are identical, except for the sign, in case they are opposite. The rank of the matrix in that case is reduced to $N - 1$, and the matrix is singular. The condition of (1.17) insures the non-singularity of the matrix as well as a meaningful solution to (1.9).

1.4.2.1. Code structure and overall functionality

The program to find solutions consists of two functions:

- *Main function*: This script sets up and solves the SHE problem for a specified set of harmonic orders to be eliminated. The user can specify the modulation index (or indices) for which the solutions are sought. The script uses the Newton-Raphson method, a numerical technique for finding the roots of a function, to iteratively solve the system of nonlinear equations that arises from the SHE problem. Key parameters such as the maximum number of iterations, precision, and the total number of runs can be adjusted to control the solution's accuracy and computational effort.
- *Calculation of function values and partial derivatives function*: This function is called within the Newton-Raphson iterative process to calculate the values of the nonlinear equations (denoted as $f(\alpha)$ (1.14)) and their derivatives with respect to the switching angles ($\frac{df}{d\alpha}$ (1.18)), given a set of switching angles (α (1.13), (1.16)) and harmonic orders

to be eliminated. The accurate calculation of these values is critical for the convergence and performance of the Newton-Raphson method.

To enhance the likelihood of identifying all possible solutions to the system of nonlinear equations, the program is set to run multiple times. This iterative strategy helps to thoroughly explore the solution space. Upon program completion, it saves all unique discovered solutions into an Excel file. The purpose of this step is to facilitate a subsequent manual review process, during which these unique solution sets are separated and analysed. This approach is designed to maximize the comprehensiveness of our solution discovery process, providing a foundation for further analysis and application of the results.

1.4.2.2. Implementation details

1. **Newton-Raphson Method**: The Newton-Raphson method is employed to solve the system of nonlinear equations derived from the harmonic elimination criteria. The method iteratively refines guesses for the switching angles until a solution is found that satisfies the equations within a specified tolerance.

   The algorithm for the solution in the form of a flowchart is shown in Fig. 1.4, which is based on the actual computer program implementation. This algorithm is run a number of times for each value of modulation index.
2. **Solution "unwinding" Approach**: The improved Newton-Raphson algorithm introduces a novel approach to verify and accept solutions, utilizing the inherent properties of trigonometric functions within the system of nonlinear equations. This method ensures the correctness of identified solutions, enhancing both convergence rate and calculation speed.
3. **Parallel Processing**: The script leverages MATLAB's *PARFOR* loop for parallel processing, enabling simultaneous computation of solutions for different modulation indices or sets of equations, significantly speeding up the computation.
4. **Flexibility and Configurability**: The code is designed with flexibility in mind, allowing the user to easily adjust the harmonics to eliminate, the range and step size of modulation indices to investigate, and calculate the computational accuracy and performance parameters.

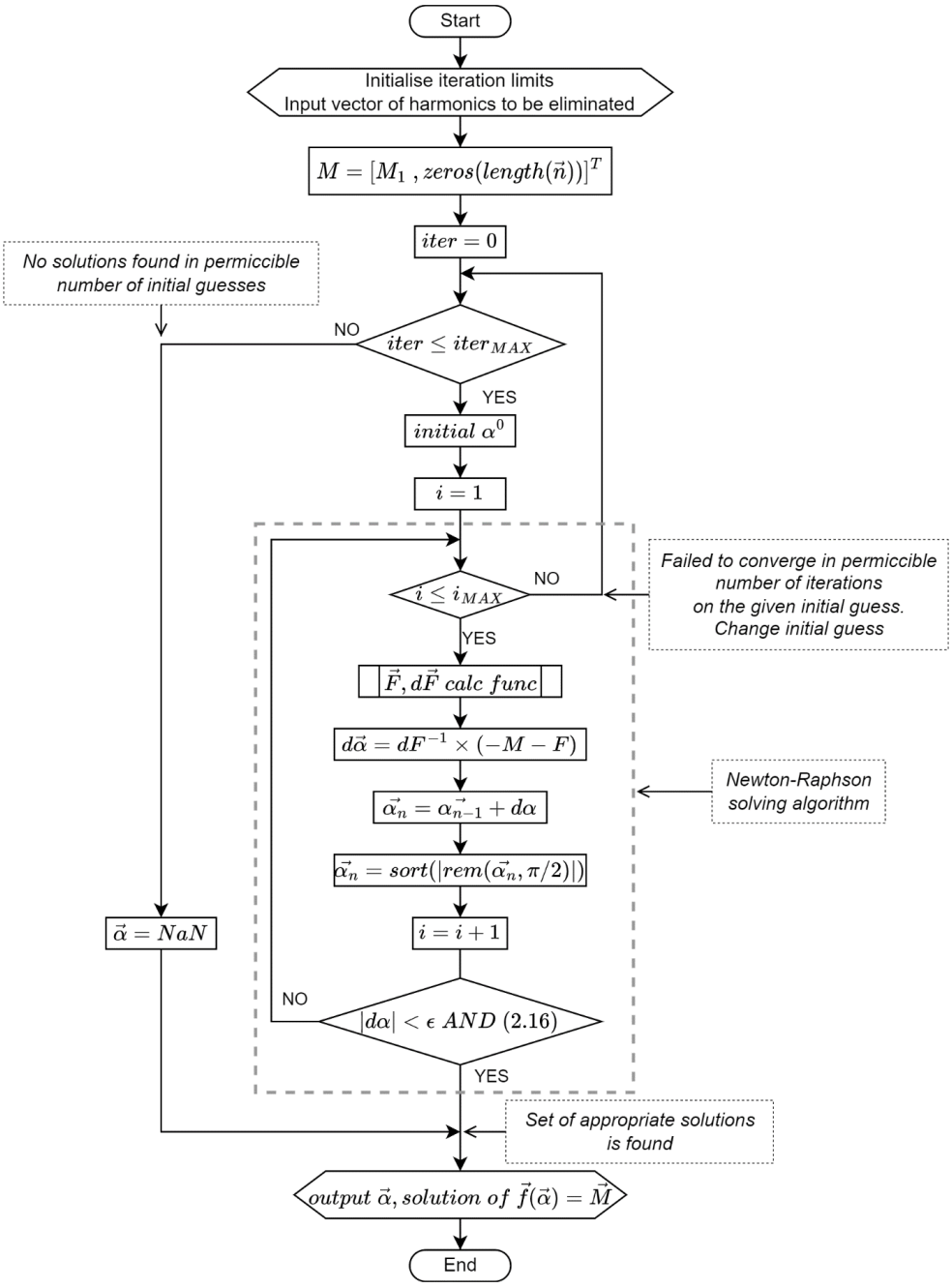

Fig. 1.4. Flowchart for the solution of SHE system of equations.

where ϵ is the desired accuracy.

1.4.2.3. Key Challenges and Solutions

1. **Convergence of the Newton-Raphson Method**: The success of the Newton-Raphson method in finding the roots depends heavily on the choice of initial guesses for the switching angles. The script tackles this by generating random initial conditions that ensure all angles are within a feasible range (0–90 degrees) and in increasing order, improving the likelihood of convergence.

   For the obtainment of solutions vector of the desired modulation indices (1.10) is created with the desired step. The program in the Fig. 1.4 is repeated number of times based on the length of modulation indices vector. In addition, the program is run predefined number of times, to increase the chance of finding the solution(s) at all modulation indices. Convergence problem becomes more prominent with the increase in number of angles, which leads to either increase in number of runs for each modulation index or increased number of initial solution guesses.

2. **Enhancing Convergence Rates: An Innovative Strategy**: The newly implemented solution aims to significantly enhance convergence likelihood. While initial iterations, guided by existing literature, successfully solve nonlinear system of SHE equations, convergence rates for systems with a higher number of angles tend to be suboptimal, as indicated (Table 1.7). To address this, several key observations were made and 'unwinding' mechanism was introduced by leveraging the intrinsic properties of trigonometric functions.

   Example:

   For a SHE 5 at $m_1 = 1$, the algorithm identified one of correct solutions:

   $$10.3669, 23.1920, 29.0769, 46.4319, 49.9495,$$

   degrees. These angles satisfy (1.17) criterion. However, another set of solutions the algorithm converges to is:

   $$730.3669, 11543.192, 1289.0769, 44866.4319, 35329.9495,$$

   which corresponds to the above angles adjusted by multiples of 90° (e.g., 10.3669° + 8×90°), initially considered invalid per (1.17). However, these are merely 'wrapped' versions of the correct solutions. To address this, developed algorithm 'unwinds' these values during each iterative loop, applying a modulus operation and sorting the results:

   ```
   alpha = sort(abs(rem(alpha, pi/2)));
   ```
   (1.19)

This modification converges to correct solutions both for 2-level and 3-level systems, while significantly enhancing the convergence rate and computational efficiency. A detailed performance analysis and further discussions are presented in chapter 1.5.

3. **Handling Multiple Solutions**: The SHE problem is known to have multiple solutions for a given set of harmonic elimination requirements. The script can identify and processing these multiple solutions, providing a comprehensive set of switching angles that meet the design criteria.
4. **Efficiency Improvements**: Various strategies are employed to improve the efficiency of the solution process, including optimizing the calculation of derivatives, employing parallel computing techniques, and careful selection of iteration parameters to balance between computational load and solution accuracy.

1.5. Application and performance of solving algorithm

This subchapter covers the application, found solutions and performance evaluation of the created solving algorithm.

1.5.1. Settings of the solving algorithm

The solving algorithm, described in chapter 1.4 is employed to find solutions for the SHE problem with 3–13 angles per quarter-wave. The range of SHE varieties analysed is summarized in Table 1.1 below.

Table 1.1 Summary of the SHE Varieties

SHE *N* switching angles	**Harmonics to be eliminated**
SHE 3	5^{th}, 7^{th}
SHE 5	5^{th}, 7^{th}, 11^{th}, 13^{th}
SHE 7	5^{th}, 7^{th}, 11^{th}, 13^{th}, 17^{th}, 19^{th}
SHE 9	5^{th}, 7^{th}, 11^{th}, 13^{th}, 17^{th}, 19^{th}, 23^{rd}, 25^{th}
SHE 11	5^{th}, 7^{th}, 11^{th}, 13^{th}, 17^{th}, 19^{th}, 23^{rd}, 25^{th}, 29^{th}, 31^{st}
SHE 13	5^{th}, 7^{th}, 11^{th}, 13^{th}, 17^{th}, 19^{th}, 23^{rd}, 25^{th}, 29^{th}, 31^{st}, 35^{th}, 37^{th}

For these computations, the 1^{st} harmonic is set to the value of the desired modulation index. The algorithm operates under the following settings:

- vector of modulation indices: $m_1 = 0.01{:}\,0.005{:}\,1.15$ (229 points);
- total number of runs: $runs_{total} = 100$;
- maximum number of attempts to guess initial solution: $iter_{MAX} = 1000$;
- maximum number of iterations to achieve required precision: $i_{MAX} = 50$;

- switching angle d_α precision is 1^{-6}. This level of precision, with all angles rounded to four-digit precision, is found to be adequate.

These settings have been validated to efficiently identify all solutions across each analysed SHE variety. However, employing an unoptimized algorithm may necessitate an increase in $runs_{total}$ due to a lower convergence rate and the challenges in locating all solutions within the specified boundaries.

The algorithm's performance has been tested on a portable machine equipped with an Intel Core i5-10300H CPU (2.5 GHz, 4 cores) and 32 GB of RAM.

1.5.2. Solutions for a 2-level inverter

The developed algorithm was executed as per the parameters outlined in Chapter 1.5.1. The solutions have been systematically recorded in a look-up table for subsequent application in modelling and laboratory testing. The number of solutions found for the 2-level inverter, which correlates with the number of angles (or harmonics to be eliminated), is presented in Table 1.2.

Table 1.2 Number of SHE Solutions for a 2-Level Inverter

SHE angles	Solutions
3	2
5	2
7	4
9	4
11	8
13	8

While the algorithm is also capable of finding solutions for a 3-level system, this aspect is not the primary focus of the current research. Therefore, details on the solutions and performance metrics for the 3-level inverter are provided in Appendix A.

Fig. 1.5 through Fig. 1.10 display sets of unique solutions for SHE cases 3, 5, 7, and 9, respectively. Each figure illustrates two continuous solution ranges for each SHE scenario, showing both the single pulse train period and the harmonic content of the pulse train at a modulation index of 1. Although solutions for SHE 11 and SHE 13 have been identified, they are not included due to the complexity of presenting eight continuous solution spaces for each.

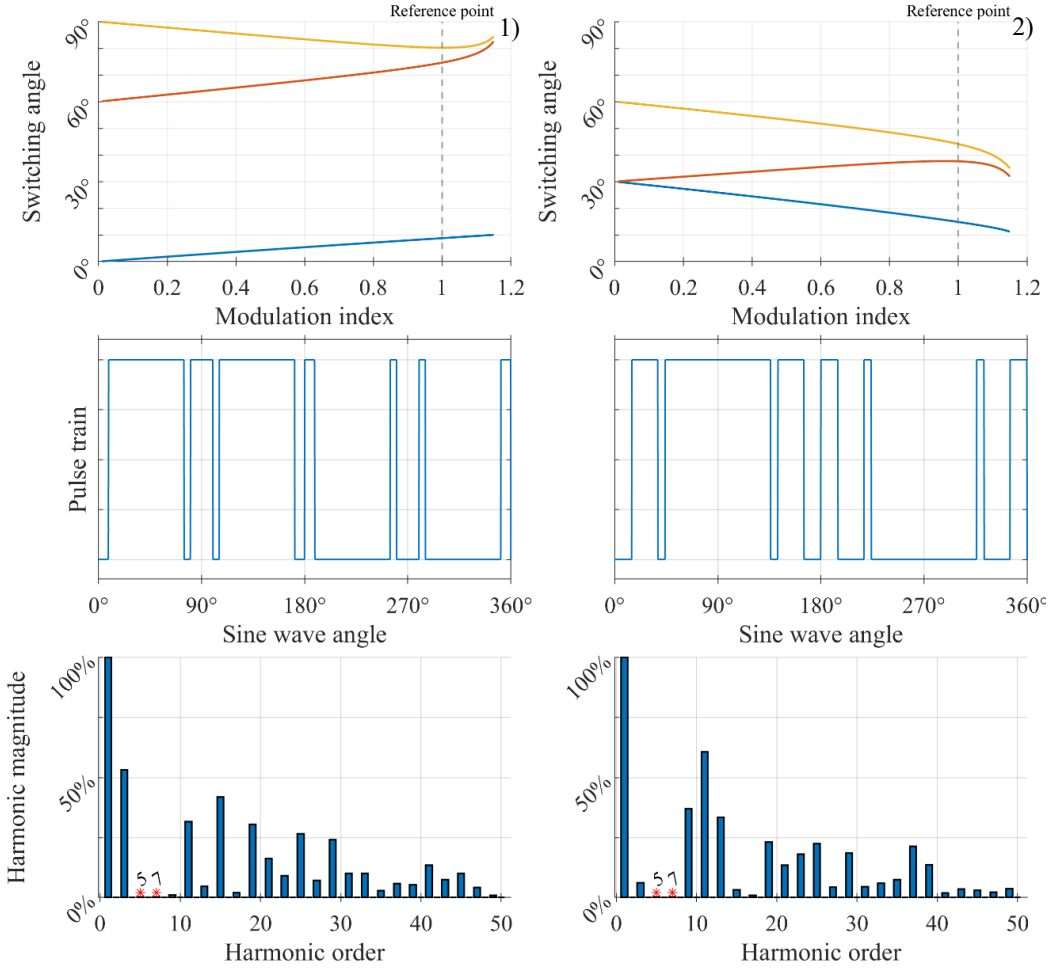

Fig. 1.5. Solution spaces for SHE 3, pulse train and FFT.

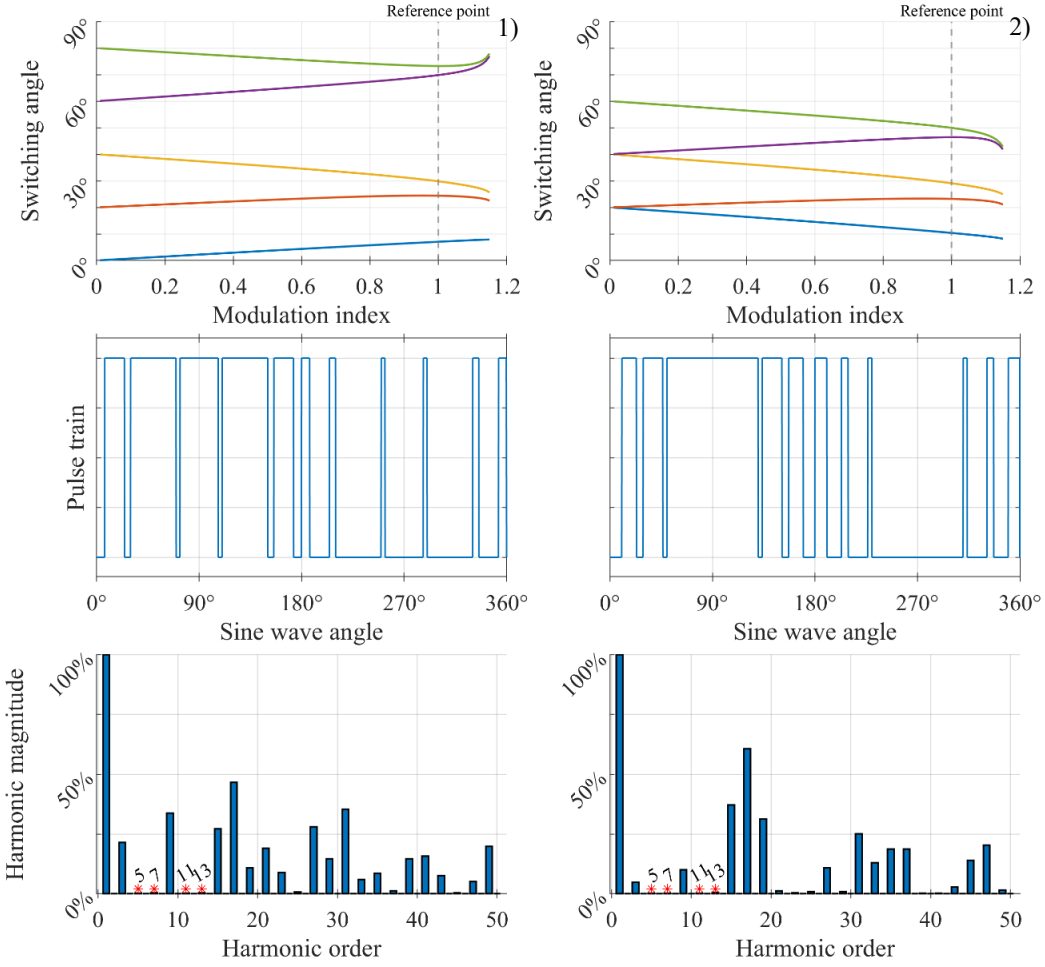

Fig. 1.6. Solution spaces for SHE 5, pulse train and FFT.

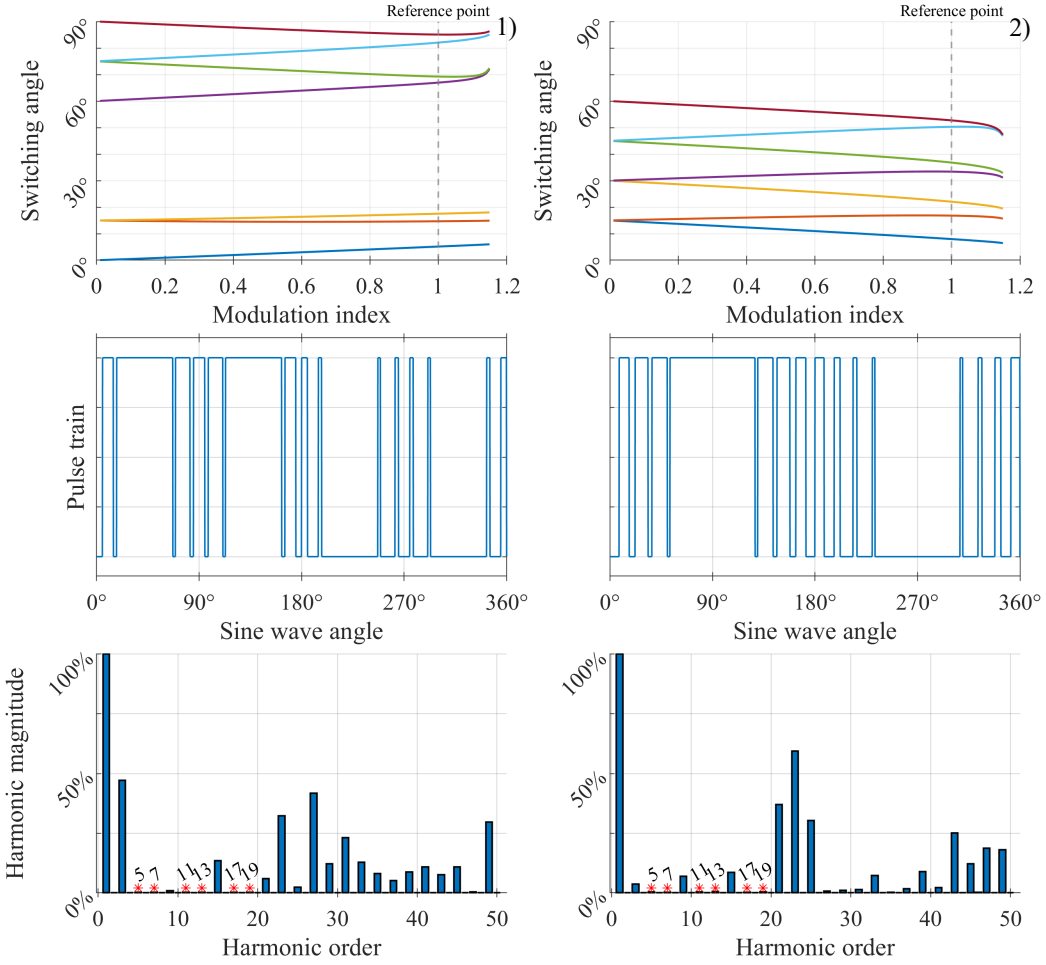

Fig. 1.7. Solution spaces for SHE 7, pulse train and FFT (1).

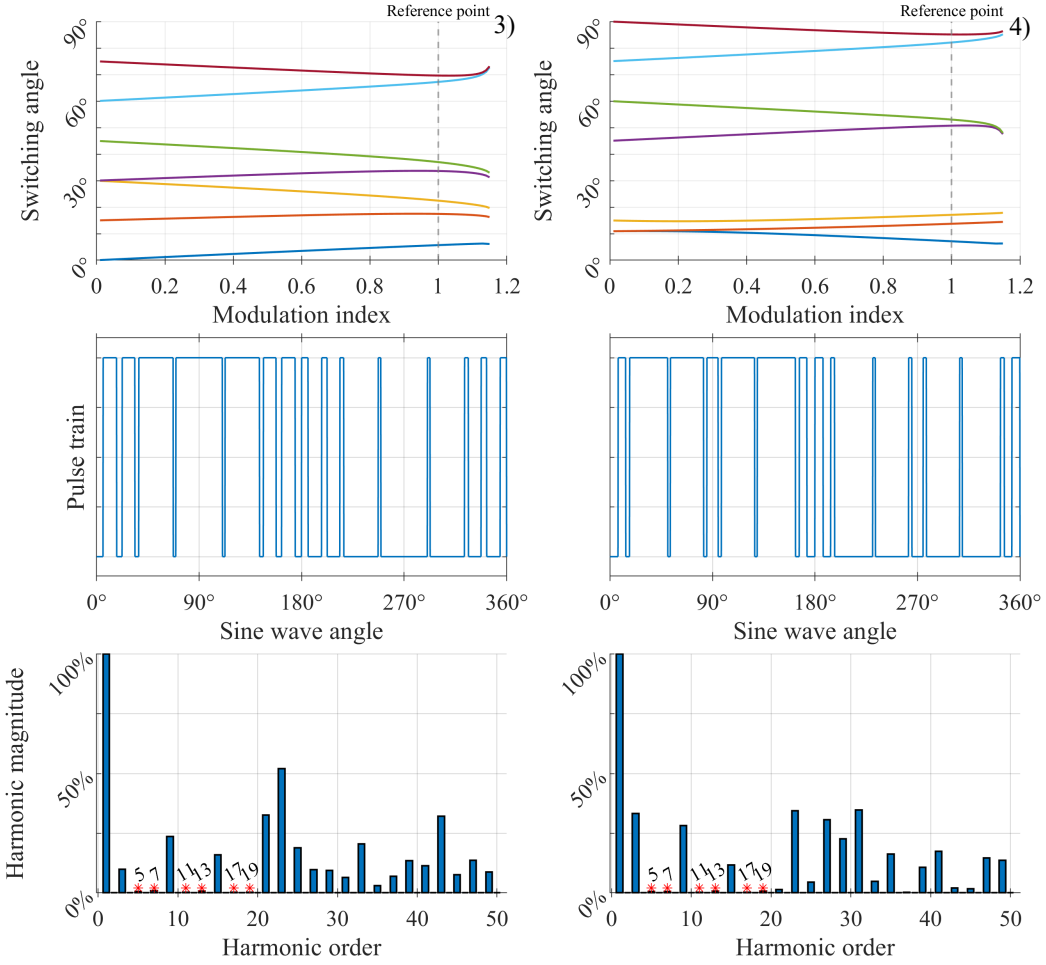

Fig. 1.8. Solution spaces for SHE 7, pulse train and FFT (2).

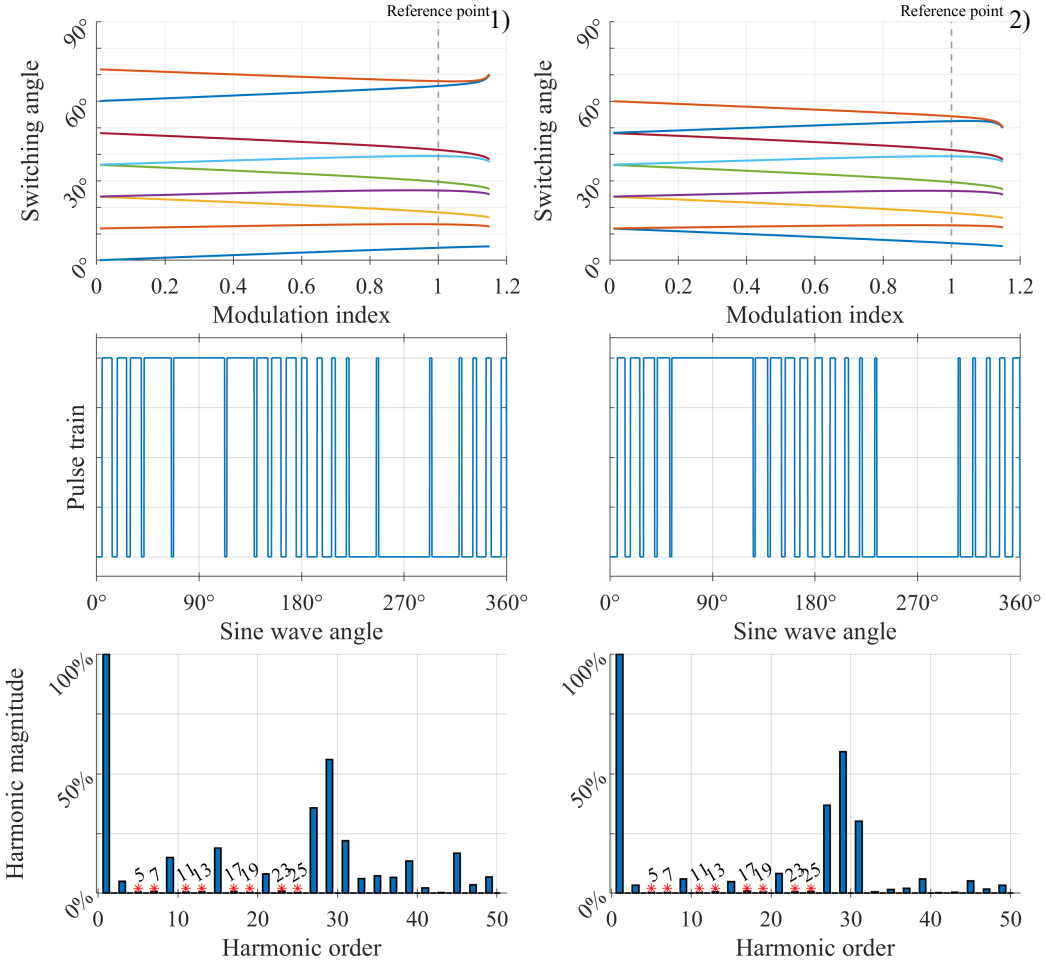

Fig. 1.9. Solution spaces for SHE 9, pulse train and FFT (1).

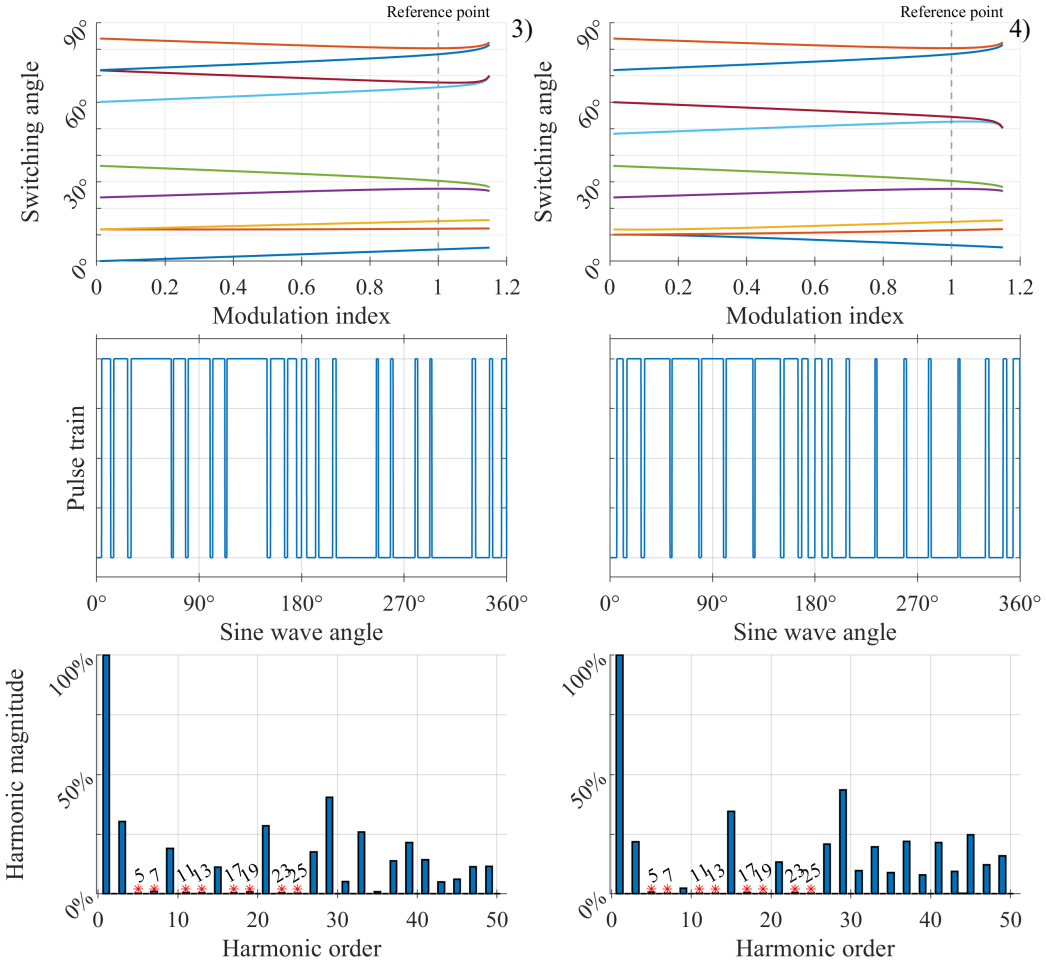

Fig. 1.10. Solution spaces for SHE 9, pulse train and FFT (2).

Initial observations from the presented SHE solutions indicate that all identified solutions for the 2-level inverter are continuous across the specified range of modulation indices, up to and including SHE 13. The harmonic analysis of the pulse trains at $m_1 = 1$ confirms the complete elimination of the targeted harmonics. Typically, the immediate non-triplen harmonic following the highest eliminated harmonic shows an increase, which aligns with expectations.

Moreover, as detailed in Chapter 1.4, the generated waveform exhibits quarter-wave symmetry, automatically nullifying all even harmonics. Currently, triplen harmonics (such as 3, 9, 15, etc.) are still present, as the analysis focuses on the pulse train itself, which is representative of the phase voltage. However, as was discussed previously, in a 3-phase electric machine line voltage is measured which cancels all triplen harmonics due to system configuration.

All found solutions are viable for achieving low-frequency operation without unwanted harmonics. Notably, some identified solutions resemble the 60° discontinuous PWM pattern (also referred to as DPWM 1–3 in some studies) [56], [57], [58] as shown in Fig. 1.7. These solutions avoid switching events for at least 60 consecutive degrees, potentially offering a further reduction in switching losses.

A more comprehensive examination of the differences between SHE solutions, particularly in terms of line voltage and stator current waveforms, is forthcoming in Chapters 3 and 4.

1.5.3. Performance of the solving algorithm

In Chapter 1.5.2, various solutions obtained through different iterations of the algorithm previously discussed were explored, including the use of MATLAB's *fsolve* function from the Optimization Toolbox. This section delves into the performance of the refined algorithm, comparing it across several performance metrics with different algorithm iterations and *fsolve* algorithm.

The evaluations were conducted using three algorithmic variations and with the *fsolve* algorithm, each set with identical parameters:

- **Unoptimized Version** utilizing a *PARFOR* loop;
- **Optimized Version** using a standard *FOR* loop;
- **Optimized Version** with a *PARFOR* loop;
- ***fsolve*** algorithm.

The *PARFOR* loop specifically facilitated parallel execution of runs across the available processor cores, which in this case amounted to 4. This parallelization is particularly advantageous when managing a higher number of harmonics.

During the development of the current implementation of the Newton-Raphson algorithm for this specific application, the in-built MATLAB *fsolve* function was employed as a benchmark to gauge comparative performance. The settings for *fsolve* were chosen to mirror those of the primary algorithm, with '*trust-region-dogleg'* for the optimization method and '*MaxIterations*' capped at 50 to align with i_{MAX}. Other parameters remained at their default settings, as detailed in Chapter 1.5.1.

The performance metrics for each variant of the algorithm are detailed in Table 1.4, Table 1.5 and Table 1.6, while performance of the *fsolve* function is presented in Table 1.3.

1.5.3.1. Performance metrics

Table 1.3 Performance of the fsolve Function

SHE angles	Computation time, s	Total num. iterations	Total num. fcn eval-s	Median num. iterations	Mean num. iterations	Standard deviation
3	74.1	37’436	2’031’655	1	1.63	1.02
5	265.9	84’607	14’125’671	3	3.69	3.20
7	786.2	200’102	52’042’282	6	8.74	8.37
9	2623.3	526’466	187’459’446	16	22.99	22.51
11	8489.8	1’373’898	599’891’514	41	60.00	62.49
13	32029.5	4’120’234	2’121’583’237	121	179.92	183.48

Table 1.4 Solving Algorithm Performance (Unoptimized, PARFOR Loop)

SHE angles	Computation time, s	Total num. iterations	Total num. fcn eval-s	Median num. iterations	Mean num. iterations	Standard deviation
3	31.5	118’187	4’898’634	4	5.16	4.62
5	144.3	921’712	45’082’997	28	40.25	39.99
7	1046.1	6’229’447	310’476’132	195	272.03	248.89
9	4515.3	18’838’242	941’315’358	1000	822.63	301.80
11	7889.3	22’194’165	1’108’980’143	1000	969.18	146.72
13	11157.7	22’873’210	1’142’400’519	1000	998.83	37.54

Table 1.5 Solving Algorithm Performance (FOR Loop)

SHE angles	Computation time, s	Total num. iterations	Total num. fcn eval-s	Median num. iterations	Mean num. iterations	Standard deviation
3	1.6	22’936	265’119	1	1.00	0.04
5	5.8	30’619	913’637	1	1.34	0.67
7	38.8	106’396	4’801’710	3	4.65	4.29
9	338.3	653’335	32’132’984	19	28.53	29.34
11	2804.5	4’686’287	232’908’781	136	204.64	209.03
13	12932.4	16’950’045	839’776’922	1000	740.18	341.48

Table 1.6 Solving Algorithm Performance (PARFOR Loop)

SHE angles	Computation time, s	Total num. iterations	Total num. fcn eval-s	Median num. iterations	Mean num. iterations	Standard deviation
3	10.2	22’940	266’381	1	1.00	0.04
5	17.4	30’586	907’225	1	1.34	0.69
7	44.7	107’226	4’843’374	3	4.68	4.22
9	154.2	650’364	31’980’968	19	28.40	29.33
11	1019.6	4’548’105	226’015’331	134	198.61	199.62
13	4355.8	16’650’931	824’964’180	1000	727.11	346.36

Where:

- *Computation time*: time to complete the program (no active demanding background tasks). This is only useful in comparison between algorithm versions, as the actual numbers are highly dependent on the computer hardware.
- *Total num. iterations*: a product between number of runs, length of modulation index array, and number of initial guesses of α per each modulation index and run iteration.
- *Total num. fcn eval-s*: number of times the most inner loop '*Calculation of function values and partial derivatives function*' is evaluated. The maximum number is limited by the product of length of $m_1 = 229, runs_{total} = 100, iter_{MAX} = 1000, i_{MAX} = 50$, and for this set of settings is 1'145'000'000 iterations. *fsolve* parameter of function evaluations is used here as a comparative benchmark.

The initial trials to solve the SHE/SHM equations utilized MATLAB's Optimization Toolbox *fsolve* function. *Fsolve* effectively replaced the *Newton-Raphson algorithm* highlighted with dashed line, as illustrated in Fig. 1.4. Across all variants, the rest of the algorithm remains consistent. Notably, the performance of the *fsolve* method surpasses that of the unoptimized algorithm but lags behind the optimized version. The stark differences in performance are due to the reliance of the unoptimized and *fsolve* algorithms on condition (1.17) for validation checks, contrasting with the internal optimizations based on trigonometric identities used in the developed algorithm. Such internal checks are not feasible with *fsolve*, highlighting the flexibility and simplicity of the Newton-Raphson method employed in the study.

The unoptimized algorithm, ran solely within a *PARFOR* loop, to speed up the computation time. For instance, solving SHE 9 scenarios takes over an hour; if executed in a *FOR* loop, this duration could extend beyond four hours. SHE 13 was also run for a complete picture, however, the unoptimized algorithm has very low convergence rate, which brings it to the limit of allowed iterations, while being unable to find most of solutions.

The principal determinant of algorithm speed is the total number of function evaluations: optimization within this aspect drastically reduces computation time. For example, for SHE 7, the optimized version reduces the number of iterations by 90.8 % compared to *fsolve* and 98.5 % compared to the unoptimized version.

To fully understand the development of the SHE/SHM algorithm, we introduce two additional performance metrics: convergence rate and success rate.

1.5.3.2. Convergence and success rate

Convergence rate: A ratio between the number of times a solution is found during a run and the number of times when $iter_{MAX}$ limit is reached (no solution found). Specifically, if no solution is identified after a predetermined number of guesses, the system is flagged as "unable to converge".

Success rate: Unlike the convergence rate, the success rate measures the proportion of the total number of solutions found against the total number of expected solutions. For instance, if the system has 8 unique continuous solutions at each of the 229 modulation index points and fails to find only 6 out of $8 \times 229 = 1832$, then the success rate is 99.7 %. Calculating the success rate for a 3-level inverter, however, presents more complexity and is addressed separately in Appendix A.

Convergence rate is shown in Table 1.7 and success rate is shown in Table 1.8 for *fsolve* algorithm, and for unoptimized and optimized developed algorithms.

Table 1.7 Convergence Rate

SHE angles	*fsolve*	Unoptimized algorithm	Optimized algorithm
3	100.0 %	100.0 %	100.0 %
5	100.0 %	100.0 %	100.0 %
7	100.0 %	97.3 %	100.0 %
9	100.0 %	33.8 %	100.0 %
11	100.0 %	5.4 %	99.1 %
13	99.5 %	0.5 %	48.2 %

Table 1.8 Success Rate

SHE angles	*fsolve*	Unoptimized algorithm	Optimized algorithm
3	100.0 %	100.0 %	100.0 %
5	100.0 %	100.0 %	100.0 %
7	100.0 %	100.0 %	100.0 %
9	100.0 %	99.6 %	100.0 %
11	100.0 %	49.4 %	99.7 %
13	99.5 %	5.7 %	99.4 %

It is important to note that the differences in convergence and success rates between the *PARFOR* and *FOR* loops are negligible, as the method of solution does not change; only the distribution of computational load across multiple CPU cores varies.

Analysis of the data reveals that while *fsolve* generally exhibits higher convergence and success rates across all SHE scenarios, it is significantly slower – taking 10 to 15 times longer – and requires more function evaluations than the optimized algorithm.

From the Table 1.4, and Table 1.7 and Table 1.8 could be seen that the time when transitioning from SHE 9 to SHE 11, and even to SHE 13 in unoptimized algorithm does not increase exponentially. That is because the algorithm is very close to pre-defined limits of iterations and convergence rate is very low, at only 5.4 %. And 0.5 % respectively. Unoptimized algorithm requires widening limits to find all the solutions, as the convergence rate is very low. For example, to find all the solutions to SHE 11 using unoptimized algorithm would potentially require 18-20 hours of computation and $runs_{total} \geq 600$, as the success rate is only 49.4 %, while for SHE 13 computation time of upwards 100 hours.

1.5.3.3. Conclusions and further optimizations possibility

This chapter has detailed enhancements to the Newton–Raphson algorithm for solving SHE and SHM problems in both 2-level and 3-level inverters. The optimized algorithm proves superior to the generic *fsolve* function in terms of both the computation time per iteration and the total number of iterations required to reach a solution. Further improvements, such as an adaptive number of runs, could enhance the algorithm's speed.

The optimization process within the algorithm primarily occurs during the solution verification phase, even though the initial guesses are randomly generated within the constraints of condition (1.17). To generate initial guesses, there is no straightforward method to acquire a-priori information that would allow for a more targeted initial guess range [17].

It is important to emphasize that the speed of calculation provided by the optimized algorithm is particularly advantageous in SHM, where minimizing THD or complying with grid codes takes precedence over mere harmonic elimination in SHE. This methodology necessitates multiple recalculations of switching angles at different harmonic level references to optimize a specific cost function. When addressing higher values of switching angles, the optimized algorithm speeds up work in the calculation stage or allows for improved step fidelity. This is crucial as some solution spaces can exhibit highly non-linear characteristics or complexities, as discussed in Appendix A.

2. Control System Development

The design of the control system, which incorporates a hybrid PWM algorithm, is a core aspect of this research. This chapter outlines the design process and lays the groundwork for the simulations and testing discussed in subsequent chapters. The design process includes several crucial steps:

1. analysing the application, parameters, and requirements for both the vehicle and the motor;
2. developing the hybrid PWM modulator;
3. designing and implementing a control system tailored to the specific needs of the application.

Each section of this chapter provides a detailed exploration of these key stages, elaborating on the process of designing and developing the control system.

2.1. Electric multiple unit

Railway vehicles come in a multitude of different varieties, the most common of which are trams, metros, trains, and locomotives. Each type has its own set of specifications, including but not limited to supply voltages, motor output power requirements, number of cars, weight, and top speeds.

For this research, the analysis is narrowed to trains, specifically electric multiple units (EMUs), as they represent a common application for medium-voltage high-power converters. Common parameters for EMUs include [4]:

- supply voltages: 750 V DC, 1500 V DC, 3000 V DC, 15 kV AC (16.7 Hz), 25 kV AC (50 Hz);
- electric motors power: 200–600 kW;
- traction converter power: 200–1400 kW;
- number of cars: 2–12;
- top speed: 120–350 km/h.

The market analysis is done to determine the average parameters of the EMUs in service. The analysis focuses predominantly on the use of EMUs in intercity and regional rail networks in Eastern Europe with a supply voltage of 3000 VDC. The 3 kV DC power supply voltage is one of the dominant power networks, accounting for 44 % of the market (combined with 1.5 kV) [59] and is utilized in countries such as Latvia, Estonia, Poland, Netherlands, Ukraine, Russia, Italy, and parts of Spain and France [60]. Where Fig. 2.1 shows the European rail electrification map [60] as a reference for distribution of railway grid voltages across continent.

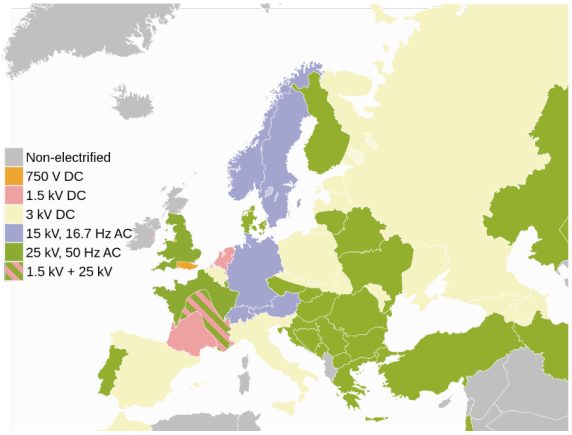

Fig. 2.1. European rail electrification map.

Market research was conducted on the EMUs used in the 3 kV DC grid from several prominent producers: Newag (Poland), Pesa (Poland), Škoda (Czech Republic), CAF (Spain), and Stadler (Switzerland).

The purpose of this comparative analysis is to outline the main variations of EMUs used in the region by comparing the continuous power of the train to its mass, and the gross weight of the train per single motor. These parameters are crucial for the selection and/or design of an appropriate traction motor. The power-to-weight ratio and mass per motor will be averaged and used for selecting the traction motor.

2.1.1. Newag Impuls

Newag Impuls is an EMU series produced by Newag, Poland from 2012 and is operated in Poland. It has maximum operating speed of 160 km/h, acceleration from 0 to 40 km/h of 1 m/s^2. With currently produced 259 out of 326 currently ordered train sets [61], [62].

Table 2.1 Summary of Newag Impuls Train Parameters

Train type	35WE	45WE	31WE	36WE	37WE
Number of cars	6	5	4	3	2
Number of motors	8	4	4	4	4
Motor power (S1, kW)	400	500	500	400	400
Train cont. Power (kW)	3200	2000	2000	1600	1600
Passenger capacity	601	544	436	330	265
Service weight (ton)	197	159	135	108	81
Gross weight (ton)	280	202	172	130	103
Mass per motor (t/mot.)	35.0	50.5	43.0	32.5	25.8
Power-to-weight (W/kg)	11.4	9.9	11.6	12.3	15.5

Traction motors are 3-phase, 4 pole squirrel cage induction motors by TSA: TMF 50-29-4 (400 kW) TMF 59-39-4 (500 kW) [2].

Power converter by MEDCOM: 2-level inverter, 6.5 kV class IGBT, PWM switching frequency 460–1100 Hz [22], [63].

2.1.2. Pesa Elf

Pesa Elf is an EMU series produced by Pesa, Poland from 2010 and is operated in Poland, Czech Republic, and Romania (ordered). It has maximum operating speed of 160 km/h, acceleration from 0 to 40 km/h of 1.2 m/s^2. With currently produced 161 out of 258 currently ordered train sets [9], [62], [64], [65].

Table 2.2 Summary of Pesa Elf Train Parameters

Train type	27WE	48WE (Elf II)	22WE	21WE	34WE
Number of cars	6	5	4	3	2
Number of motors	8	4	4	4	4
Motor power (S1, kW)	400	500	500	400	400
Train cont. Power (kW)	3200	2000	2000	1600	1600
Passenger capacity	701	540	450	326	281
Service weight (ton)	190.5	161	135	107.3	83.2
Gross weight (ton)	246.6	204.2	171.0	133.4	105.7
Mass per motor (t/mot.)	30.8	51.1	42.8	33.3	26.4
Power-to-weight (W/kg)	13.0	9.8	11.7	12.0	15.1

Traction motors are 3-phase, 4 pole squirrel cage induction motors by TSA: TMF 50-29-4 (400 kW) TMF 59-39-4 (500 kW) [2].

Power converter by Ingeteam: 2-level inverter, 6.5 kV class IGBT [9], [66].

2.1.3. Škoda 7Ev

Škoda 7Ev, also known as “RegioPanter” or “InterPanter” is an EMU series produced by Škoda Vagonka, Czech Republic since 2011 and is operated in Czech Republic, Slovakia, Latvia, and Estonia (ordered). Exists as a 3 kV DC variant, and as a dual system variant for both 3 kV DC and 25 kV 50Hz. It has a maximum operating speed of 160 km/h, maximum acceleration of 1.1 m/s^2. With currently produced 142 out of 301 currently ordered train sets [67].

Table 2.3 Summary of Škoda 7Ev train parameters

Train type	440 ČD (DC)	640 ČD (Dual)	650/651 ČD (Dual)
Number of cars	3	3	2
Number of motors	6	6	4
Motor power (S1, kW)	340	340	340
Train cont. Power (kW)	2040	2040	1360
Passenger capacity	499	499	317
Service weight (ton)	150.0	159.5	106.5
Gross weight (ton)	189.9	199.4	131.9
Mass per motor (t/mot.)	31.7	33.2	33.0
Power-to-weight (W/kg)	10.7	10.2	10.3

Traction motors are 3-phase, 4 pole squirrel cage induction motors by Škoda itself: ML 3942 K/4 [68].

With no information available on power converter.

2.1.4. CAF Civia

Civia EMU lineup is produced in collaboration with CAF, Siemens, and Alstom. This lineup was in production from 2004 till 2010 and is operated by Renfe in Spain. It has a maximum operating speed of 160 km/h, maximum acceleration of 1.3 m/s^2, and acceleration from 0 to 120 km/h of 0.59 m/s^2. With 248 produced sets [69], [70].

Table 2.4 Summary of CAF Civia Train Parameters

Train type	465	464	463	462
Number of cars	5	4	3	2
Number of motors	*8*	*6*	*4*	*4*
Motor power (S1, kW)	*275*	*350*	*350*	*317.5*
Train cont. Power (kW)	2200	2100	1400	1270
Passenger capacity	997	832	607	414
Service weight (ton)	157.3	131.5	105.8	80.0
Gross weight (ton)	237.1	198.1	154.4	113.1
Mass per motor (t/mot.)	29.6	33.0	38.6	28.3
Power-to-weight (W/kg)	9.3	10.6	9.1	11.2

Where values in *italic* are not available online but are assumed based on commonly used configurations.

Traction motors are 3-phase, 6 pole squirrel cage induction motors by Alstom [1]. While the power converter is produced by Siemens with 6.5 kV class IGBT.

2.1.5. Stadler Flirt and KISS

Flirt and KISS lineups are produced by Stadler, Switzerland from 2004 and 2011 respectively. These trains are the most common modern EMUs and are in operation across the world. They have many different variations for different markets adapted for 1.5 kV DC, 3 kV DC, 25 kV 50 Hz, 15 kV 16.7 Hz with different combinations possible. With acceleration from 0.8 to 1.3 m/s2 based on customer's requirements. Stadler Flirt sold over 2500 units [71], while Stadler KISS sold over 620 units [72].

Below are several examples of train configurations made for markets with 3 kV DC supply voltage grid.

Table 2.5 Summary of Stadler Train Parameters

	Stadler Flirt			Stadler KISS	
Train type	PKP Intercity [73]	Region Lodz [74]		Aeroexspress, Russia [75]	
Number of cars	8	2		6	4
Number of motors	4	4		8	6
Motor power (S1, kW)	500	350		400	400
Train cont. Power (kW)	2000	1400		3200	2400
Passenger capacity	672	278		1550	927
Service weight (ton)	257.0	90.0		349.0	237.0
Gross weight (ton)	310.8	112.2		473.0	311.2
Mass per motor (t/mot.)	77.7	28.1		59.1	51.9
Power-to-weight (W/kg)	6.4	12.5		6.8	7.7

Traction motors have different power and configuration, while all being induction motors. Many of which are reported to be produced by TSA [2]. The power converter system is produced by ABB, Turgi, Switzerland.

2.1.6. Average parameters

Averaging many parameters can be challenging due to their dependence on various EMU configurations, such as the number of motors per set, the number of cars per set, and motor power. Nevertheless, mass per motor and continuous power-to-weight ratios are commonly utilized to assess the comparative performance of vehicles in general. Setting the desired requirements involves considering the customer's needs, the geography of operation, and other complex factors. However, for the purposes of this research, average parameters suffice for the design and tuning of the control system.

- Average mass per motor: **38.9 tons/motor**.
- Average power-to-weight: **11.2 W/kg**.

- Common average acceleration in the constant torque regime of the induction motor: **1 m/s^2**.

These parameters are used to estimate the dynamic parameters of a train equipped with the selected induction motor, based on average specifications.

2.2. Traction motor

The selection and/or design of a traction motor is a complex process tailored for specific vehicles. The design process for the traction motor involves several key considerations to achieve a cost-effective balance among various factors. These considerations include:

- understanding the vehicle's geometrical and mounting constraints;
- addressing the dynamic requirements of the vehicle,
- Managing adhesion constraints and environmental usage conditions;
- considering wheel diameter and maximum speed;
- selecting gearbox ratio, type, and producer;
- determining the cooling approach;
- evaluating financial implications, among others.

2.2.1. Induction motor parameters

Typically, traction motors are custom-made for EMU producers in collaboration with companies specializing in traction motor production. Detailed parameters of these motors are often confidential. However, the research and development project at JSC "Rīgas elektromašīnbūves rūpnīca" has provided access to detailed parameters and testing results of the traction induction motor prototype for EMU application (Fig. 2.2). These parameters and the maximum traction characteristics are summarized below for simulation purposes.

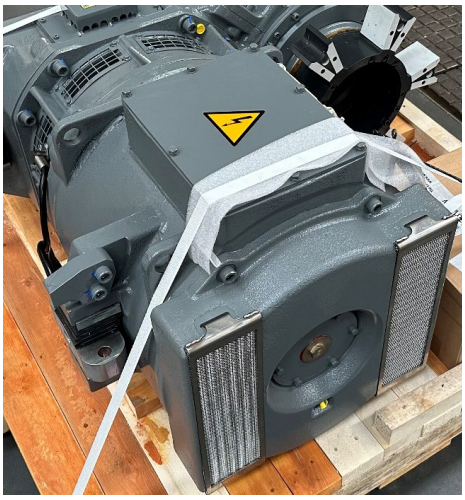

Fig. 2.2. Traction induction motor produced at AS “Rīgas elektromašīnbūves rūpnīca”.

The developed traction motor is a squirrel cage 3-phase, 4-pole, star-connected induction motor. The main parameters of the motor, operating with S1 (continuous) duty, are presented in Table 2.6.

Table 2.6 S1 Working Point Parameters

Parameter name	*Units*	*Value*
Output power (on shaft)	kW	360
Stator voltage LL	V	2340
Stator current	A	107.4
Power factor	-	0.886
Frequency	Hz	79.5
Slip	%	1.06
Rotational speed	RPM	2359.8
Mechanical torque	Nm	1456.8
Maximum torque	Nm	3925.6
Efficiency	%	93.1
Current, slip=0	A	35

The maximum speed of the motor is 4774 RPM, with an insulation class of 220°C. The motor's mass does not exceed 770 kg. To obtain equivalent circuit parameters, the motor was tested according to IEC 60034-28:2012 [76]. These parameters are detailed in Table 2.7.

Table 2.7 Equivalent Circuit Parameters

Parameter name	*Units*	*Value*
Stator resistance at 20°C	mΩ	166.3
Rotor resistance at 20°C	mΩ	101.5
Stator leakage inductance	mH	2.23
Rotor leakage inductance	mH	2.80
Magnetizing inductance	mH	77.05

Table 2.8 shows the mechanical parameters of the induction motor. For the design of the speed control of the control system inertia is the most important part. These parameters are obtained based on the deceleration test [77] and based on the known geometry of the electrical machine.

Table 2.8. Mechanical Parameters

Parameter name	*Units*	*Value*
Inertia of the rotor	kgm^2	8
Viscous friction coefficient	Nms/rd	0.02

2.2.2. Traction characteristic

The reference traction characteristic of the electrical traction motor represents the maximum effort of the motor during normal acceleration. This is crucial as a dynamic limiter in the control system. Creating such a limiting traction characteristic involves understanding the motor's thermal limits, converter current limits, the used gearbox, and the vehicle's dynamic requirements. Traction effort limit is a part of the electrical-mechanical characteristics of the motor, depicting output power, torque, line voltage, and stator current at maximum effort, as shown in Fig. 2.3.

Traction characteristic has the following regions:

1) 0–350 RPM: torque is limited to the value achieved when stator current is limited to 250 A RMS;
2) 350–1720 RPM: constant torque region limited by $T_{out} = 3000$ Nm;
3) 1720–3310 RPM: constant power region limited by $P_{out} = 540$ kW;
4) 3310 – 4780 RPM (max speed): $T_{elm}\omega_m \cong constant$ or $T_{em} \propto \frac{1}{\omega_s^2}$ region.

Additionally, at the value of torque during traction characteristic (at 2427 Nm) and at a speed of 2130 RPM, stator line voltage reaches a nominal value of 2340 V RMS. Below 2130 RPM, it keeps a nominal flux of 2.9 Vs, and above 2130 RPM, the motor goes into a field-weakening regime. With an implemented feedback-based field weakening controller, this speed point varies slightly depending on the load.

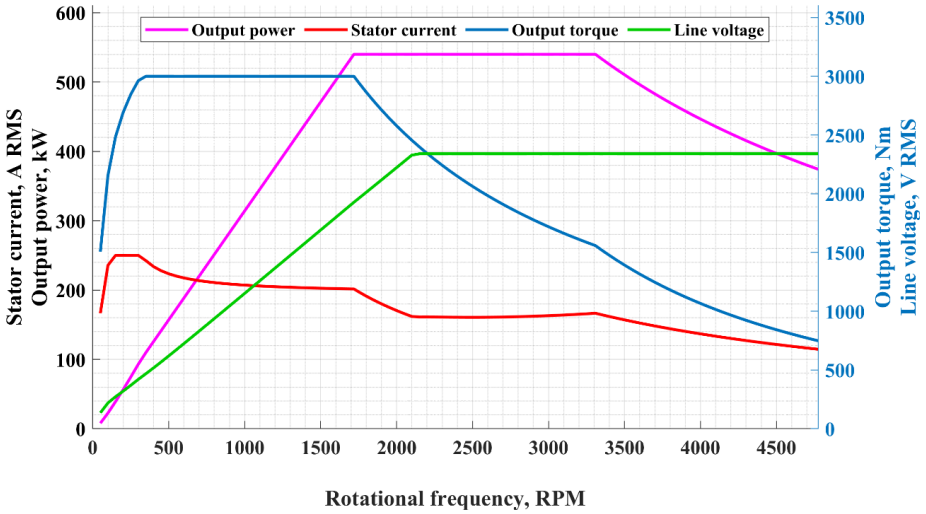

Fig. 2.3. Reference traction characteristic of the induction motor.

The characteristic was developed for the actual motor prototype. The output power in the constant region is 540 kW, which is 1.5 times higher than in S1 duty. This is because the motor does not operate at this power most of the time but only during maximum effort acceleration and deceleration.

2.2.3. Selection of final train parameters

Chapter 2.2.2 and 2.2.3 are interconnected, as the creation of the limiting traction characteristic is always tailored to the vehicle. Railway vehicles are generally treated as semi-rigid bodies, described by their linear and angular position along three coordinated dimensions. For this research, only the longitudinal motion is considered. The mathematical model is based on the approach by A. Sciaretta and A. Vahidi, 2020 [78], with detailed implementation shown in prior research by the author [79]. The parameters selected are consistent with those discussed in Chapter 2.1.6 and commonly used parameters from scientific literature. Key selected parameters include:

- Average gross mass (including passengers) per motor: 38.9 tons/motor.
- 2 motors per car.
- Train resistance: $w_o = 0.6 + 0.027 \cdot v + 0.00005 \cdot v^2 [N/kN]$ [80].
- Inertial mass ratio: $\gamma = 1.08$ [59], [80], [81]. It is different for different train types and configurations. 1.08 is a commonly used value for intercity and regional EMUs.
- Wheel diameter (commonly used): 0.85 m – new, 0.78 m – worn out.
- Gearbox ratio: 5.89, chosen to ensure a maximum operating speed of 120 km/h even with worn-out wheels.

Based on these parameters, the train is calculated to have:

- power-to-weight ratio: 9.3 W/kg;
- maximum acceleration: 0.95 m/s^2;
- average acceleration from 0 to 50 km/h: 0.89 m/s^2, and time to reach 50 km/h is 15.7 seconds;
- acceleration from 0 to 120 km/h with a new wheel: 59.4 seconds.
- maximum speed with new wheel – 130 km/h, with worn out wheel – 120 km/h.

In Fig. 2.4 the dependency of train acceleration on speed based on the designed maximum traction characteristic with the traction induction motor under consideration is depicted.

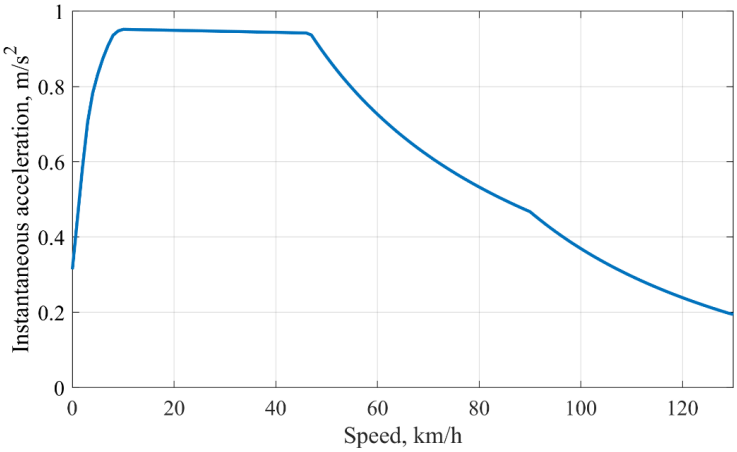

Fig. 2.4. Acceleration of the train with average parameters and selected traction motor.

As the designed traction motor is a first iteration prototype, some of the resulting parameters, such as average acceleration, maximum speed, and power-to-weight ratio, are below average. From the testing, several changes are planned for a second iteration.

Moreover, while this calculation uses average parameters, the actual induction traction motor application will require adjustments to the motor's outer casing for mounting and changes to crucial parameters such as train car weight, gearbox ratio, and dynamic requirements.

This calculation serves solely as a reference for the design and development of the control system methodology. Based on this methodology, any other combination of train, motor, and power converter parameters could be used to achieve the required result.

2.3. Power converter

Besides the traction motor, the power converter is another important component of the traction drive. As previously discussed, this research implements a hybrid PWM approach aiming to limit

IGBT and diode losses within junction temperature limits while reducing harmonic currents compared to conventional modulation methods.

An important part of the research involves the precise calculation of IGBT module losses. This accuracy is essential to assess the impact of PWM types not only on the stator current quality but also on the converter's losses.

Only losses are calculated, not the junction temperature, as temperature calculation requires an understanding of the utilized heatsink and cooling solution. These factors are highly application-dependent and are typically designed based on the hardware configuration of the actual implementation, often modelled using FEM analysis with specialized software. However, losses are sufficient for comparative analysis of different modulation strategies.

This subchapter first covers converter losses, followed by the selection of the IGBT power module designed for traction applications. It investigates the parameters used for loss calculation and concludes with a calculation example.

2.3.1. Power converter losses

In frequency inverter operation IGBT operates as a switch with anti-parallel freewheeling diode, taking on various static and dynamic states in cycles. In any of these states, one power dissipation or energy dissipation component is generated, heating the semiconductor, and adding to the total power losses of the switch [82]. Fig. 2.5 shows the individual power losses of semiconductor switches.

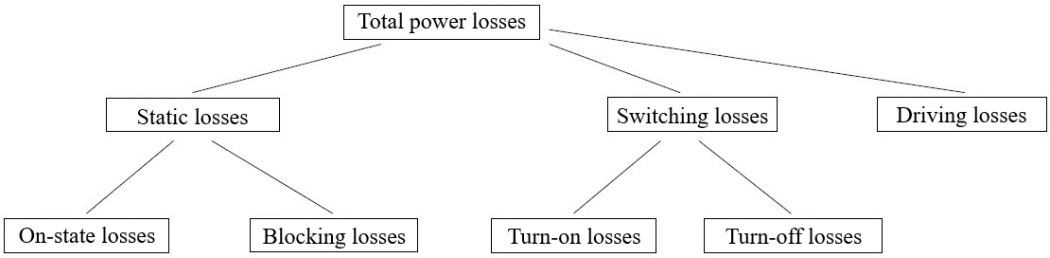

Fig. 2.5. Individual power losses of semiconductor switches [82].

Below presented calculation methodology is based on Semikron's application manual [82].

2.3.1.1. IGBT losses

Blocking losses and driver losses account for a small share of the total power dissipation, they can normally be neglected.

Conduction or on-state losses are dependent on [82]:

- the load current. Collector-emitter voltage drop in the on state (2.1) is an approximation function from the producer datasheet.
- the junction temperature

Below are mathematical representations of on-state losses:

$$P_{cond(T)} = \frac{1}{T}\int_{t_{n-1}}^{t_n} i_C(t) \cdot v_{CE}(t)\, dt, \tag{2.1}$$

$$v_{CE}(t) = f\big(i_c(t), T_j\big). \tag{2.2}$$

In different calculation approaches the losses are often averaged either over fundamental cycle, or phase of the current, however all of the losses in this calculation are instantaneous. And averaged later over the fundamental frequency. The instantaneous losses could be easily calculated during modelling phase, as the discrete time step in a Simulink model is sufficiently small. In the case of the model described further it is 10 microseconds. Instantaneous losses are crucial for understanding differences between modulation strategies with the same switching frequency.

At given control parameters (R_G, V_{GG}) and neglecting parasitic effects (L_S, C_{load}), turn-on and turn-off losses are dependent on:

- the load current and the electric load type (ohmic, inductive, capacitive)
- the DC link voltage
- the junction temperature
- the switching frequency

$$P_{on/off}(t) = \frac{E_{on/off}(t)}{T_{step}}, \tag{2.3}$$

$$E_{on/off}(t) = f\big(V_{DC}, i_c(t), T_j\big). \tag{2.4}$$

Equation (2.5) represents total considered losses of the IGBT:

$$P_{total(T)} = P_{cond(T)} + P_{on} + P_{off}. \tag{2.5}$$

2.3.1.2. Freewheeling diode losses

Since it only accounts for a minor share of the total power dissipation, reverse blocking power dissipation may also be neglected in this case. The same constraints and assumptions apply to diode as to IGBT, the losses constitution is also similar to the IGBT. Turn-on power dissipation is caused by the forward recovery process [82].

Conduction losses are dependent on:

- the load current (over output characteristic $V_F = f(I_F), T_j$)
- the junction temperature

$$P_{cond(D)} = \frac{1}{T}\int_{t_{n-1}}^{t_n} i_F(t) \cdot v_F(t)\, dt, \tag{2.6}$$

$$v_F(t) = f\big(i_F(t), T_j\big). \tag{2.7}$$

At given control parameters of the IGBT commutating with the diode, and neglecting parasitic effects (L_S), turn-off (diode recovery) losses (P_{rec}) are dependent on:

- the load current
- the DC link voltage
- the junction temperature
- the switching frequency

$$P_{rec}(t) = \frac{E_{rec}(t)}{T_{step}}, \tag{2.8}$$

$$E_{rec}(t) = f\left(V_{DC}, i_F(t), T_j\right), \tag{2.9}$$

Total losses are calculated in the same manner as for the IGBT:

$$P_{total(D)} = P_{cond(D)} + P_{rec}. \tag{2.10}$$

Total losses of the single power module are obtained through a summation of constituent losses. While total losses of the power converter are multiplied by 6, as there are 6 power modules in a 3-phase 2-level topology.

$$P_{total} = P_{total(T)} + P_{total(T)}, \tag{2.11}$$

$$P_{converter} = 6 \cdot P_{total}. \tag{2.12}$$

2.3.2. IGBT power module

ABB is one of the leading producers of both power converters for railway applications, and IGBT power modules used in power converters. Therefor for specific calculation of converter losses one of the power modules with freely available datasheet is selected matching the power demand and breakdown voltage requirements.

ABB HiPak 5SNA 0600G650100 IGBT power module is selected and used [83] for losses calculation, with parameters for the IGBT turn-on, turn-off, and conduction losses, and diode turn-on (recovery) and conduction losses in XML format available from the manufacturer's website [84], [85]. The power module is shown in Fig. 2.6.

This is power module has a 6.5 kV rated blocking voltage and is designed for a collector current of 600 A.

Fig. 2.6. ABB HiPak 5SNA 0600G650100 IGBT power module.

2.3.2.1. IGBT on-state characteristic

IGBT on-state characteristic is shown in Fig. 2.7 and it represents a function of $V_{CE}[V] = f\left(I_C[A/1000], T_j\right)$. The values are for the $V_{GE} = 15\ V$ and are obtained from manufacturer provided data in XML format [84].

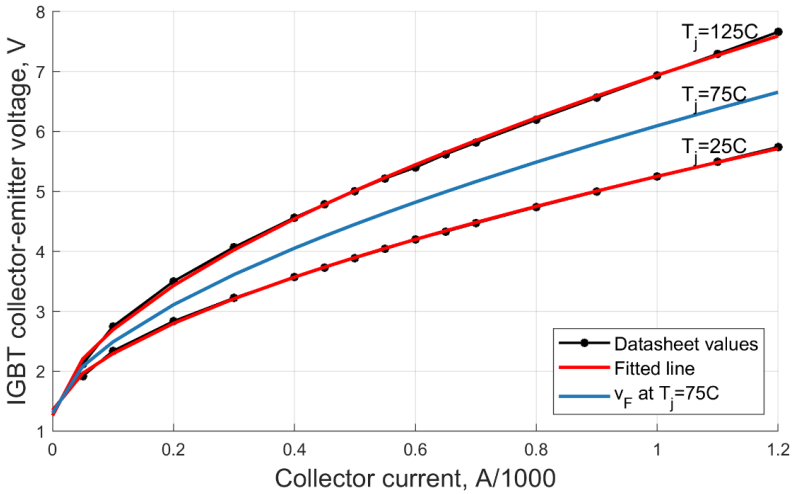

Fig. 2.7. IGBT forward voltage fit.

Conduction collector-emitter voltage of the IGBT, as well as forward voltage of the diode are approximated as a function of current, and junction temperature form the manufacturer's datasheet. Many publications suggest a linear approximation; however, a power function dependency in the form of $(v = a \cdot i^b + c)$ showed better fitting results. Therefore, it was used for data fitting, with temperature dependency modifying each coefficient linearly, as datasheets usually provide curves at 25°C and at a maximum junction temperature of 125°C or 150°C.

To dynamically calculate the collector-emitter voltage for the conduction losses calculation approximation coefficients are extracted from the datasheet data using 'fit' MATLAB function with 'power2' approximation in the form of $a \cdot x^b + c$ both for $T_j = 25°C$ and $T_j = 125°C$. These approximations account for collector current. R^2 for $T_j = 25°C$ is 0.9996 and $T_j = 125°C$ is 0.9992.

Approximation model has 6 coefficients and accounts for collector current and junction temperature variations to dynamically calculate collector-emitter voltage. Coefficients for the power module under consideration are shown in Table 2.9, and calculation approach detailed in equations (2.13) and (2.14).

Table 2.9. Coefficients for Approximation of v_{CE}

	1	2
a	0.0178	3.9008
b	-1.7048e-4	0.6152
c	-8.8520e-4	1.3507

$$a = a_1 \cdot \left(T_j - T_{ref}\right) + a_2 \tag{2.13}$$

$$v_{ce} = a \cdot I_{C_{norm}}^{b} + c \tag{2.14}$$

Where equation (2.13) accounts for the junction temperature and is applied to each coefficient of equation (2.14). $I_{C_{norm}} = I_C/1000$ is normalised collector current.

2.3.2.2. IGBT switching energies

IGBT per pulse switching energies consist of turn-on and turn-off energies and are dependent on both collector current and junction temperature. In most of the calculations junction temperature dependence is neglected, however for accurate calculations and if the data is available T_j dependency is considered.

Switching energies are obtained from manufacturer's data. Fitting of both turn-on (Fig. 2.8) and turn-off (Fig. 2.9) energies is done in very similar manner to the v_{ce} with the only distinction being type of fitting function, in this case it is done using MATLAB 'fit' function with 'poly3' type approximation in the form of $p_1 \cdot x^3 + p_2 \cdot x^2 + p_3 \cdot x + p_4$. This type of approximation function showed best fitting results.

IGBT driver parameters for the calculation are left default from the manufacturer's datasheet, and in the actual application coefficient are adjusted based on the actual circuitry. $V_{CC} = 3600V, R_G = 3.9\ ohm, V_{GE} = \pm 15V, L_\sigma = 280nH$.

However, switching losses for the IGBT and diode are dependent on DC-link voltage, in datasheet abbreviated as collector-emitter supply voltage V_{CC}. Losses are scaled accordingly as the ratio between actual and reference voltage $E_{sw} = E_{sw_{ref}} \left(\frac{V_{DC}}{V_{CC_{ref}}} \right)^{K_v}$. In the scope of this calculation reference voltage is $V_{CC} = 3600V$. While for the IGBT $K_v \approx 1.3 \dots 1.4$, and for the diode $K_v \approx 0.6$ [82].

Coefficients for the approximation model of turn-on and turn-off losses are shown in Fig. 2.8 and Fig. 2.9 respectively. While equations for approximated model of both turn-on and turn-off energies use equations shown in (2.15) and (2.16). Where $I_{C_{norm}} = I_C/1000$ is normalised collector current.

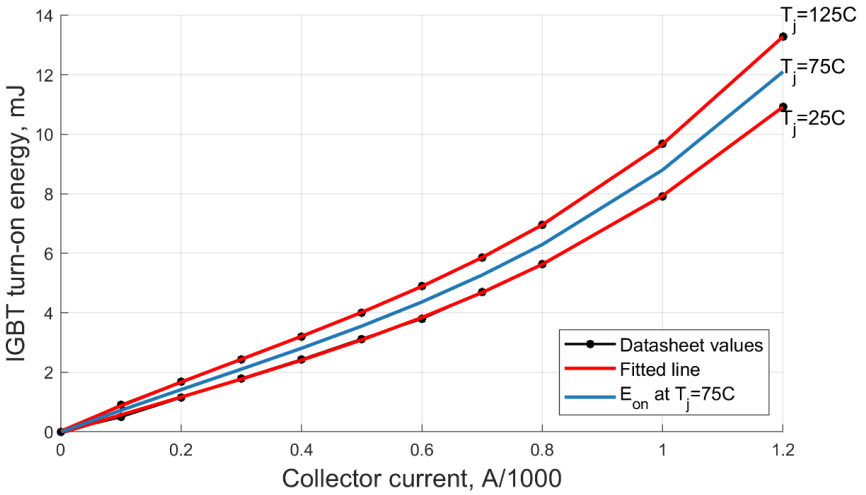

Fig. 2.8. IGBT turn.on energy fit.

For the case of IGBT R^2 for turn-on energy at $T_j = 25°C$ is 0.9999 and $T_j = 125°C$ is 1.

Table 2.10. Coefficients for Approximation of E_{on}

	1	2
p_1	0.0188	3.3776
p_2	-0.0293	-1.6365
p_3	0.0272	6.2380
p_4	6.2242e-4	-0.0437

$$p_x = p_{x1} \cdot \left(T_j - T_{ref}\right) + p_{x2} \tag{2.15}$$

$$E_{on/off} = p_1 \cdot I_{C_{norm}}^3 + p_2 \cdot I_{C_{norm}}^2 + p_3 \cdot I_{C_{norm}} + p_4 \tag{2.16}$$

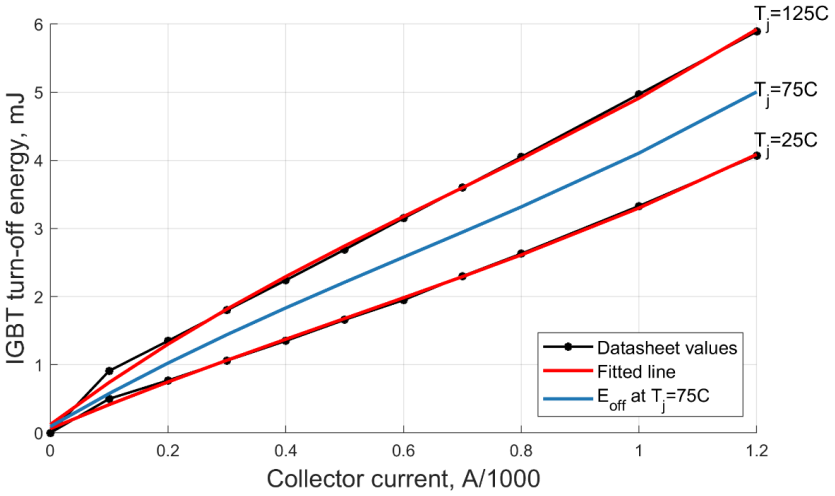

Fig. 2.9. IGBT turn-off energy fit.

For the case of IGBT R^2 for turn-off energy at $T_j = 25°C$ is 0.9986 and $T_j = 125°C$ is 0.9974.

Table 2.11. Coefficients for Approximation of E_{off}

	1	2
p_1	0.0079	0.8156
p_2	-0.0210	-1.2133
p_3	0.0286	3.6358
p_4	6.0423e-4	0.0624

2.3.2.3. Diode forward characteristic

Diode forward characteristic is constructed in the same way as IGBT's v_{ce} characteristic. Diode forward characteristic with fitted curves and intermediate junction temperature approximation is shown in Fig. 2.10. Values of the forward voltage are provided by the manufacturer in the XML format [85].

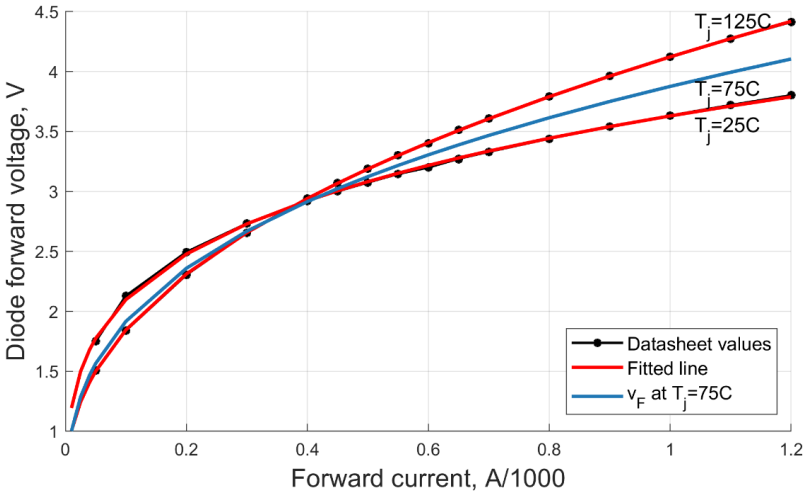

Fig. 2.10. Diode forward voltage fit.

Approach to extraction of approximation model coefficients is identical to the IGBT v_{CE}. For the case of diode R^2 for $T_j = 25°C$ is 0.9995 and $T_j = 125°C$ is 1.

Table 2.12. Coefficients for Approximation of v_F

	1	2
a	-0.0013	3.7412
b	0.0020	0.2286
c	0.0062	-0.1115

$$a = a_1 \cdot \left(T_j - T_{ref}\right) + a_2 \tag{2.17}$$

$$v_F = a \cdot I_{F_{norm}}^{b} + c \tag{2.18}$$

$I_{F_{norm}} = I_F/1000$ is normalised forward current.

2.3.2.4. Diode reverse recovery characteristic

Typical diode reverse recovery characteristic is analysed based on manufacturer's data. Fitting approach is identical to the switching energies of the IGBT and the approximation 'poly3' model is constructed in the form of $E_{rec} = f\left(I_F, T_J\right)$. Manufacturer's data, fitted curves, and curve at intermediate temperature is shown in Fig. 2.11, with model parameters shown in Table 2.13, with the equations shown in (2.19) and (2.20).

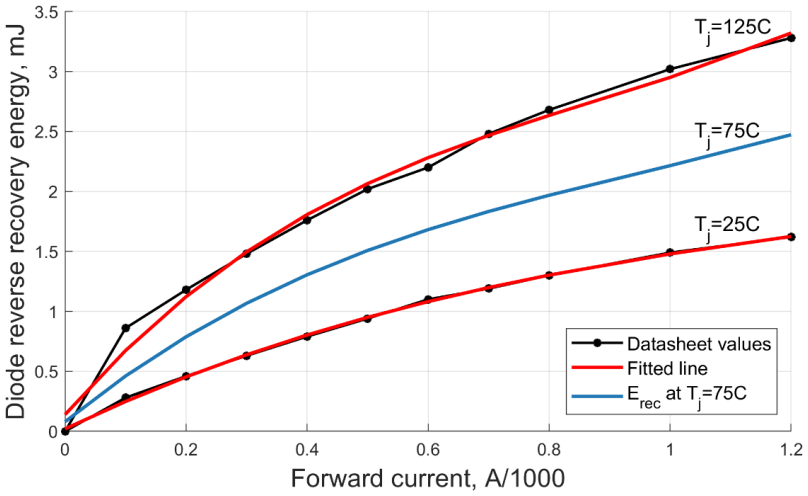

Fig. 2.11. Diode reverse recovery energy fit.

For the case of diode goodness-of-fit R^2 for $T_j = 25°C$ is 0.9987 and $T_j = 125°C$ is 0.9885.

Table 2.13 Coefficients for Approximation of E_{rec}

	1	2
p_1	0.0155	0.2755
p_2	-0.0361	-1.2148
p_3	0.0341	2.3980
p_4	0.0012	0.0205

$$p_x = p_{x1} \cdot \left(T_j - T_{ref}\right) + p_{x2} \tag{2.19}$$

$$E_{rec} = p_1 \cdot I_{F_{norm}}^3 + p_2 \cdot I_{F_{norm}}^2 + p_3 \cdot I_{F_{norm}} + p_4 \tag{2.20}$$

$I_{F_{norm}} = I_F/1000$ is normalised forward current.

2.3.3. Losses calculation approach

Losses calculation is done instantaneously at each discrete calculation step. Losses are calculated separately for IGBT and diode. For the analysis and comparison of PWM approaches losses are averaged over each fundamental period over several fundamental periods.

The calculation function takes approximation model coefficients, DC-link voltage, stator phase current, and corresponding IGBT pulse.

Fig. 2.12 shows the calculated distribution of instantaneous losses in a single power module of a power converter of a single period of fundamental current waveform in stationary regime. Modelling is done in Simulink using model described in the later sections of this chapter.

The instantaneous losses are only informative to show the calculation approach. Regime of the motor operation has the following parameters:

- SHE 5 PWM;
- equivalent switching frequency: 793 Hz,
- rotational speed: 2125 RPM;
- output torque: 2462 Nm;
- power factor: 0.896;
- stator phase current: 162 A_{RMS};
- fundamental stator line voltage: 2340 $V_{1_{RMS}}$.

This is one point at the traction characteristic of the motor (Fig. 2.3), where target fundamental RMS voltage is reached.

Average losses in stationary regime:

- IGBT conduction loss: 205 W;
- diode conduction loss: 19 W;
- IGBT switching loss: 998 W;
- diode switching loss: 480 W.

Total power module loss: 1702 W

Total power convert loss: 6x1702 W ≈ 10.2 kW

Calculated losses distribution corresponds to theoretical ratio of IGBT:Diode ≈ 2…3:1 = 2.4 (in this case) [82]. With conduction losses ratio of IGBT : Diode ≈ 10.8 corresponding to power factor dependency [82].

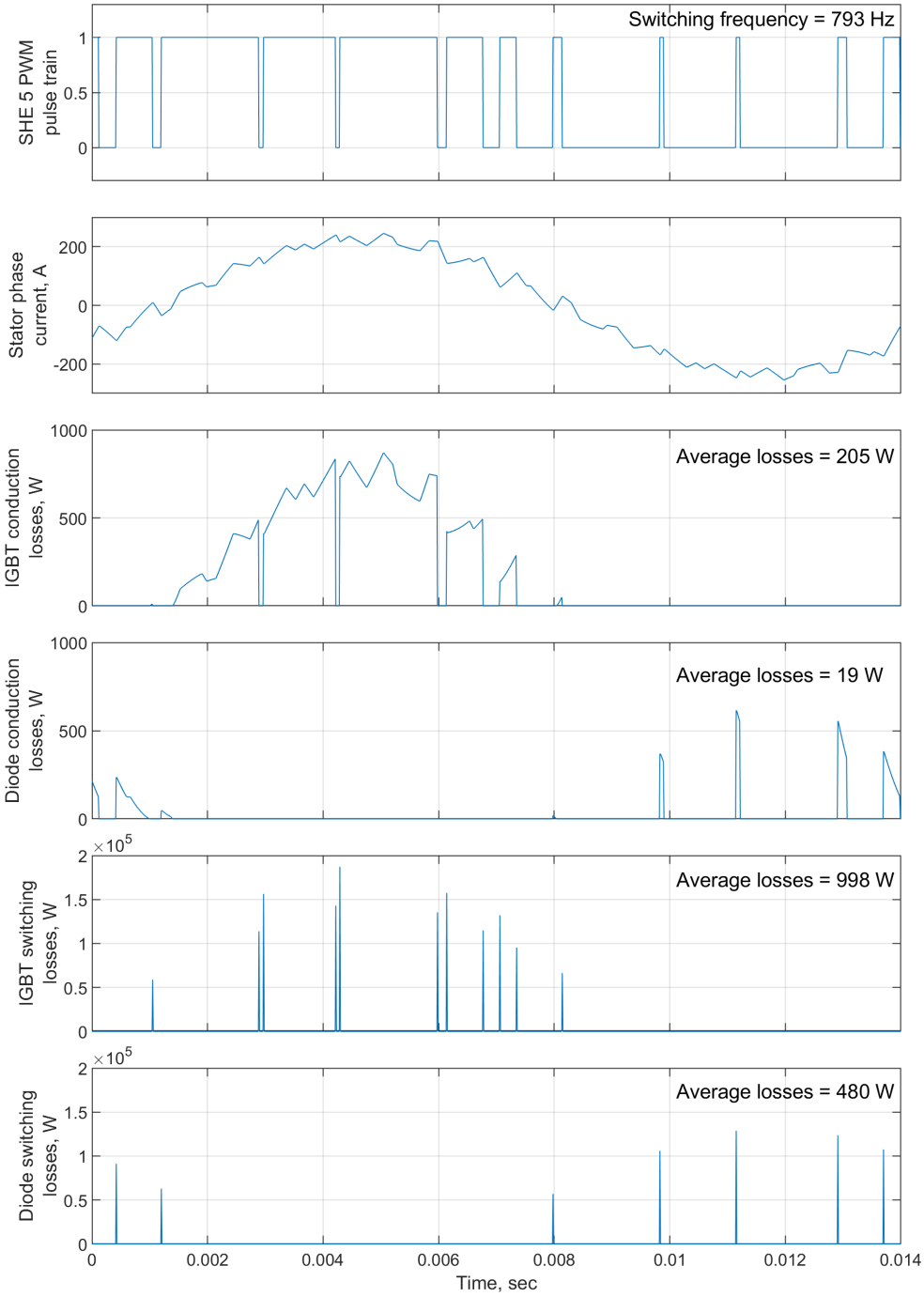

Fig. 2.12. Distribution of losses in power module (calculated).

2.4. PWM modulator

The next major component in the design of the control system is the PWM modulator. As previously described, hybrid PWM combines several distinct PWM regimes: asynchronous, synchronous, and SHE PWM. This subchapter delves into the details of the PWM modulator implementation.

2.4.1. Asynchronous and synchronous PWM generation

The generation of asynchronous and synchronous PWM is conducted similarly, with the primary difference being that the reference carrier frequency for asynchronous PWM remains constant, whereas for synchronous PWM, it is a multiple of the synchronous frequency from the control system.

The crucial element for both the asynchronous and synchronous sinusoidal PWM is the creation of a carrier signal. On a microcontroller, this is achieved using a built-in clock peripheral with up-down counting capabilities. However, in Simulink, it necessitates the creation of a function that can accurately handle the generation of the carrier signal. This function generates a sawtooth signal ranging from –1 to +1, which must precisely follow the signal frequency while detecting changes in the slope. Accurate frequency generation is vital in the discrete system environment, as the step-created frequencies tend to fluctuate.

Although Simulink provides built-in blocks for "Carrier" and "Sawtooth Generation" from the Simscape library, these blocks lack the ability to dynamically change their frequency and offer limited flexibility.

The function developed for this purpose manages the generation of a saw-tooth with precise frequency control, crucial for applications using asynchronous and synchronous PWM within the fixed-step execution constraints of Simulink. It accepts inputs such as reference carrier frequency, and fixed sampling time. The function propagates update of reference carrier frequency each step, enabling smooth slopes and timely transitions while maintaining precise phase alignment. It also compensates for the limitations due to the finite precision of discrete systems, particularly noticeable at higher carrier frequencies. By accurately calculating the carrier frequency, it prevents the drift between the discrete realization and its continuous counterpart. Additionally, this function monitors the first derivative to detect changes in sign, indicating a need to adjust the carrier's slope and trigger an update in frequency settings.

In the final step of generating asynchronous and synchronous PWM, a three-phase space-vector generated by the control system is compared with the carrier to produce the output PWM pulse train.

2.4.2. SHE PWM generation

Initially, angles for transition points are retrieved from a look-up table based on the current value of the modulation index. These angles are then passed to the function responsible for creating the pulses themselves.

Fig. 2.13 shows main body of the function in the form of a flow-chart, where T_s is the fixed time step of the Simulink, f_1 set synchronous frequency, as output from the control system, $\vec{\alpha}$ is an array of angles to switch at from look-up table, $\vec{\theta}$ array of three clock signals. This flowchart includes two functions responsible for determining actual switching based on the provided angles.

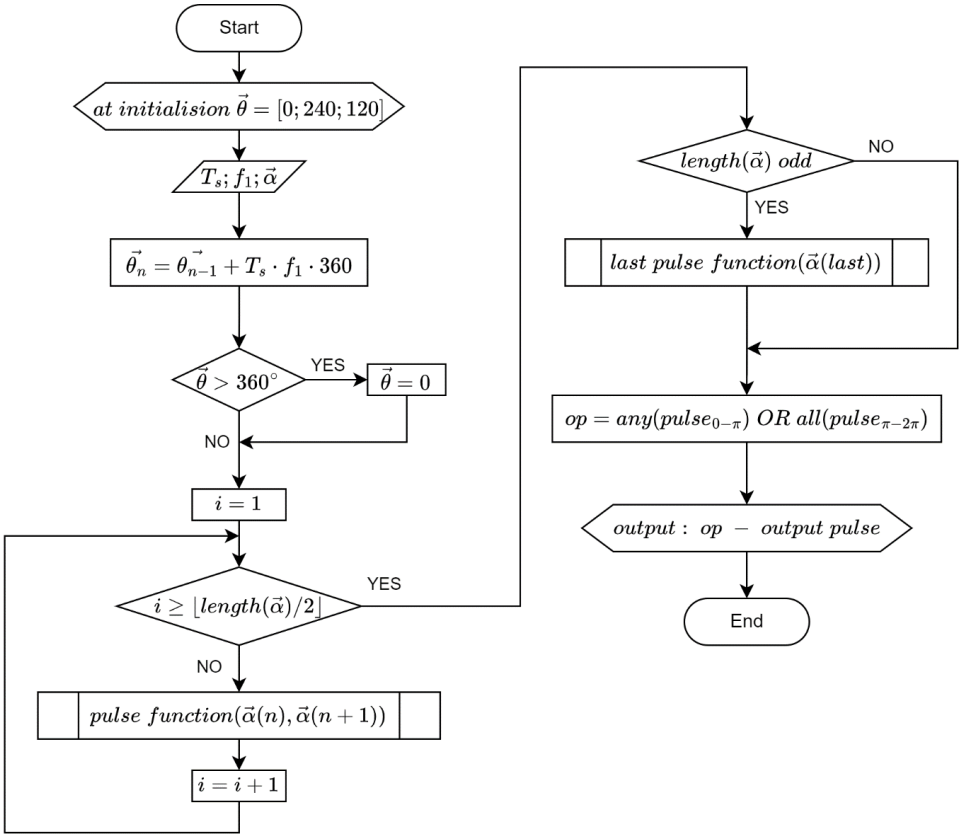

Fig. 2.13. Flowchart of the SHE pulses generation function.

"*Pulse function*" and "*last pulse function*" serve as wrappers for a set of equations shown in Table 2.14. Where (2.21) and (2.22) correspond to "*pulse function*", while (2.23) and (2.24) are for the "*last pulse function*". Equations (2.25) and (2.26) apply to both functions. The first function takes two adjacent angles as input, while the second, executed only when the total number of angles is odd, takes a single angle. Both functions generate output switching pulses based on $\vec{\alpha}(n)$ and/or $\vec{\alpha}(n+1)$ angles

for a signal with quarter-wave symmetry. After these subroutines, outputs for the first and second half-periods are combined into a single Boolean output ("*op*" – output pulse) for the inverter.

Table 2.14 Equations of the Pulse Function

$pls_{0-\pi} =$	$(\theta \geq \alpha_n)\ AND\ (\theta \leq \alpha_{n+1})$ OR $(\theta \geq 180 - \alpha_{n+1})\ AND\ (\theta \leq 180 - \alpha_n)$	(2.21)
$pls_{\pi-2\pi} =$	$(\theta \geq 180 + \alpha_n)\ AND\ (\theta \leq 180 + \alpha_{n+1})$ OR $(\theta \geq 360 - \alpha_{n+1})\ AND\ (\theta \leq 360 - \alpha_n)$	(2.22)
$pls_{0-\pi} =$ (last angle)	$(\theta \geq \alpha_{last})\ AND\ (\theta \leq 180 - \alpha_{last})$	(2.23)
$pls_{\pi-2\pi} =$ (last angle)	$(\theta \geq 180 + \alpha_{last})\ AND\ (\theta \leq 360 - \alpha_{last})$	(2.24)
$out\ pls_{0-\pi} =$	$(pls_{0-\pi}) AND (\theta < 180)$	(2.25)
$out\ pls_{\pi-2\pi} =$	$\overline{(pls_{\pi-2\pi})} AND \overline{(\theta < 180)}$	(2.26)

The SHE pulses generation function is iterative and executed at each time step to create a pulse train suitable for the inverter.

2.4.3. Mode selection and hysteresis

This block is responsible for accurately selecting the correct mode the system is in, taking into account the direction of rotation. PWM transitions only when the reference voltage sinewave crosses zero in the positive direction (phase of 0°) to ensure smooth phase following.

Additionally, a small hysteresis band (0.5–1 Hz) is added to avoid jitter when the system is stable near the transition point. Mode transition points and limiting switching frequency are one of the system inputs and in actual application are chosen based on converter power module losses, in order to stay within junction temperature limits.

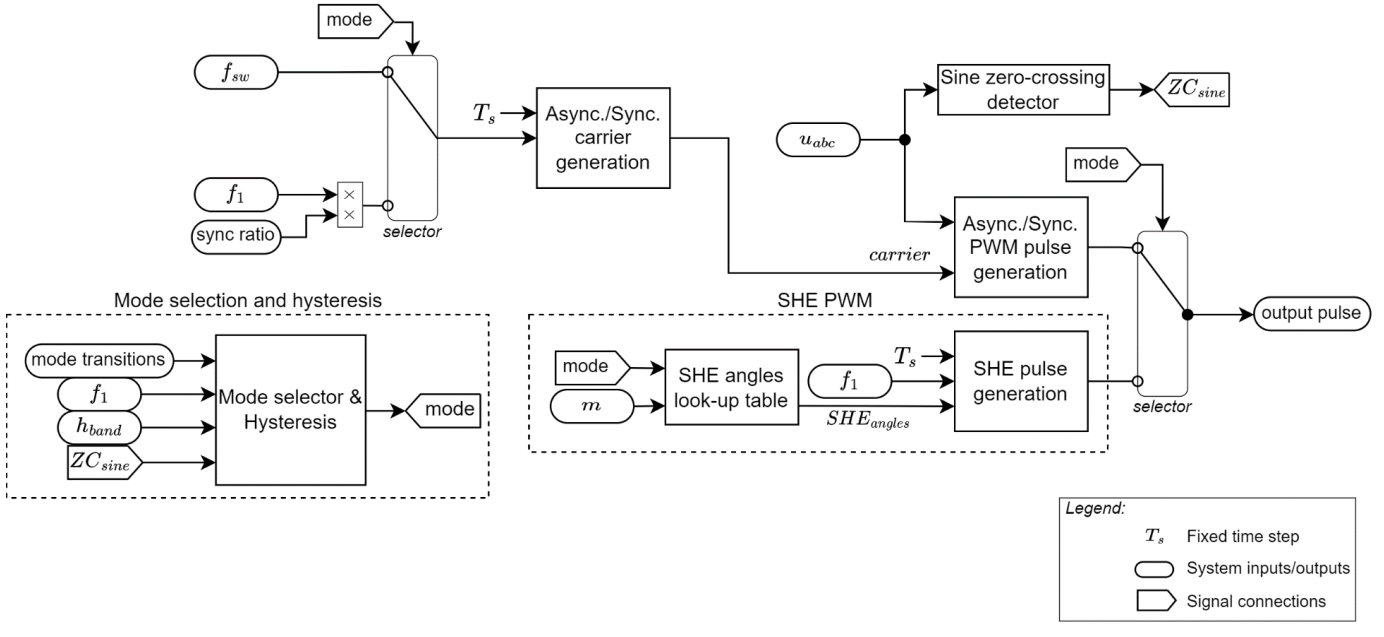

Fig. 2.14. Schematic of the hybrid PWM generation.

2.4.4. Hybrid PWM module overview

The overview of the hybrid PWM module, as shown in Fig. 2.14, indicates that most of the module is developed from the ground up to achieve smooth transition between modulation modes in a fixed-step domain. Additionally, PWM generation algorithms are implemented with custom-made blocks written in code utilizing MATLAB functions. This is done to ease the transition from model to hardware.

Overall system inputs include the reference three-phase sine wave, synchronous frequency, and mode transition points. The system outputs pulses for the converter and the current PWM mode.

2.5. Control system

The control system is the heart of a traction electric drive. The primary objective for traction applications is speed control, with field control in the field-weakening regime at above nominal speeds. There are two methods for controlling AC motors: scalar control and vector control.

The average torque control is a cost-effective variable speed control solution for general-purpose applications, such as fans, blowers, and pump drives, which do not require precise speed or torque control. A typical example of the scalar control method is the constant V/f control. This method can effectively manage motor torque under steady-state conditions, making it suitable for applications with less stringent dynamic performance requirements. However, V/f control has significant limitations when it comes to controlling the motor's dynamic behaviour [86].

The primary disadvantage of V/f control lies in its slow response and extended settling time in both speed and torque control. This sluggish performance is due to the inherent nature of V/f control, where transitioning to a steady state requires the distribution of the torque-forming current and the flux-forming current. In V/f control systems, these processes occur independently and naturally over time. Consequently, this transition period results in poor dynamic performance, which is a characteristic drawback of electric drives utilizing scalar control [87].

To overcome these limitations, there are several types of commonly used control systems. The most commonly used is field-oriented control (FOC) or vector control techniques such as rotor field-oriented control, stator-flux-oriented control, or indirect stator-quantities control. FOC is sensitive to motor parameters, therefor prior knowledge of the parameters and flux estimation should be accurate [88].

Another used paradigm of drive control is direct torque control. It provides a simple structure and is applied in railway traction as well [89], [90]. However, DTC performance degrades especially at low speed and suffers from high torque and flux ripple, variable switching frequency, violence of

polarity consistency rules, and is highly influenced by motor speed [88]. Different variation of DTC with space vector modulation and model predictive control has been attracting research attention [91], [92].

Table 2.15 shows the comparison of main indexes across commonly used and researched control systems that are being used for the electric drive control.

Table 2.15 Comparison of Different Drive Control Techniques [88]

Comparison Index	*FOC*	*DTC*	*DTC-SVM*	*MP-DTC*
Parameter sensitivity	High	Low	Low	High
Computation time	Long	Short	Short	Short
Torque ripple	Low	High	Medium	Medium
Stator flux ripple	Low	High	Medium	High
Stator current THD	Low	High	Medium	Medium
Sampling frequency	Low	High	Medium	Medium
Switching frequency	Fixed	Variable	Fixed	Variable
Dynamic response	Low	Fast	Fast	Fast
Machine losses	Low	High	High	High
PWM modulator	Yes	No	Yes	No
Algorithm complexity	High	Low	Low	High

Based on the above presented comparison FOC system is chosen for the implementation. FOC systems enable precise real-time control of the electric machine's state, significantly enhancing the control system's response speed. While algorithm complexity is not an issue for the modern microcontrollers, and parameters of the machine are always obtained beforehand via testing.

The FOC system requires the fundamental component of the stator current or stator flux as a feedback signal. Such a signal is inherently obtained as part of the modulation algorithm when carrier-based modulation is used [93]. However, in contrast to carrier-based modulation, PPWM strategies do not offer this feature, since the measured and sampled current contains significant harmonic content [28].

Various methods have been developed to estimate the fundamental current component, such as filtering, model-predictive control (MPC), and different observer variations. Filtering is not appropriate for applications requiring high dynamic performance. MPC combined with PPWM is an effective but computationally intensive method, enabling a very fast dynamic response without needing a complex observer [28]. In this case, a simple type of hybrid observer is implemented, which estimates the fundamental current, rotor flux, and torque. The hybrid observer design is based on the work of J. Holtz and N. Oikonomou (2008) [30], with several key improvements and custom code implementations.

This chapter covers three parts:

- Field-oriented control system and overall traction drive schematic
- Hybrid observer
- Control design (tuning of PI controllers)

2.5.1. Field-oriented control

As previously discussed, V/f control has intrinsic limitations. field-oriented control (FOC) overcomes these limitations by providing better dynamic performance through decoupling the effects of the torque and magnetizing flux in the stator current. These decoupled currents are used to independently control torque and maintain magnetization at the required level, making control quite similar to that of a DC machine [94], [95].

FOC operates on the technical principle of transforming a three-phase, time- and speed-dependent system into a rotating (d,q) coordinate system that is time-invariant. This transformation is achieved using mathematical projections, specifically the Park and Clarke transformations. By dealing with instantaneous readings in this transformed frame, FOC ensures precise and accurate control. One of the main advantages of FOC is its ability to reach torque and flux references independently. Torque can be directly controlled by keeping the rotor flux constant and manipulating only the torque component of the stator current vector. This relationship is expressed in equation (2.27) [94], if flux kept constant, torque and quadrature component of stator current are linearly dependent.

$$T \propto \psi_r i_{sq}, \tag{2.27}$$

where T is torque; ψ_r is rotor flux; i_{sq} is quadrature component of the stator current.

The overall structure of the FOC system with a hybrid observer is depicted in Fig. 2.15. The hybrid observer, which is discussed in the next section, plays a crucial role in this setup.

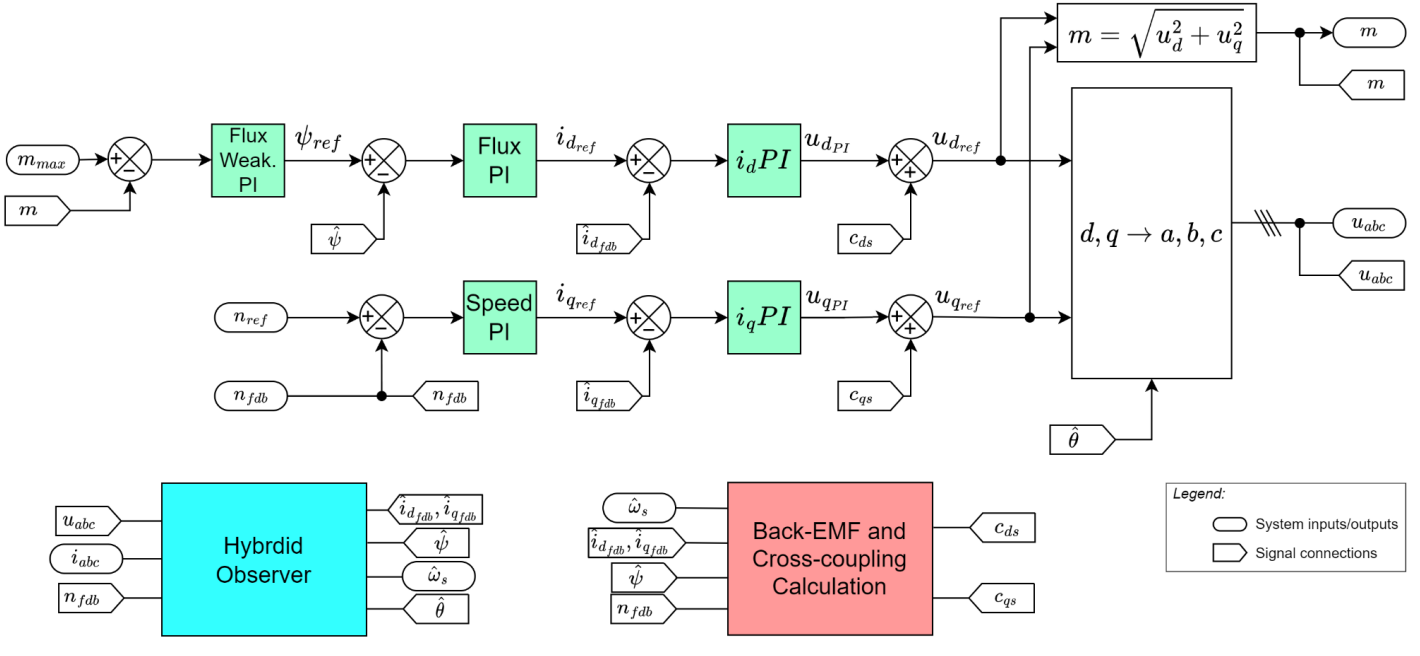

Fig. 2.15. Field-oriented control structure with hybrid observer.

The core of the FOC control system is classical. It takes inputs such as reference speed, measured feedback speed, and measured stator current, and outputs three-phase voltage in per unit along with the modulation index for the PWM modulator. The system includes five PI regulators: for speed, flux, field-weakening, and one for each component of the stator current.

FOC requires precise transformation from the stationary reference frame to the rotor-oriented rotating reference frame. This transformation necessitates an accurate current frequency, which is non-trivial for induction motors due to slip, which is not directly measurable. Typically, a rotor model is used for rotor angle estimation. In this implementation, the rotor angle estimation is incorporated into the fundamental current hybrid observer.

The control system operates with an interrupt rate of 10 kHz, independent of the PWM modulator. This separation is partly because the control system is designed to be deployed on a microcontroller, while the PWM modulator is deployed on an FPGA for higher speed and accuracy, as illustrated in the overall diagram of the electric drive (Fig. 2.16).

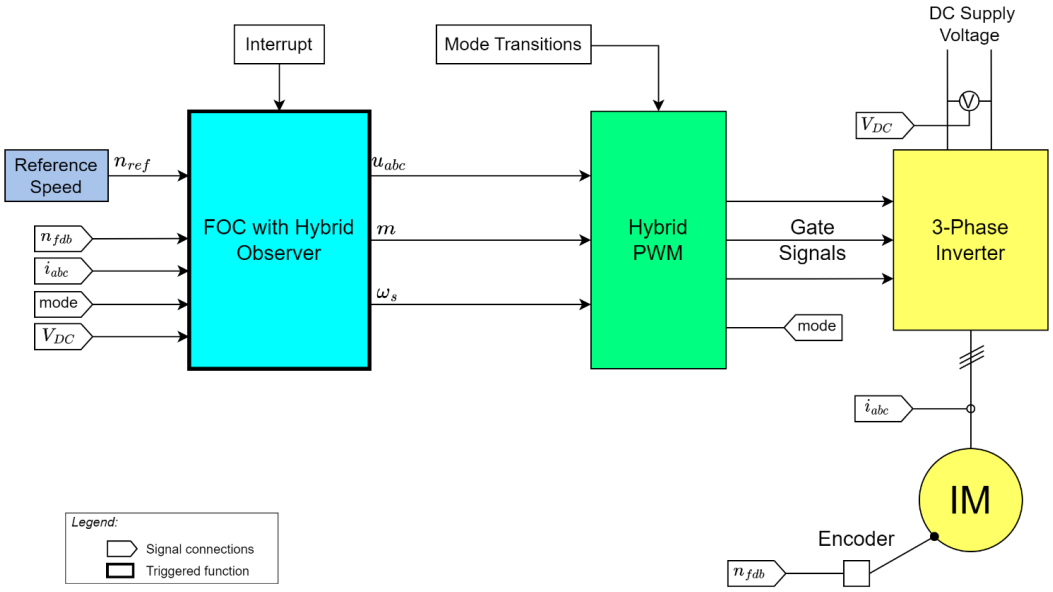

Fig. 2.16. Overview of the electric drive with field-oriented control system.

2.5.2. Back-emf and cross-coupling decoupling

Back-emf and cross-coupling decoupling are also considered in the FOC system. These values, represented by equations (2.28) and (2.29), are part of the voltage equations (2.30) and (2.31). They can act as disturbances for the current controllers or be compensated for, thus making the relationship between the d and q components of the stator current and voltage correspond to an RL load (i.e., a

first-order system) [4]. With proper current regulator designs, accurate, high-bandwidth control of the current is possible. Moreover, the current regulator design is greatly simplified when considering a first-order system.

$$c_{ds} = v_{ccd} + e_d = -\omega_s \sigma L_s i_q - R_r \frac{L_m}{L_r^2} \psi_{rd}, \tag{2.28}$$

$$c_{qs} = v_{ccq} + e_q = \omega_s \sigma L_s i_d + \omega_{mech} \frac{L_m}{L_r} \psi_{rd}, \tag{2.29}$$

$$v_{ds} = R_s' i_d + \sigma L_s \frac{di_d}{dt} + c_{ds}, \tag{2.30}$$

$$v_{qs} = R_s' i_q + \sigma L_s \frac{di_q}{dt} + c_{qs}, \tag{2.31}$$

where R_s, R_r respective active resistances of the stator and rotor, L_m, L_s, L_r respective magnetising, stator, and rotor inductances, $R_s' = R_s + R_r \frac{L_m^2}{L_r^2}$ stator transient resistance, $\sigma = 1 - \frac{L_m^2}{L_s L_r}$ total leakage factor, ω_{mech} angular mechanical velocity of the rotor.

Both c_{ds} and c_{qs} consist of two parts with very different characteristics: the cross-coupling terms (v_{ccd} and v_{ccq}) and the back-emf terms (e_d and e_q). The cross-coupling terms, v_{ccd} and v_{ccq}, can produce large disturbances with very fast dynamics, significantly affecting the current dynamics, especially at high speeds. The q-axis current (responsible for torque) can change rapidly, from zero to its rated value within several milliseconds. On the other hand, e_d and e_q have relatively slow dynamics, as they depend on rotor flux and rotor speed. Rotor flux is either kept constant or changes slowly in the field-weakening regime [4].

Back-emf and cross-coupling terms are incorporated into the control system, as shown in Fig. 2.15, where the calculation block represents the set of formulas depicted in equations (2.28) and (2.29).

2.5.3. Fundamental current hybrid observer

The FOC system for the fast control requires fundamental component of the stator current as a feedback signal. Such a signal is inherently obtained as part of the modulation algorithm when carrier-based space-vector PWM is used. Pre-programmed PWM, such as considered SHE/SHM PWM does not provide a comparable feature. Meaning that by regular sampling it is not possible to acquire fundamental waveform, it will be highly distorted.

To operate FOC a hybrid observer has been implemented for the identification of the fundamental current. The fundamental current hybrid observer used has been introduced by Professor J. Holtz and N. Oikonomou in 2008 [30]. Several modifications were made, while making custom implementation.

Observer hybrid structure is the combination of the stator model in stationary coordinates (2.32) and the rotor model in rotor field coordinate (2.33).

$$\tau_s' \frac{d\hat{\psi}_{s1}}{dt} + \hat{\psi}_{s1} = k_r \hat{\psi}_r + \tau_s' u_s^* + G_s \Delta\psi_s \,, \tag{2.32}$$

$$\tau_r \frac{d\hat{\psi}_r}{dt} + \hat{\psi}_r = -j\hat{\omega}_r \tau_r \hat{\psi}_r + L_m i_s, \tag{2.33}$$

where $\Delta\psi_s = \hat{\psi}_s - \hat{\psi}_{s1}$ is the estimated stator flux error. The state variable of the stator model is the fundamental component $\hat{\psi}_{s1}$ of the stator flux linkage vector. It is derived from the reference voltage vector u_s^* as the input signal.

A voltage vector is a command signal generated by the control signal and fed back to the next calculation step of the observer.

The rotor model operates at field orientation, and hence, $\hat{\psi}_{rq} = 0$ holds. Equation (2.33) then becomes:

$$\tau_r \frac{d\hat{\psi}_{rd}}{dt} + \hat{\psi}_{rd} = L_m \hat{\imath}_{d1}, \tag{2.34}$$

$$\hat{\theta} = \int \left(\frac{L_m \hat{\imath}_{q1}}{\tau_r \hat{\psi}_{rd}} + \omega_{mech} \right) dt, \tag{2.35}$$

$$\hat{T} = \frac{3}{2} \frac{L_m}{L_r} p \, \hat{\psi}_{rd} \, \hat{\imath}_{q1}, \tag{2.36}$$

where first part of the integral is the slip $\hat{\omega}_r$. The rotor flux linkage vector in stationary coordinates $\hat{\psi}_r$ is generated by transforming $\hat{\psi}_{rd}$ from (2.34) to stationary coordinates by means of the estimated rotor field angle $\hat{\theta}$ from equation (2.35). And $\hat{\imath}_{d1}, \hat{\imath}_{q1}$ are transformed values of the estimated fundamental stator current vector by means of $\hat{\theta}$.

The stator flux is obtained using equation below.

$$\hat{\psi}_s = k_r \hat{\psi}_r + \sigma L_s i_s, \tag{2.37}$$

From which estimated stator flux error and consequently error correction signal $G_s \Delta\psi_s$ is computed. G_s is a coefficient that makes the observer robust against disturbances. The precise value is tuned during the testing process.

Main output of the observer is the instantaneous fundamental component of the stator current vector.

$$\hat{\imath}_{s1} = \frac{1}{\sigma L_s} \left(\hat{\psi}_{s1} - k_r \hat{\psi}_r \right) \tag{2.38}$$

The above-described mathematical model of the hybrid observer is shown in Fig. 2.17 in the form of a flow diagram, for better visualization of interconnections. The hybrid observer is

implemented in Simulink in the form of a function and tested. Function is made in a way to easily adapt it to microcontroller implementation. Testing is described in chapter 3.

Where above equations utilize following parameters:

$\tau_s' = \sigma L_s / R_s$ transient time constant of the stator

$k_r = L_m / L_r$ coupling factor of the rotor

$\tau_r = L_r / R_r$ rotor time constant

ω_r rotor (slip) frequency

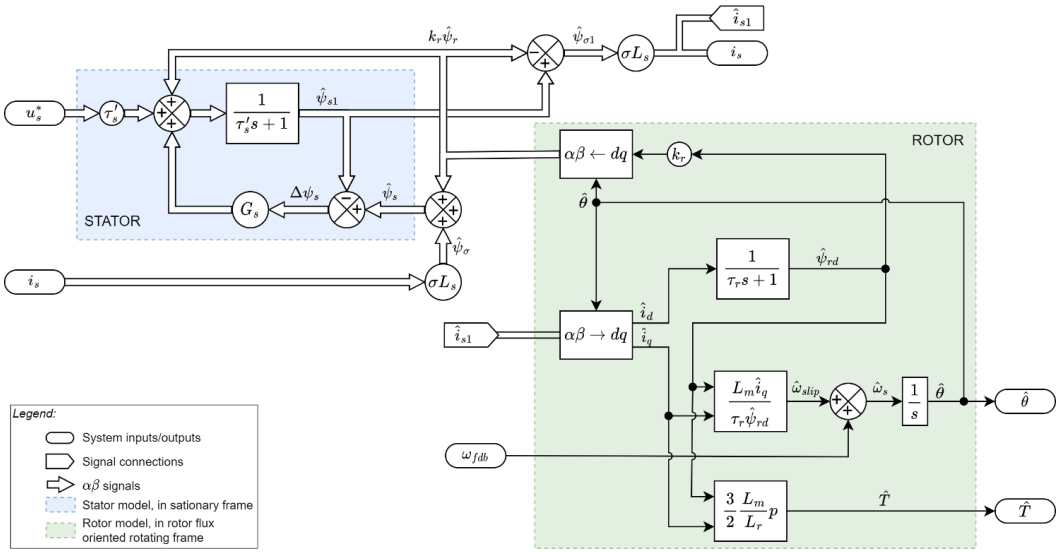

Fig. 2.17. Flow diagram of the hybrid observer.

As a summary the hybrid observer function has:

Inputs: measured stator current i_s, command voltage vector u_s^* and measured mechanical speed ω_{mech}.

Outputs: direct and quadrature estimated stator currents $\hat{\imath}_{ds1}, \hat{\imath}_{qs1}$, rotor flux $\hat{\psi}_{rd}$, electromagnetic torque $\hat{T}$, synchronous speed $\hat{\omega}_s$, and rotor angle $\hat{\theta}$.

2.5.4. Controller design

A proper control system design requires precise tuning of the controllers used to generate voltage commands for the frequency inverter. PI regulators implemented in a synchronous reference frame are widely accepted as the standard solution for current regulation in vector-controlled AC drives [4]. Proper tuning of these PI controllers, based on a thorough understanding of the machine model, is crucial for the stable operation of the traction electric drive across all operating regimes.

As seen in the Fig. 2.15 the system under consideration has two parallel feedback control loops; each loop has two cascades.

- Loop 1: A d-axis current controller and a flux controller, with a field-weakening controller acting above the nominal point.
- Loop 2: A q-axis current controller and a speed controller.

In a control system with cascaded feedback loops, the analysis typically begins with inner loops, which are then progressively reduced to simplify the system to a single closed-loop transfer function [96]. This reduction is feasible because the time constants of the inner (current) and outer loops (speed and flux) differ significantly for most types of electric machines due to the physical nature of the mechanical systems, thereby simplifying the tuning process. Parallel loops of flux and speed are also considered separately because decoupling is performed to separate the effects of each other to a minimum and simplify the control system design.

The design of a field-oriented control system involves three general steps:

- tuning of d- and q-axis stator current controllers;
- tuning of speed controller (just motor, and with a vehicle);
- tuning of flux controller.

The d- and q-axis controllers use the same set of gains because the induction motor exhibits similar dynamics for both d- and q-axis currents. The controller design involves selecting the controller type (in this case all regulators are PI) and defining the optimal settings. The parameters are chosen according to established criteria. The optimal modulus criterion (OMC) and optimal symmetry criterion (OSC) are commonly used in power electronics and drive control practices. The OMC is used for tuning the inner loop, while the OSC is usually applied to the outer loop [97], [98]. However, in this case the response of the outer loop is selected directly based on the desired bandwidth and damping of the system [4].

The control design approach and methodology are based on references [4], [96], [97], [98].

Control design, calculations and visualizations are made in MATLAB with the Control System Toolbox. The transfer function is created using '*tf*', step response is obtained using the '*step'* function, custom input system response is done with *'lsim'* function, and information about overshoot and settling time with '*stepinfo*', closed-loop transfer function for step response calculation is constructed using the '*feedback*' function.

2.5.4.1. Design of d-/q-axis current controllers

Tuning of the synchronous PI current regulators can be addressed using well-known tools for linear systems. If ideal decoupling of the effects due to cross-coupling and the back-emf is assumed, the dynamic behaviour of the d and q axis currents is given by equation (2.39) [4].

$$\frac{i_d(s)}{v_d(s)} = \frac{i_q(s)}{v_q(s)} = \frac{1}{\sigma L_s s + R'_s} \tag{2.39}$$

Current control loop is shown in Fig. 2.18. To work with unitary feedback, the transfer function placed in the feedback should be moved according to the transformation theorems [96]. The result of transformation is shown in Fig. 2.19.

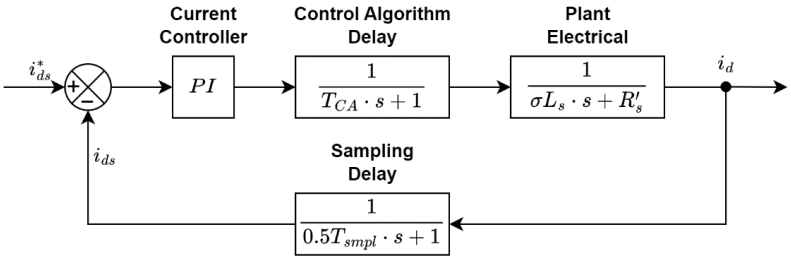

Fig. 2.18. Current controller loop.

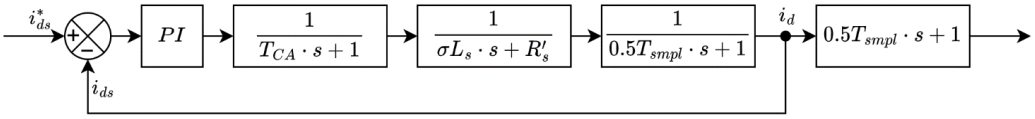

Fig. 2.19 . Current controller loop with unitary feedback.

The transfer function of the PI controller is shown in equation (2.40).

$$G_{PII}(s) = \frac{C(s)}{R(s)} = k_{pi} + \frac{k_{ii}}{s} = k_{pi} \cdot \frac{1 + T_{ii}s}{T_{ii}s}, \tag{2.40}$$

where $G(s)$ is a product of all transfer functions along forward path, $R(s)$ is a reference input, and $C(s)$ is a controlled output, k_{pi} is proportional gain, k_{ii} is integral gain, and $T_{ii} = \frac{k_{pi}}{k_{ii}}$ is an integrator time constant.

The control algorithm block and sampling block are similar. Control algorithm is a delay introduced due to the digital calculation (interrupt of the DSP), while sampling block as the name suggests due to the analogue signal sampling and it depends on the chosen PWM strategy. Transfer functions are shown in equation (2.41).

$$G_{CA}(s) = \frac{1}{T_{ca}s + 1};\ G_{smpl}(s) = \frac{1}{T_{smpl}s + 1} \tag{2.41}$$

The plant (model of the induction machine, electrical part) transfer function for the analysis is a continuation of the equation (2.39) in a general transfer function form shown in equation (2.42).

$$G_P(s) = \frac{i(s)}{u(s)} = \frac{1}{\sigma L_s s + R_s'} = \frac{1}{R_s'} \cdot \frac{1}{1 + s\frac{\sigma L_s}{R_s'}} = \frac{1}{R_s'} \cdot \frac{1}{1 + sT_{sI}}, \tag{2.42}$$

where $R_s' = R_s + R_r \frac{L_m^2}{L_r^2}$ is stator transient resistance, $L_s = L_m + L_{\sigma s}$ is stator inductance, $\sigma = 1 - \frac{L_s L_r}{L_m^2}$ is total leakage factor, and T_{sI} is electrical time constant of the motor.

Overall transfer function of the current controller loop is shown in equation (2.43), and is obtained by multiplication of components.

$$G_{OLI}(s) = G_{PII(s)} \cdot G_{CA}(s) \cdot G_{smpl}(s) \cdot G_P(s). \tag{2.43}$$

A simple and effective way to select the gains for the current regulator is to use the zero of the regulators to cancel the dynamics of the load. For that purpose, OMC strategy is used, and controller values are defined as:

$$\begin{aligned} k_{pi} &= \frac{T_{sI}}{2T_{eqvI}K_P}, \\ T_{ii} &= T_{sI}, \end{aligned} \tag{2.44}$$

where $K_P = \frac{1}{R_s}$, T_{eqvI} is the equivalent time constant equal to the sum of all the constants in the system, excluding the machine electrical time constant. Such simplification is made for easier calculation, this simplification could be made because all other time constants are substantially faster than electrical time constant of the machine. In this case it can is:

$$T_{eqvI} = T_{CA} + 0.5T_{smpl}. \tag{2.45}$$

Considering equations presented values for the PI controller are: $k_{pi} = 1.62, \frac{1}{T_{ii}} = 75.4\ Hz$, when $T_{CA} = \frac{1}{735\ Hz} = 1.36\ ms$, $T_{smpl} = \frac{1}{10\ kHz} = 0.1\ ms$, and motor values are taken from Table 2.7. Control algorithm frequency is an average expected switching frequency of 735 Hz in of the speed range, as it will be shown in chapter 3 Fig. 3.1.

Below in the Fig. 2.20 is the step response of the current controller. Time constant is 13.3 milliseconds, settling time is 12.5 milliseconds, overshoot is 4.9%, and rise time is 4.3 milliseconds. These values are satisfactory for a rather slow system using SHE PWM.

It is noted in this regard that even if the pole-zero cancellation described by (2.44) is not ideal, this does not normally produce a significant deterioration of the current regulator response and does not affect its stability, as the system pole is located in the stable half of the s plane, and relatively far from the origin [4].

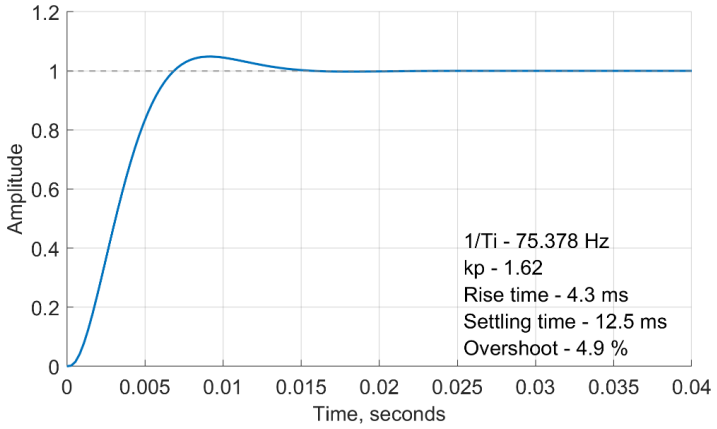

Fig. 2.20. Step response of the current controller.

2.5.4.2. Design of speed controller

Once the inner current controller loop is tuned with the desired performance, the outer controller can also be tuned. The structure of the speed loop in shown in Fig. 2.21, and the transformed loop to the one with unitary feedback in the Fig. 2.22.

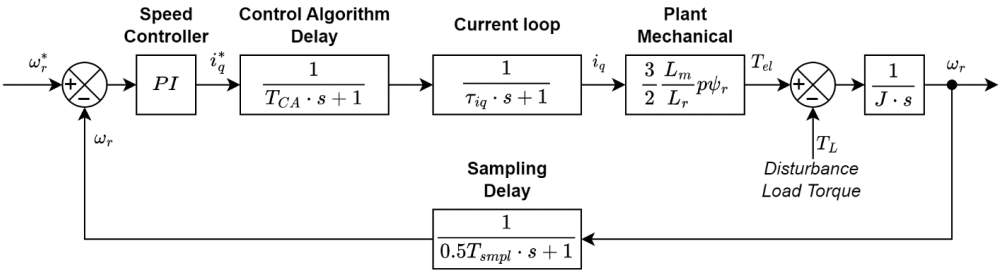

Fig. 2.21. Speed controller loop.

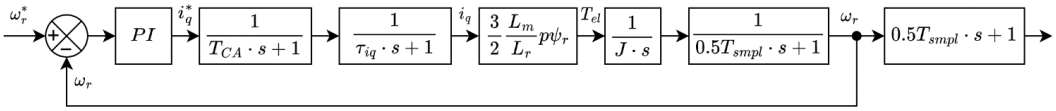

Fig. 2.22. Speed controller loop with unitary feedback.

The transfer function of the PI controller is the same as with current controller, just with different naming:

$$G_{PIn}(s) = \frac{C(s)}{R(s)} = k_{pn} + \frac{k_{in}}{s} = k_{pn} \cdot \frac{1 + T_{in}s}{T_{in}s}. \tag{2.46}$$

The effect of the inner current loop must be considered. This effect can be modelled as a first order system [97], acting as a delay. It is applicable to assume it that way, as the bandwidth of current

and speed/flux controllers should sufficiently different from each other, usually outer controller is at least 10 times slower.

$$G_{is}(s) = \frac{1}{\tau_{iq}s + 1}, \tag{2.47}$$

where $\tau_{iq} = \frac{T_{ii}}{k_{pi}k}$.

The mechanical speed of the motor ω_m is determined from the mechanical equation [86]:

$$\begin{aligned} T_{el} - T_L &= Js\omega_m + K_F\omega_m, \\ T_{el} &= \frac{3}{2}\frac{L_m}{L_r}p\psi_r i_q = K_T i_q. \end{aligned} \tag{2.48}$$

The equation (2.48) is transformed into a transfer function of mechanical system (2.49) [4]. Where T_L load torque is a disturbance in the system, J inertia of the electrical machine, K_F viscous friction coefficient. While viscous friction coefficient is mostly negligible in big electrical machines. Values are taken from Table 2.8.

$$G_{Pn}(s) = \frac{\omega(s)}{T_{el}(s)} = \frac{1}{Js + K_F} \cong \frac{1}{Js}. \tag{2.49}$$

The open-loop transfer function of the speed loop is shown below:

$$G_{OLn}(s) = k_{pn}\frac{1 + T_{in}s}{T_{in}s} \cdot \frac{1}{T_{CA}s + 1} \cdot \frac{1}{\tau_{iq}s + 1} \cdot \frac{1}{0.5T_{smpl}s + 1} \cdot K_T \cdot \frac{1}{Js}. \tag{2.50}$$

To simplify the open loop transfer function, an equivalent time constant is assumed as:

$$T_{eqvn} = T_{CA} + 0.5T_{smpl} + \tau_{iq}, \tag{2.51}$$

As these time constants are substantially slower. Additionally, K_F can be neglected as it is usually very small. After simplification the open loop transfer function becomes:

$$G_{OLn}(s) = \frac{(1 + T_{in}s)K_T k_{pn}}{JT_{in}s^2\left(T_{eqvn}s + 1\right)}. \tag{2.52}$$

To design PI controller for this transfer function OSC could be used or, as done in this case direct tuning approach could be used using a simplified transfer function linking the actual speed with the speed command [4], while selecting bandwidth substantially slower than T_{eqvn}. In this case speed is mechanical in rad/s.

$$\frac{\omega_n(s)}{\omega_n^*(s)} = \frac{k_{pn} \cdot s + k_{in}}{J \cdot s^2 + \left(K_F + k_{pn}\right) \cdot s + k_{in}}. \tag{2.53}$$

To select controller coefficients the natural frequency and damping coefficients for the second order system are specified.

$$k_{in} = J \cdot \omega_n^2, \tag{2.54}$$

$$k_{pn} = J \cdot 2\xi\omega_n,$$

$$T_{in} = \frac{k_{pn}}{k_{in}} = \frac{2\xi}{\omega_n}.$$

There are different ways to select the natural frequency and damping coefficients, however in this case commonly used damping factor of $\xi = 0.707$ is used and natural frequency is selected in a way that time constant and/or rise time is approximately 10 times slower than the current controller time constant.

In this case $\omega_n = 10\ rad/s$. Below in the Fig. 2.23 is the step response of the speed controller. Time constant is 141.4 milliseconds, settling time is 476.1 milliseconds, overshoot is 22.3%, and rise time is 78.5 milliseconds. The time constant is 10.6 times slower than the current controller, which is satisfactory, while the overshoot is within the expected value of 30%.

This overshoot value is acceptable, as in a real application the rise time is limited by the traction characteristic. In other words, the output of the speed controller goes into saturation to avoid exceeding current limits, thus making the dynamics slower.

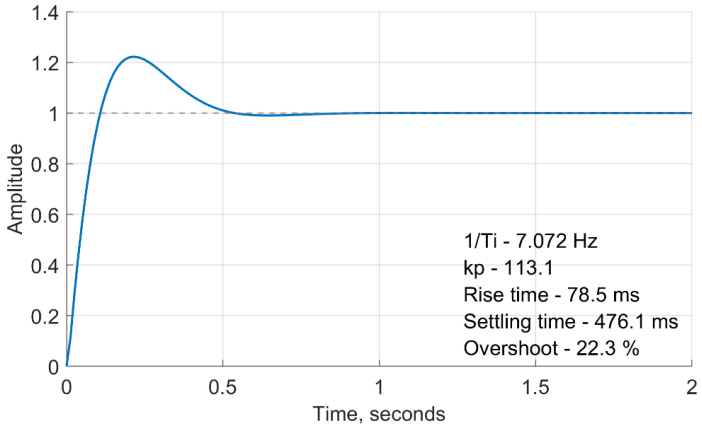

Fig. 2.23. Step response of the speed controller.

2.5.4.3. Design of speed controller (with EMU)

The design of the speed controller, when connected to a vehicle (EMU) is done according to the previous section, with the only change to the transfer function of the plant.

The transfer function of the plant (EMU) is the linking of vehicle speed in rad/s and input torque in Nm. The transfer function input and output are the same as with motor mechanical plant as shown in equation (2.49). The transfer function is derived from Newton's second law of motion and relation between vehicle speed and motor shaft speed through the gearbox. Below is the vehicle transfer function.

$$G_{Pvehicle}(s) = \frac{\omega(s)}{T_{el}(s)} = \frac{1}{\left(\frac{D/2}{\mu}\right)^2 \cdot \frac{1}{\eta_{gb}} \cdot m \cdot (1+\gamma) \cdot s}, \tag{2.55}$$

where D is wheel diameter, μ is gearbox ratio, η_{gb} is gearbox efficiency (in this case average value of 0.975 is used), m is vehicle mass referred to a single motor, and γ is inertial mass ratio. All values are taken from the chapter 2.2.3.

Considering numerical values transfer function has following form:

$$G_{Pvehicle}(s) = \frac{\omega(s)}{T_{el}(s)} = \frac{1}{\left(\frac{0.85/2}{5.89}\right)^2 \cdot \frac{1}{0.975} \cdot 38900 \cdot (1+0.08) \cdot s} = \frac{1}{224.3 \cdot s}, \tag{2.56}$$

while that transfer function for the motor was $G_{Pn}(s) = \frac{1}{J \cdot s} = \frac{1}{8 \cdot s}$.

Based on this controller coefficients are recalculated with the same damping factor ($\xi = 0.707$) and bandwidth ($\omega_n = 10\ rad/s$). Could be seen that with and without vehicle controller performance does not change, while only proportional constant changes $k_p = 3172$, which is a scaled-up coefficient when system operates with just a motor $\frac{3172}{113.1} = \frac{224.3}{8} = 28$.

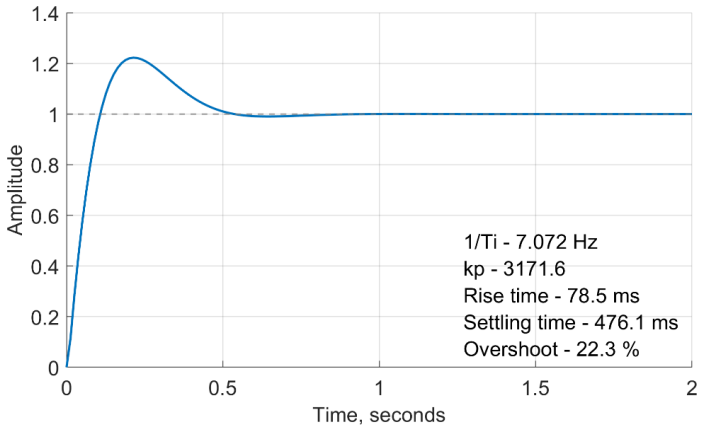

Fig. 2.24. Step response of the speed controller (with vehicle).

In the real traction application system response, and more specifically overshoot is governed by the traction characteristic. Using 'lsim' MATLAB function allows to make a system response with an arbitrary input. Based on that, theoretical speed controller system response to the traction characteristic input up to the nominal speed was calculated.

Traction characteristic system response is shown in Fig. 2.25. Could be seen that reference speed is 50 km/h with the maximum speed of 50.15 km/h, making system overshoot 0.3 %, which is perfectly acceptable for the railway traction application.

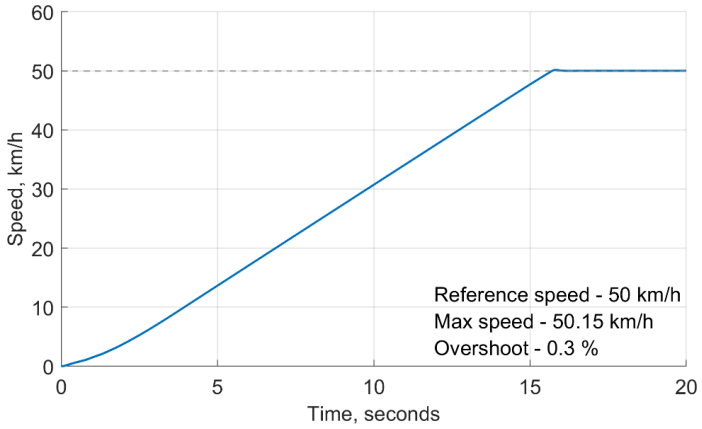

Fig. 2.25. Traction characteristic response of the speed controller (with vehicle).

2.5.4.4. Design of flux controller

When flux control loop is implemented in practice flux is always an estimated value, in the case of this research it is an output of the hybrid observer. And obviously, the performance of the rotor flux control loop will be conditioned by the accuracy of the observer.

Similar to the tuning of the speed controller, it is assumed that the current loop bandwidth is tuned to be much faster than the rotor flux loop [4]. Thus, the dynamics of the current controller is neglected, and current controller induced delay is used as in (2.47). It should be noted that perfect rotor flux estimation has been assumed.

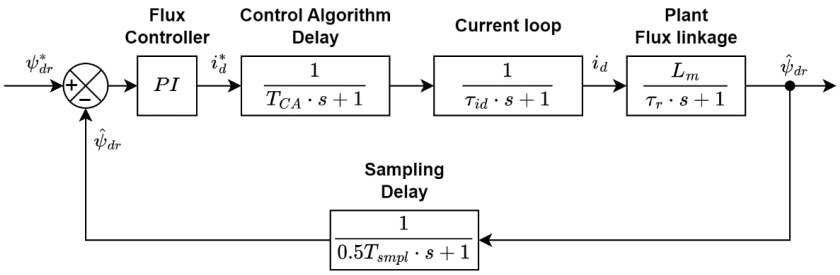

Fig. 2.26. Flux controller loop.

Design of flux controller is made in a similar way to the speed controller procedure. Flux controller loop is shown in Fig. 2.26. For the analysis sampling delay is put on the forward path in the same way as in Fig. 2.19 and Fig. 2.22.

The PI controller transfer function is as follows:

$$G_{PIf}(s) = \frac{C(s)}{R(s)} = k_{pf} + \frac{k_{if}}{s} = k_{pf} \cdot \frac{1 + T_{if}s}{T_{if}s}. \tag{2.57}$$

Plant model of the field component of the induction machine is shown in equation (2.58) [4].

$$G_{Pf}(s) = \frac{\psi(s)}{i(s)} = \frac{L_m}{\frac{L_r}{R_r}s + 1} = \frac{L_m}{\tau_r s + 1}. \tag{2.58}$$

The open-loop transfer function of the flux loop is shown below:

$$G_{OLf}(s) = k_{pf}\frac{1 + T_{if}s}{T_{if}s} \cdot \frac{1}{T_{CA}s + 1} \cdot \frac{1}{\tau_{id}s + 1} \cdot \frac{1}{0.5T_{smpl}s + 1} \cdot \frac{L_m}{\tau_r s + 1}. \tag{2.59}$$

Simplification of the $G_{OLf}(s)$ transfer function is done in the same way as in (2.51). Leading to simplification of the open-loop transfer function:

$$G_{OLf}(s) = \frac{(1 + T_{if}s)L_m k_{pf}}{(\tau_r s + 1)T_{if}s(T_{eqvf}s + 1)}. \tag{2.60}$$

To design PI controller for this transfer function OSC could be used or, as done in this case direct tuning approach is used using a simplified transfer function linking the estimated using hybrid observer flux with the flux command [4].

$$\frac{\hat{\psi}_d}{\psi_d^*} = \frac{k_{pf} \cdot s + k_{if}}{\frac{\tau_r}{L_m} \cdot s^2 + \left(\frac{1}{L_m} + k_{pf}\right) \cdot s + k_{if}}. \tag{2.61}$$

To select controller coefficients the natural frequency and damping coefficients for the second order system can be specified. Controller coefficients are calculated in the following manner [4]:

$$\begin{aligned} k_{if} &= \frac{\tau_r}{L_m}\omega_n^2, \\ k_{pf} &= \frac{\tau_r}{L_m}2\xi\omega_n - \frac{1}{L_m}, \\ T_{in} &= \frac{k_{pf}}{k_{if}}. \end{aligned} \tag{2.62}$$

There are different ways to select the natural frequency and damping coefficients, however in this case commonly used damping factor of $\xi = 0.707$ is used and natural frequency is selected in a way time constant and/or rise time is at least 10 times slower than the current controller time constant. The approach to the design is the same as with the speed controller.

In this case $\omega_n = 9\,rad/s$. Below in the Fig. 2.27 is the step response of the flux controller. Time constant is 134.4 milliseconds, settling time is 540.8 milliseconds, overshoot is 16.3%, and rise time is 105.9 milliseconds. Time constant is 10.1 times slower than the current controller, which is satisfactory.

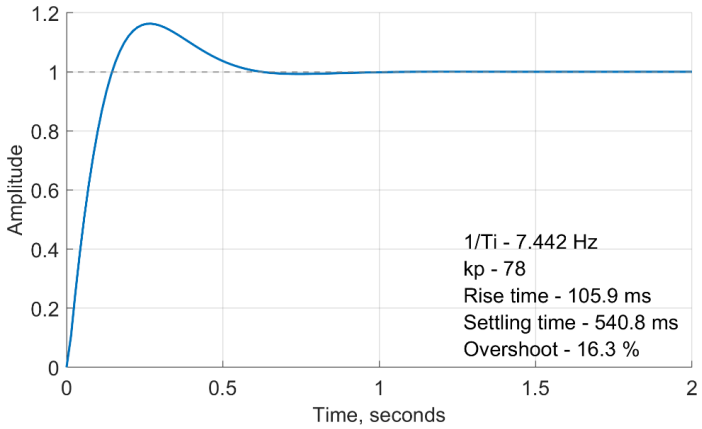

Fig. 2.27. Step response of the flux controller.

In a real application, the rise time is limited by a rate limiter, as changes to the flux reference occur infrequently or gradually. This typically happens during the magnetization of the motor or during field-weakening operation. Flux-weakening is managed by a feedback-based field-weakening controller, which gradually provides updated flux references for the flux controller.

2.5.4.5. Feedback-based field weakening controller

Alternatively, to feed-forward-based flux-weakening methods, a feedback-based strategy can be used. This method does not require the use of a machine model or pre-calculated look-up tables. Instead, the voltage command provided by the current regulator is used to dynamically adapt the flux reference to the machine speed [4].

As shown in Fig. 2.15, the input to the flux-weakening regulator is the difference between the modulation index of the current regulator and the maximum set modulation index. Although the actual output voltage of the current regulators is in volts, for the feedback-based field-weakening controller, it is recalculated to actual modulation index per unit values based on the measured DC-link voltage, according to the equation below [86]:

$$m = \frac{V_{1peak}}{V_{DC}/2} = \frac{\sqrt{u_d^2 + u_q^2}}{V_{DC}/2}, \tag{2.63}$$

and reference voltage limit is set according to equation below:

$$m_{max} = \frac{V_{1rms_{ref}} \cdot \sqrt{2}/\sqrt{3}}{V_{DC}/2}, \tag{2.64}$$

where V_{1peak} is amplitude of the 1st harmonic of the phase voltage, u_d, u_q are voltage references as outputs of the d-/q- axis current controllers, V_{DC} is DC-link voltage, $V_{1rms_{ref}}$ is reference maximum RMS line voltage (1st harmonic), $\sqrt{3}$ is line to phase voltage conversion coefficient, $\sqrt{2}$ is RMS of the sine wave to peak value conversion coefficient.

Before reaching nominal voltage, this controller does not engage; only upon reaching the voltage limit does it start to lower the flux reference below nominal. Tuning the flux-weakening regulator is not straightforward. Its bandwidth should be significantly lower than the current regulator bandwidth to prevent interference. However, due to this, in scenarios of fast speed variations, the performance of this loop may exhibit oscillatory behaviour [4].

As there is no state variable to control it is difficult to tune this controller. Time constant of the controller was chosen equal to the flux controller's time constant $T_{ipf} = 7.44$, while proportional gain was chosen as the value of nominal flux in Vs equal to $k_{pfw} = 2.7\ Vs$ as it links per unit modulation index in the range 0…1.15 and flux in Vs.

2.5.4.6. Summary of the controller coefficients

The final section summarizes the results of the design process in tabular form (Table 2.16) for at a glance understanding of the controller parameters and its performance.

Table 2.16 Summary of the Controller Coefficients

Controller	T_i	$k_i = \frac{k_p}{T_i}$	k_p	Rise time	Settling time	Overshoot
d-/q- current	13.3 ms	121.8	1.62	4.3 ms	17.4 ms	4.9 %
Speed (motor)	141.4 ms	800	113.1	78.5 ms	476.1 ms	22.3 %
Speed (EMU)		22470	3177			
Flux	134.4 ms	580	78	105.9 ms	540.8 ms	16.3 %
Field-weakening	134.4 ms	20.1	2.7			

3. Simulation of Traction Drive System with Hybrid PWM

This subchapter delves into in-depth simulation of the traction drive model with designed control system. It aims to assess the performance and capabilities in both static and transient regimes of operation, as well as to verify the stability of the control system before proceeding to laboratory tests.

Several test categories were carried out:

1) The stator current harmonic content and power module losses:
   - modulation performance in static regime;
   - comparison of SHE and synchronous PWM performance;
   - performance of different SHE solutions.
2) Tests without train with static load:
   - flux response;
   - acceleration-deceleration;
   - PWM transitions performance;
   - hybrid observer performance;
   - torque application at different speeds.
3) Tests with model of EMU:
   - PWM transitions performance in acceleration-deceleration under traction characteristic.

All tests have identical hybrid PWM transition types and points of transition, unless otherwise specified. Parameters of each PWM mode are summarized in Table 3.1 and Fig. 3.1 shows the hybrid PWM transitions scheme in visual form.

Table 3.1 Hybrid PWM Transitions Scheme

PWM mode	**Switching frequency**	**Fundamental frequency range**
Asynchronous	820 Hz	0…22 Hz
Synchronous 27	594…918 Hz	22…34 Hz
SHE 9, Solution 1	646…919.6 Hz	34…48.4 Hz
SHE 7, Solution 1	726…919.5 Hz	48.4…61.3 Hz
SHE 5, Solution 1	674.3…919.6 Hz	61.3…83.6 Hz
SHE 3, Solution 1	585.2…919.8 Hz	83.6…131.4 Hz
SHE 1	394.2…480 Hz	131.4…160 Hz

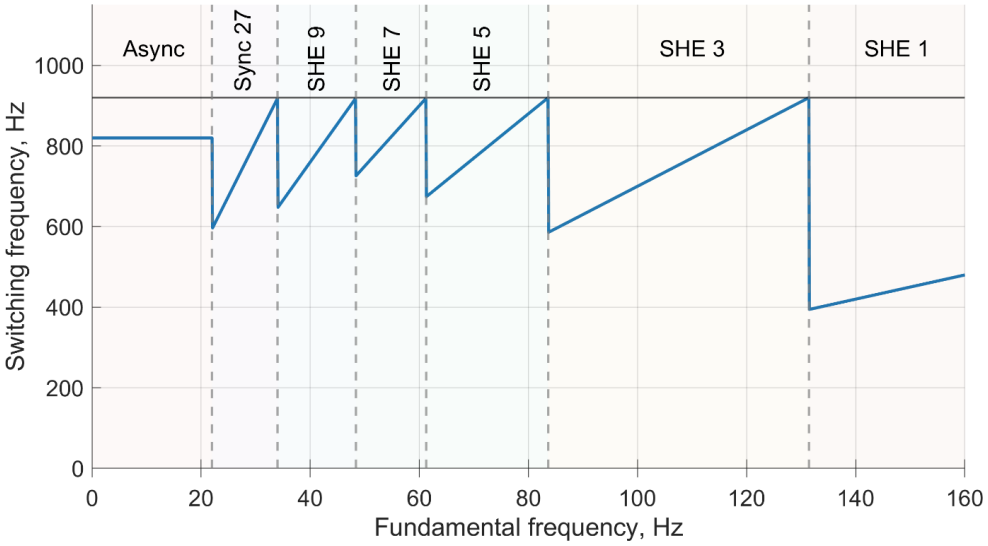

Fig. 3.1. Hybrid PWM transitions scheme (used in simulation).

Additional overarching parameters:

- PWM transitions hysteresis band: 1 Hz;
- hybrid observer G_s gain: 0.75;
- reference nominal flux: 2.75 Vs;
- minimum allowed flux in field-weakening regime: 10% of nominal – 0.275 Vs;
- field-weakening modulation index limit – m=1.09, which at 3500 VDC corresponds to 2340 V_{1RMS}, where relation $V_{1rms} = m \cdot \frac{V_{DC}}{2} \cdot \frac{\sqrt{3}}{\sqrt{2}}$ [86]. $\sqrt{3}$ is phase voltage to line voltage conversion coefficient, $\sqrt{2}$ is peak value to rms for pure sine wave conversion coefficient;
- during calculation of the power converter losses junction temperature was set to $T_j = 125°C$, which corresponds to the maximum operation junction temperature according to the datasheet.

Simulink model modelling solver parameters:

- type: fixed-step;
- solver: ode4 (Runge-Kutta);
- fixed-step size: 10 microseconds.

All consequent modelling was carried out in MATLAB version 23.2 R2023b Update 7.

3.1. Analysis of stator current harmonic content and converter losses

This subchapter focuses on harmonic analysis of the induction motor stator current and power converter losses in static operation. Several tests were carried out to depict the THD, WTHD and converter losses, while outlining the differences between modulation modes. Transition points and SHE solutions are used as outlined in Table 3.1, unless otherwise specified.

In each test analysis of the harmonic content is done based on a 4 second snapshot of the signal with sampling rate of 20 kHz, recorded from the Simulink model. As the calculation of the THD, and WTHD requires static regime with at least 20 fundamental periods to achieve good results [99]. With the speeds above 150 RPM it holds true with 4 second snapshot. Below 150 RPM snapshot duration is increased proportionally.

The analysis is done using the FFT functionality of MATLAB, after that for visualisation and comparison purposes harmonic grouping was done based on IEC 61000-4-7:2002 standard [100]. Each signal is analysed with integer harmonic order grouping, from 1st to 50th harmonic.

Total harmonic distortion (THD) and weighted total harmonic distortion (WHTD) are calculated in the following manner:

$$THD = \sqrt{\frac{\sum_{n=2}^{\infty} x_n^2}{x_1}}, \tag{3.1}$$

$$WTHD = \sqrt{\frac{\sum_{n=2}^{\infty} \left(\frac{x_n}{n}\right)^2}{x_1}}, \tag{3.2}$$

where n is the harmonic order, x_n is the waveform amplitude at nth harmonic order.

THD and WTHD calculations are done according to the study of D. Holmes and T. Lipo (2003) [32]. THD is the most common measure of waveform distortion, while WTHD is more useful in comparing different switching algorithms, as it takes into consideration the value of each harmonic as a weight, as the further the harmonic is from the fundamental the lesser effect it has on losses in the induction motor. However, it is useful only in comparison to other PWM regimes.

Additionally, stator current fundamental harmonic amplitude (I_1), and harmonic current content component up to the 50th harmonic ($I_{2\ldots50}$) are shown in each test.

$$I_{2\ldots50} = \sqrt{\sum_{2}^{50} I_n^2}. \tag{3.3}$$

Harmonics are considered and analysed up to the 50th order, as above that effect on losses and WTHD is almost negligible.

Power module constituent losses are calculated according to the description in the chapter 2.3.1.

3.1.1. Overview of modulation performance in static regime

The first test is a representation of harmonics and losses in each modulation regime in static conditions. The model was tested at 7 speed reference points and in 3 loading conditions. This test serves as a baseline test for the operation of the PWM module. It aims to provide harmonic content and specific harmonics in each regime and constituent power module losses, while setting the stage for further tests and comparison.

Table 3.2 provides an overview of used reference points.

Table 3.2 Overview of Reference Points

PWM mode	**Reference speed, RPM**	**Reference torque, Nm | Switching frequency, Hz**					
		No-load (A)		0.5 TrChar (B)		TrChar (C)	
Asynchronous (1)	600	0	820	1500	820	3000	820
Synchronous 27 (2)	900	0	810	1500	831	3000	852
SHE 9 (3)	1200	0	760	1500	775	3000	789
SHE 7 (4)	1650	0	825	1500	837	3000	848
SHE 5 (5)	2100	0	770	1228	777	2456	784
SHE 3 (6)	3000	0	700	859	706	1718	714
SHE 1 (7)	4200	0	420	484	423	968	427

TrChar is the traction characteristic reference from Fig. 2.3. Loadings conditions: no-load marked as (A), 50 % of traction characteristic reference marked as (B), and full traction characteristic reference marked as (C). The left column shows the reference torque, and the right column shows the switching frequency. PWM modes are marked (1) through (7) correspondingly for more concise naming in the following tables.

In the Table 3.2 could be noted that the switching frequency changes slightly in synchronous PWM and SHE PWM since it is synchronized with the fundamental frequency, while speed reference is the rotor frequency lowered from synchronous frequency by a slip of the motor.

Table 3.3 outlines the stator current performance indicator of the stator current in each modulation regime and at each loading condition, while Fig. 3.2 provides FFT with integer grouping of up to the 50^{th} harmonic. While visual representation of the stator current with 2 periods each is depicted in Appendix B to help represent the difference between regimes, and how prominent are the current harmonics.

From the current performance indicators, it could be seen that at fully loaded conditions THD and WTHD are not that high, with relatively low values of harmonic content. However, harmonic content stays relatively consistent, despite the load. Meaning that at no-load harmonic values are comparable to the fundamental and could be even higher with SHE 1.

Fig. 3.2 expands the results in the Table 3.3 by providing location of each harmonic in each respective regime and each tile shows harmonics at each load. Could be seen that modulation regimes are working as expected. Asynchronous PWM has harmonics to the side of 820 Hz, however they drift in harmonic order depending on slip. But synchronous PWM has 25^{th} and 29^{th} harmonics to the sides of 27^{th} and are independent of slip, as the frequency is synchronized with the synchronous speed.

SHE reliably eliminates all the lower order harmonics, while boosting following non eliminated one. From these results could be seen that each SHE regime operates as expected.

Fig. 3.3 outlines constituent power module losses in each regime and loading condition. As expected, in the high-power IGBT/Diode module, majority of the losses are produced by the switching losses, with the share of IGBT and diode conduction losses being 15-20% at the heaviest load. It once again shows that the focus here is the limits of switching losses by the means of limiting switching frequency in these devices.

Table 3.3 Summary of the Stator Current Indicators

Mode / Load	**THD, %**			**WTHD, %**			$\boldsymbol{I_1}$			$\boldsymbol{I_{2\ldots50}}$		
	(A)	(B)	(C)	(A)	(B)	(C)	(A)	(B)	(C)	(A)	(B)	(C)
(1)	8.37	8.13	2.42	1.45	3.16	0.65	54.2	144.5	275.1	4.5	11.7	6.7
(2)	14.54	8.35	3.99	2.39	2.59	0.87	54.0	144.8	274.7	7.9	12.1	11.0
(3)	49.82	19.18	9.69	2.23	2.36	0.75	53.9	144.9	274.8	26.8	27.8	26.6
(4)	42.72	16.07	7.65	1.99	2.32	0.71	53.7	145.0	274.5	23.0	23.3	21.0
(5)	47.73	20.23	10.76	2.79	1.76	1.81	53.8	122.9	227.0	25.7	24.9	24.4
(6)	53.43	16.69	7.82	4.35	1.82	0.78	34.0	109.4	229.3	18.2	18.3	17.9
(7)	201.81	53.15	24.67	35.37	9.34	4.50	22.7	85.8	185.7	45.8	45.6	45.8

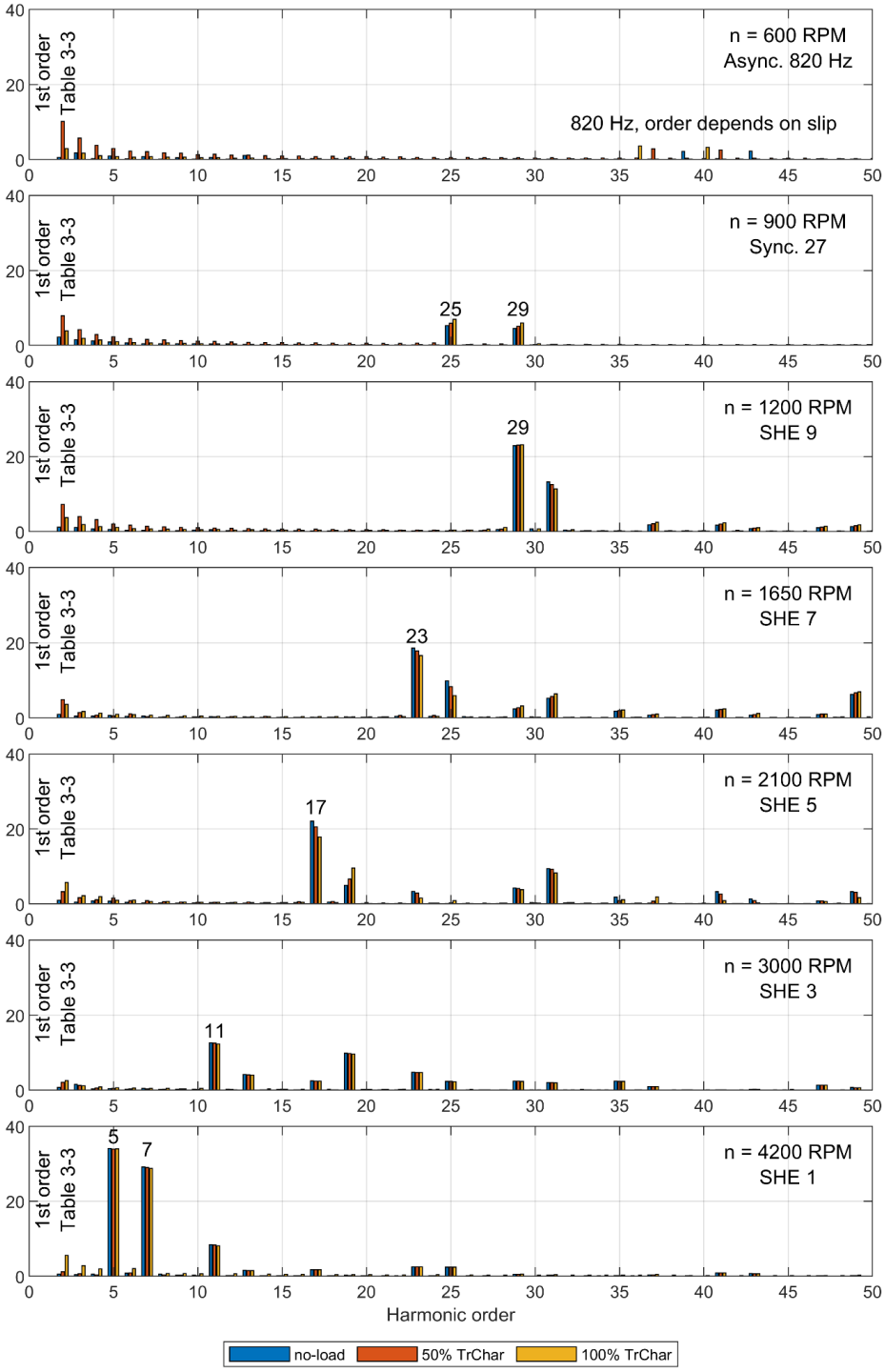

Fig. 3.2. FFT in each regime (excludes 1st harmonic).

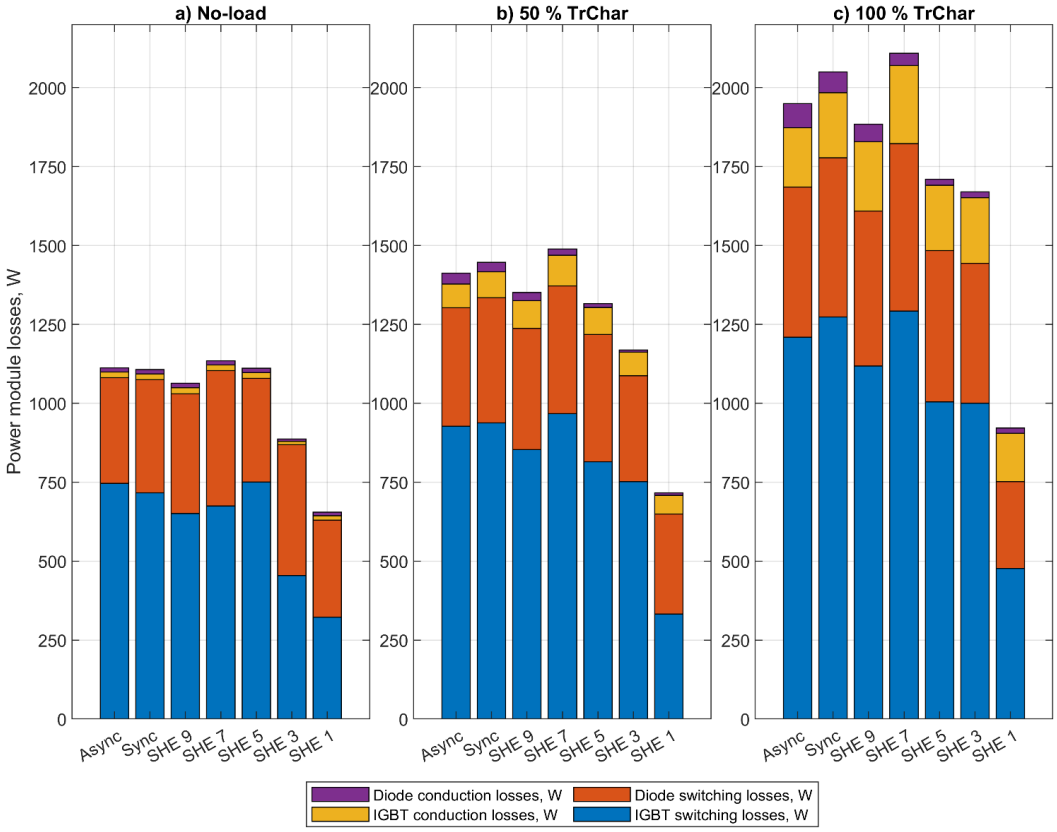

Fig. 3.3. Constituent losses of the power module.

Following that, based on the results several preliminary conclusions could be drawn. While THD with SHE PWM is substantially higher than one with synchronous PWM, WTHD is almost the same, because the harmonic order is shifted further from the fundamental harmonic and is less critical. It has lesser effect on the motor losses and could be more easily filtered. At the same time when transitioning from sync. 27 to SHE 9, switching frequency is lowered by 6.2–7.4 %, and total power losses are lowered by 4–8 % based on loading conditions.

3.1.2. Comparison of synchronous and SHE PWM

The following set of tests revolves around comparison of the synchronous PWM and SHE PWM performance in different conditions.

3.1.2.1. At the same switching frequency

The first test was carried out at several reference points with synchronous PWM and SHE in different configurations, where Table 3.4 outlines the reference points used for the test. For this test

manual PWM mode transition regime was set, which allows for arbitrary pre-set combination of PWM modes with any setting to transition at any point in time.

Table 3.4 Overview of Reference Points

PWM mode	Reference speed, RPM	Switching frequency, Hz		
		No-load (A)	1500 Nm (B)	3000 Nm (C)
Synchronous 23 (1)	900	690	703	717
SHE 11 (2)				
Synchronous 19 (3)		570	581	592
SHE 9 (4)				
Synchronous 15 (5)		450	459	468
SHE 7 (6)				
Synchronous 23 (7)	1140	874	888	901
SHE 11 (8)				
Synchronous 19 (9)		722	733	744
SHE 9 (10)				
Synchronous 15 (11)		570	579	588
SHE 7 (12)				

Reference points at 900 and 1140 RPM are chosen as they lay on both sides of the hybrid PWM transition points between ‘Sync. 27’ and ‘SHE 7’, as these reference points approximately correspond to 30 and 38 Hz, depending on the slip. While 0, 1500 and 3000 Nm loads represent 0 %, 50 % and 100 % of the reference traction characteristic in this area.

At these speeds three PWM pairs are tested with equivalent switching to fundamental frequency ratios of 23, 19, and 15 for synchronous and SHE PWM respectively.

These points are more representative in the THD, WTHD, and losses department, and show comparative advantages and disadvantages of synchronous and SHE PWM. Summary of the stator current performance indicators are shown in Table 3.5, while power module losses are shown in Fig. 3.4. Green colour in WTHD outlines lower value across synchronous-SHE pairs for clearer visualisation. While thicker divider in the table separates each pair of reference points.

Table 3.5 Summary of the Stator Current Indicators

Mode / n-ref	**THD, %**			**WTHD, %**			I_1			$I_{2...50}$		
	(A)	(B)	(C)	(A)	(B)	(C)	(A)	(B)	(C)	(A)	(B)	(C)
(1)	39.84	15.60	9.74	2.36	1.67	2.12	54.1	145.0	273.9	21.6	22.6	26.7
(2)	52.63	20.47	12.14	2.21	1.76	2.10	54.0	145.0	273.9	28.4	29.7	33.2
(3)	48.07	18.73	11.31	2.38	1.76	2.16	54.1	145.0	273.9	26.0	27.1	31.0
(4)	58.41	22.38	12.93	3.20	1.75	2.11	54.2	145.0	274.0	31.6	32.4	35.4
(5)	63.28	24.45	14.23	3.09	1.83	2.18	54.0	145.0	273.9	34.2	35.4	39.0
(6)	73.21	27.70	15.53	3.50	2.01	2.22	54.0	145.0	274.0	39.5	40.2	42.6
(7)	36.84	14.30	8.81	2.16	1.54	1.89	54.1	145.0	274.2	19.9	20.7	24.2
(8)	49.00	18.71	11.00	2.53	1.52	1.97	54.0	145.0	274.1	26.5	27.1	30.2
(9)	44.45	17.13	10.23	2.36	1.55	1.94	54.1	145.0	274.1	24.1	24.8	28.0
(10)	51.59	19.50	11.10	2.26	1.68	1.92	54.0	145.1	274.1	27.8	28.3	30.4
(11)	59.05	22.55	12.97	3.18	1.73	1.96	54.0	145.1	274.1	31.9	32.7	35.5
(12)	62.71	23.46	13.03	3.00	1.72	1.94	54.0	145.0	274.1	33.9	34.0	35.7

Could be seen that in THD synchronous PWM is favourable because amplitudes of created harmonics are lower. However, WTHD is either close with SHE or lower in many cases especially at higher loads and/or higher speeds.

That is the case with WTHD because synchronous 23 has main prominent harmonics at 21st and 25th orders, synchronous 19 at 17th and 21st, synchronous 15 at 13th and at 17th, while SHE 11 eliminates up to 34th and has boosted harmonics at the 35th and 37th orders, SHE 9 and SHE 7 have boosted at 29th/31st and 23rd/25th respectively (summarized in Table 1.1), which are significantly further than with synchronous PWM.

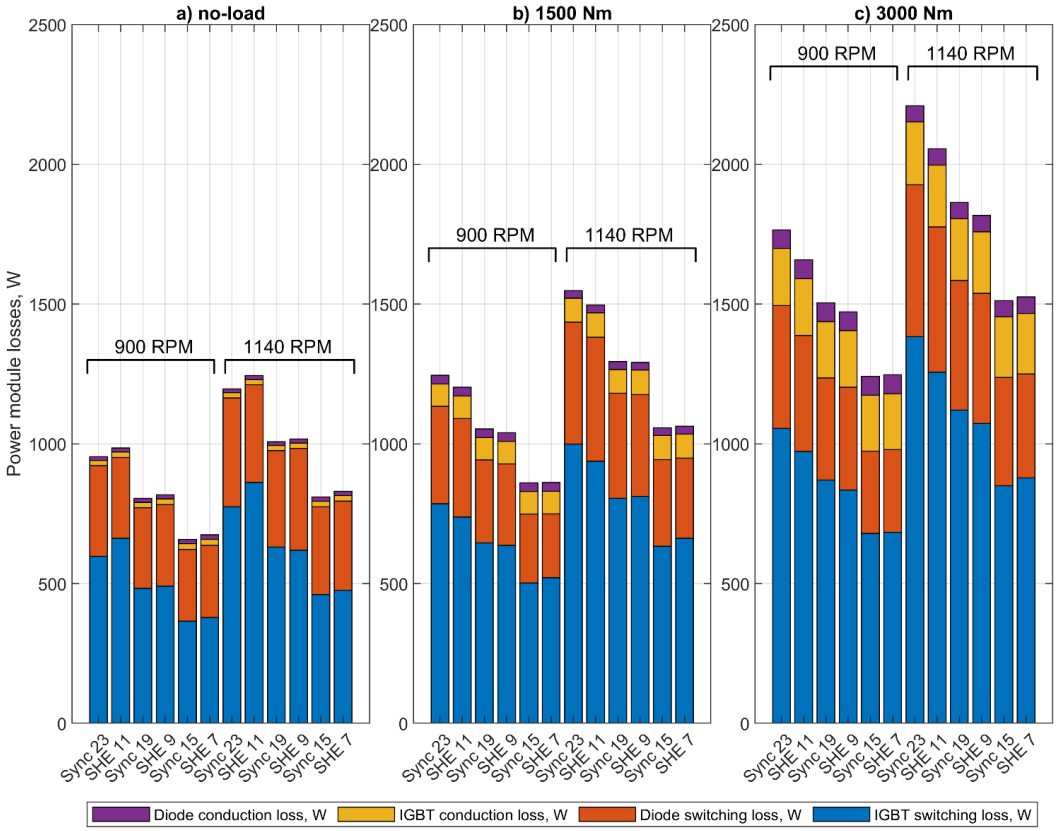

Fig. 3.4. Constituent losses of the power module.

The assessment of losses presents a complex and multifaceted challenge. At no-load or under low loading conditions, synchronous PWM provides lower power module losses (0.9 %–4 %) compared to the respective SHE. However, at 1500 Nm, the losses are either almost equal or SHE shows up to 3.4 % lower losses. At 3000 Nm, the losses are either nearly equal or SHE exhibits up to 7 % lower losses compared to synchronous PWM, depending on the m_f ratio.

It can be concluded that the lower the ratio of switching to fundamental frequency, the better the SHE performs. Additionally, at higher loads, SHE is more favourable due to both lower losses and lower WTHD. Further work on an adaptive transition scheme could investigate the combination of not only frequency-dependent but also load-dependent transition schemes, aiming to minimize both WTHD and losses.

3.1.2.2. At traction characteristic reference

This section covers comparison of operation with mode transition scheme utilizing SHE and synchronous PWM with the same switching frequency. Instead of SHE 9, 7, 5, 3, and 1 synchronous PWM was selected with switching to fundamental frequency ratio of 19, 15, 11, 7, and 3, such that switching frequency pattern stays consistent with original SHE PWM scheme.

To calculate THD and WTHD at each point FFT with at least 20 periods was required, thus the system needed to reach stable operation. Therefore, 4 seconds of stable operation were analysed at 50 speed reference points with a step of 100 RPM. From that stator current signals were analysed for harmonic content, THD, and WTHD.

Fig. 3.5 shows performance indicators of the two regimes. Blue line represents SHE sections, while red line represents synchronous PWM.

Operation with synchronous PWM with $m_f = 3$ was not stable and failed to reliably reach reference points, therefore results were excluded from the final graph.

The provided graph outlines several key indicators: output torque and switching frequency as indicators that systems operate with identical references. Stator current, power module losses, THD and WTHD to compare the performance of the systems.

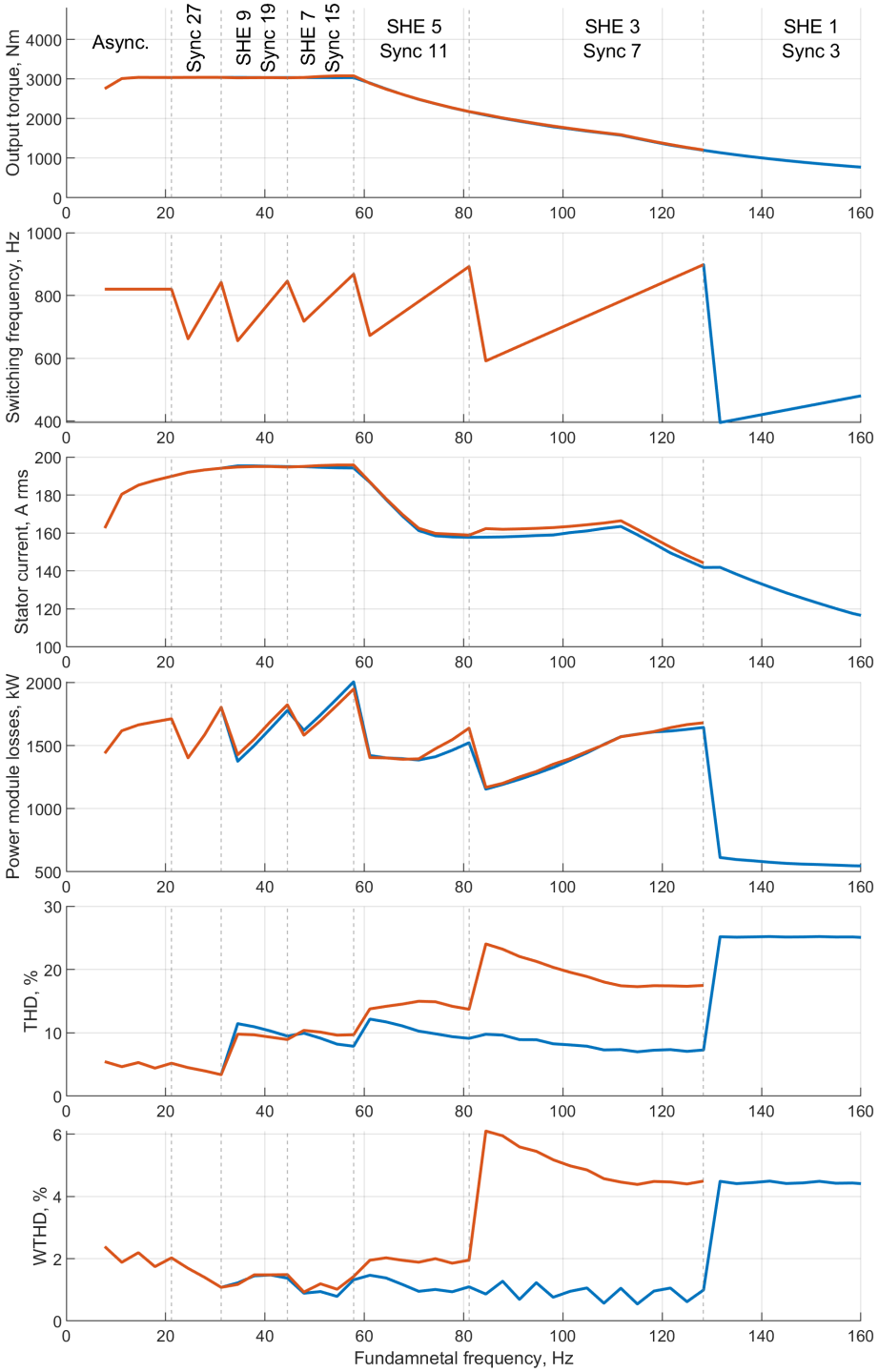

Fig. 3.5. Comparison of SHE and Synchronous PWM.

Could be seen that SHE 9/sync. 19 operate with very similar indicators and it is inconclusive which is more favourable. But could be said that if the system does not go below m_f ratio of 19, standard synchronous PWM could be employed.

However, starting from SHE 7/sync. 15 THD/WTHD starts to increase with each transition quite significantly. With SHE 5 and SHE 3 showing the best results in terms of current quality at very low m_f ratios.

Starting at SHE 5/sync. 11, differences in THD/WTHD become very significant even under loaded conditions, making operation with synchronous PWM ill-advised. As is commonly stated in the literature, the minimum acceptable ratio of switching frequency to fundamental harmonic is typically 10, and the reasons for this are evident. The most prominent harmonics of sync. 7 are the 5th and 9th, whereas for SHE 3, they are the 11th and 13th. At sync. 7, compared to SHE 3, the RMS current becomes on average 4.4 % larger due to significantly elevated harmonics, even at full load. At no-load conditions, the difference is even more pronounced.

In conclusion, power module losses are on average 1.5 % lower with SHE than with synchronous PWM across all differing regimes (SHE 3, 5, 7, and 9). At SHE 5 and SHE 3, THD/WTHD is substantially lower than with the same frequency of synchronous PWM.

3.1.3. Comparison of different SHE solutions

Selective harmonic elimination problem has multiple solutions depending on the number of notches per-quarter wave of the fundamental waveform. Number of unique solutions were calculated for SHE up to 13 and were outlined in Table 1.2 for 2-level inverter and in Table A.1 for 3-level inverter. This research focuses more on the control system and general implementation of the hybrid PWM approach into the system and testing of its stability. However, the test was conducted comparing different solutions for SHE 7 and SHE 9 utilizing each of the 4 unique solutions, as proof of actual numerical difference between solutions and idea for more in-depth analysis in further research.

Table 3.6 outlines the reference points used in the test. In the PWM mode shortened value in brackets is used for further marking for conciseness. Solution number corresponds to the values showed in Fig. 1.7 through 1.10.

Switching angle values are shown in the Fig. 1.7 and Fig. 1.8 for SHE 7, and in Fig. 1.9 and Fig. 1.10 for the SHE 9, depending on the reference modulation index produced as a result by the designed control system.

Table 3.6 Overview of Reference Points

<table>
<tr><th rowspan="2">PWM mode</th><th rowspan="2">Reference speed, RPM</th><th colspan="6">Switching frequency, Hz | Modulation index</th></tr>
<tr><th colspan="2">No-load (A)</th><th colspan="2">1500 Nm (B)</th><th colspan="2">3000 Nm (C)</th></tr>
<tr><td>SHE 9, Solution 1 (9–1)</td><td rowspan="8">900</td><td rowspan="4">570</td><td rowspan="8">0.43</td><td rowspan="4">585</td><td rowspan="8">0.465</td><td rowspan="4">599</td><td rowspan="8">0.512</td></tr>
<tr><td>SHE 9, Solution 2 (9–2)</td></tr>
<tr><td>SHE 9, Solution 3 (9–3)</td></tr>
<tr><td>SHE 9, Solution 4 (9–4)</td></tr>
<tr><td>SHE 7, Solution 1 (7–1)</td><td rowspan="4">450</td><td rowspan="4">462</td><td rowspan="4">473</td></tr>
<tr><td>SHE 7, Solution 2 (7–2)</td></tr>
<tr><td>SHE 7, Solution 3 (7–3)</td></tr>
<tr><td>SHE 7, Solution 4 (7–4)</td></tr>
</table>

Table 3.7 summarizes results outlining stator current performance indicators, while Fig. 3.6 represents power module constituent and total losses, in the same way as was done in previous tests. Table 3.7 has a red colour shading representing maximum respective value, and a light green colour representing minimum respective value across solutions.

Table 3.7 Summary of the Stator Current Indicators

Mode	**THD, %**			**WTHD, %**			I_1			$I_{2...50}$		
/ n-ref	(A)	(B)	(C)	(A)	(B)	(C)	(A)	(B)	(C)	(A)	(B)	(C)
(9–1)	59.72	23.62	12.45	2.34	2.70	0.58	53.9	144.5	272.7	32.2	34.1	33.9
(9–2)	58.61	23.05	12.06	3.38	2.72	0.64	54.0	144.5	272.7	31.6	33.3	32.9
(9–3)	63.42	25.19	13.53	2.71	2.69	0.63	53.9	144.5	272.7	34.2	36.4	36.9
(9–4)	61.83	24.49	13.04	2.89	2.74	0.64	53.9	144.5	272.6	33.3	35.4	35.5
(7–1)	73.27	28.27	14.75	3.64	2.93	0.72	53.9	144.5	272.6	39.5	40.8	40.2
(7–2)	75.59	29.33	15.56	3.31	2.81	0.74	53.9	144.5	272.7	40.7	42.4	42.4
(7–3)	83.46	32.48	17.50	3.89	2.90	0.83	53.9	144.5	272.6	45.0	46.9	47.7
(7–4)	79.64	30.90	16.50	4.19	2.91	0.90	54.0	144.5	272.6	43.0	44.7	45.0

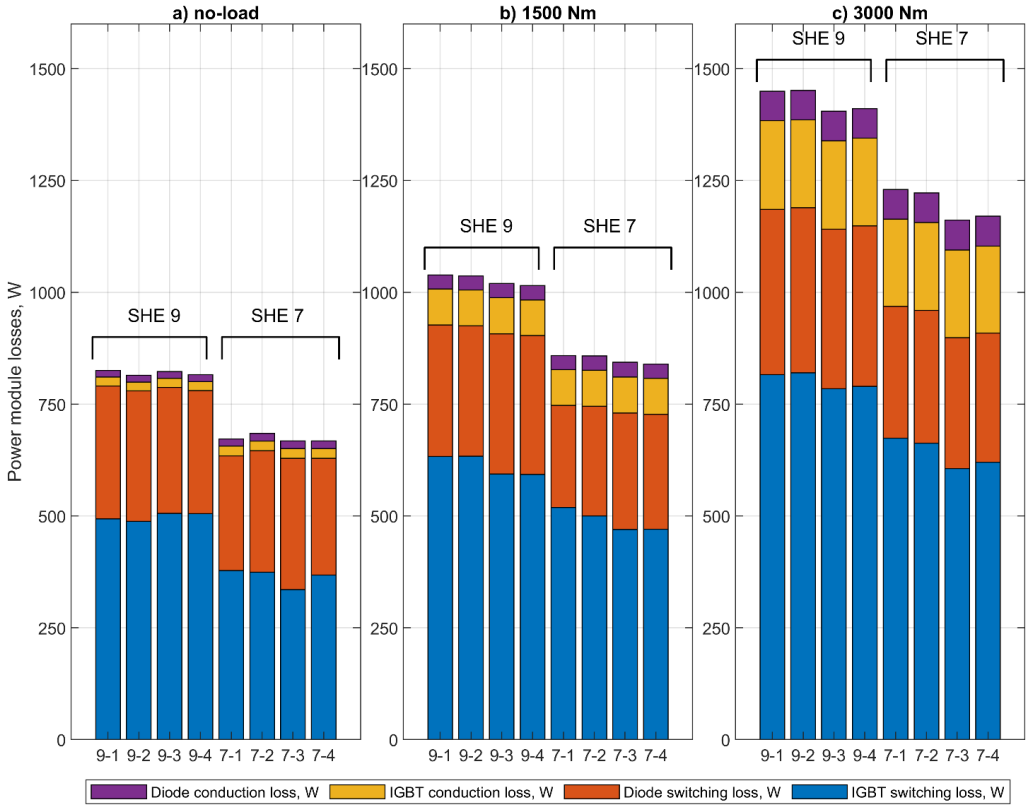

Fig. 3.6. Constituent losses of the power module.

From the presented data could be seen that there is no difference regarding the fundamental current component I_1 as it stays constant across the SHE types and its solutions, while different only depending on the load value. That is expected, as the task of the control system and the fundamental current hybrid observer is to keep the stator current's fundamental harmonic at predefined level.

However, another story entirely when harmonic content and total losses are considered. Analysing WTHD and stator current harmonic component, could be seen that there is a measurable difference between solutions. In WTHD difference in SHE 9 is up to 45 %, and up to 27 % in SHE 7, with more prominent difference in no-load conditions, while at full load difference is up to 20 %. And when discussing $I_{2\ldots50}$ differences between the worst- and best-case results can reach up to 19 %, while values remain relatively constant regardless of the load. Consequently, THD and WTHD decrease with increasing load.

Regarding power module, and consequently power converter losses, differences between solutions are measurable. Under no-load conditions, the maximum difference in losses is 2.5 %, while at full load, the maximum difference reaches 6 %. The most significant impact is due to the difference

in IGBT switching loss, because switching occurs at different phases of the current, and switching energy is mainly dependent on the instantaneous value of the current at the switching point.

In conclusion, there is a measurable difference between SHE solutions in both WTHD and power module losses. For the most efficient operation with the best achievable stator current quality, an optimization process should be developed at a later stage of development. However, the task of optimizing losses and WTHD falls outside the scope of the current research, and the preliminary results are presented as a basis for future research possibilities.

3.2. Control system performance without EMU

The next set of modelling tests outlines the control system performance without EMU. This way it is possible to test the system's stability with higher rates of acceleration, and with application of static load.

3.2.1. Flux response

The first test is induction motor magnetization, in other words performance of the flux loop. Test is conducted by applying reference flux of $\psi_{nom} = 2.75\ Vs$ in a step manner and with the ramp of $2 \cdot \psi_{nom} = 2 \cdot 2.75\ Vs/second$.

Test results are summarized in Fig. 3.7 with the left tile showing motor flux with calculated and modelled responses, while on the right is change in magnetizing current (d-axis current).

Could be seen that the design of the PI controllers was accurate as the modelled response almost perfectly matches the theoretically calculated values. Magnetizing current in a step response does not exceed the current limit, however, to decrease stress on an actual system ramp is commonly used. Even with a ramp that has a rise time of 0.5 seconds peak value of needed current is reduced 3x times, without much effect on a system performance. As the motor magnetization in real-world deployments does not happen that often or does not need to be very fast. While in the field-weakening mode change in speed is rather slow which does not cause rapid change in flux reference.

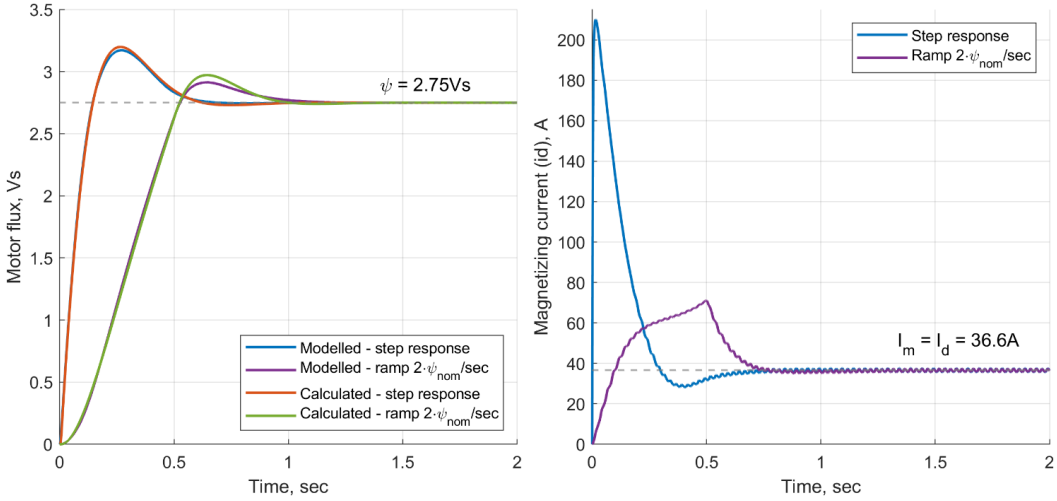

Fig. 3.7. Flux response: modelled and calculated.

3.2.2. Speed response

The next step of test is the response of system to the change in reference speed. Two sets of tests were carried out:

1. Acceleration and deceleration 0–4780 (n max)–0 RPM with only limiter being traction characteristic. Results are shown in Fig. 3.8.
2. Acceleration and deceleration 0–4780 (n max)–0 RPM with 500 RPM/s^2 rate limiter. Results are shown in Fig. 3.9.

Each of the figures shows the same set of plots:

- Left upper: motor speed, RPM
- Right upper: output torque, Nm (blue), output power, kW (red)
- Left lower: 1st RMS harmonic of the stator voltage, V (blue), total RMS voltage (red)
- Right lower: RMS stator current, A (blue), motor flux, Vs (estimated by the hybrid observer) (red)

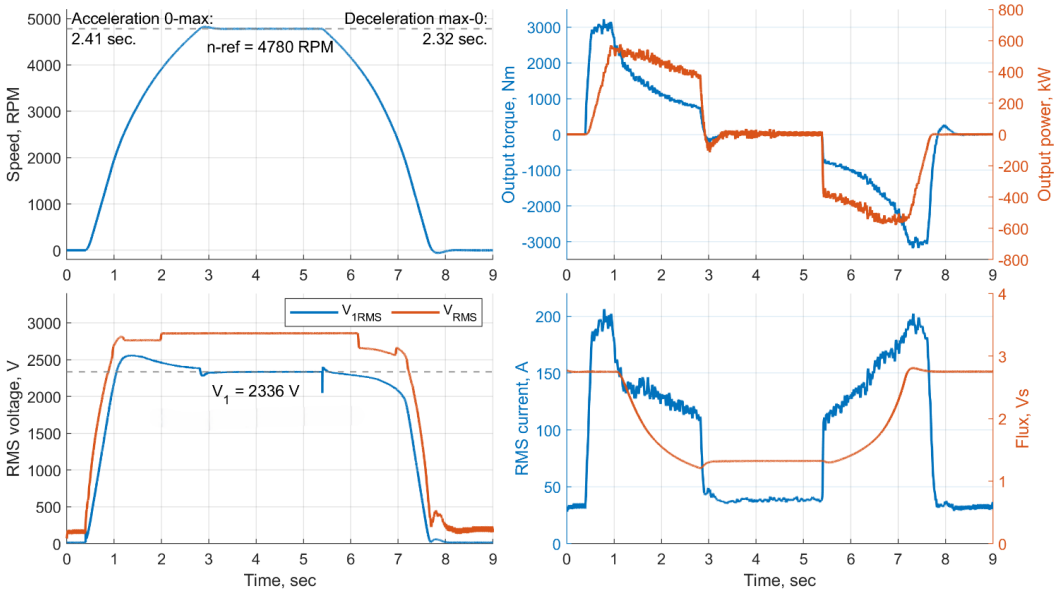

Fig. 3.8. Motor acceleration and deceleration at traction characteristic.

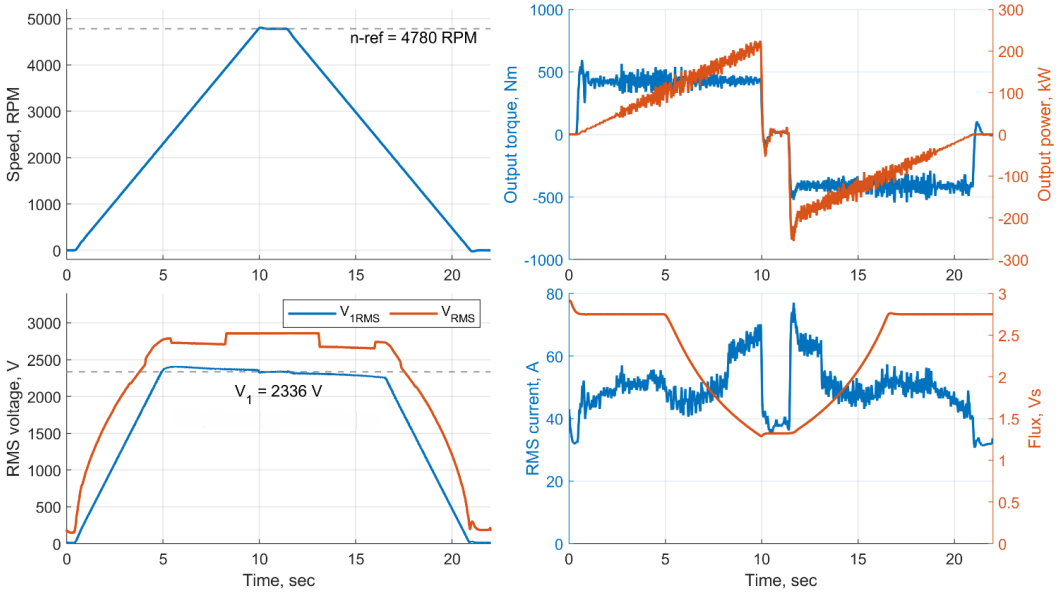

Fig. 3.9. Motor acceleration and deceleration at 500 RPM/s^2 ramp.

The test results performance indicators are summarized in the table below. It can be seen that even with the step response, the system operates within the desirable performance range. Both the control system and the fundamental current hybrid observer exhibit a much quicker response. As discussed in chapter 2.2.3, the maximum EMU acceleration is 0.95 m/s², which corresponds to 127

RPM/s². Thus, the 500 RPM/s² rate limiter is four times quicker than the maximum train acceleration, providing more than enough capability for testing the control system dynamics.

Table 3.8 Summary of Performance Indicators

	TrChar limiter	500 RPM/s^2 rate limiter
Speed overshoot, acceleration	43.4 RPM / 0.9 % overshoot	23.7 RPM / 0.5 % overshoot
Speed overshoot, deceleration	–57.2 RPM	–25.4 RPM
Feedback-based voltage limiter	227 Vrms / 9.7 % overshoot	72.5 Vrms / 3.1 % overshoot
Acceleration time	2.41 seconds	9.56 seconds
Deceleration time	2.32 seconds	9.56 seconds

3.2.3. Transitions between PWM modes

This section outlines transitions between PWM modes. Current waveforms are taken from the test 1. in chapter 3.2.2.

Select number of transitions both in acceleration and deceleration are shown in Fig. 3.10. Transitions are selected as to highlight waveform shape conformity between different modulators (synchronous and SHE), and between different SHE types. Could be seen that all transitions happen smoothly and in-phase without any noticeable spikes. The dotted line highlights the transition point at each subplot. While the time values at x-axis correspond to the time in Fig. 3.8.

Could be concluded that the modulation transitions happen smoothly even with the highest rate of acceleration achievable by the motor without the vehicle. Meaning that at slower rates transitions will not have any issues.

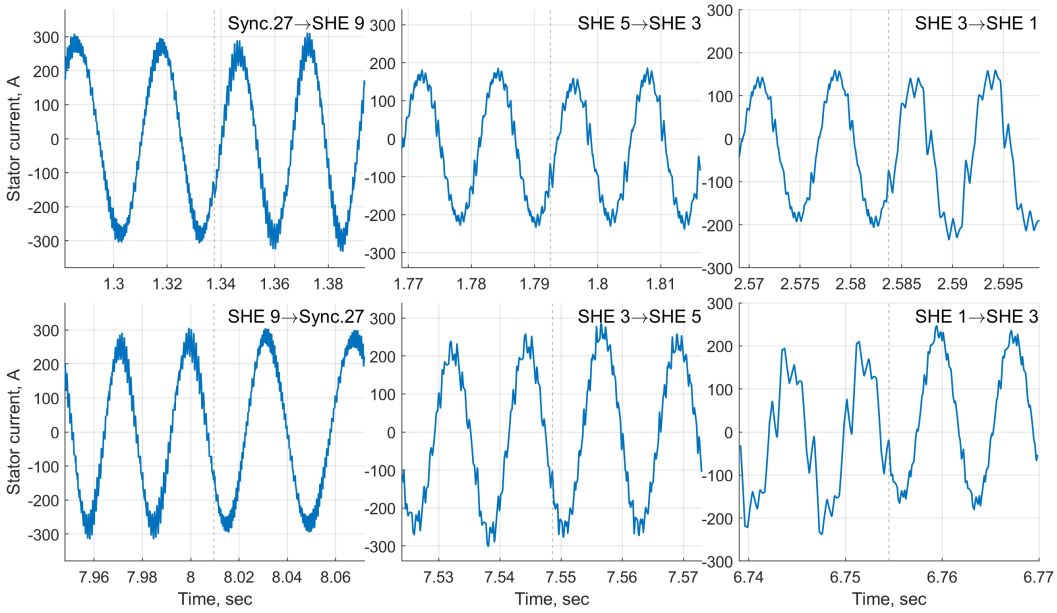

Fig. 3.10. Transitions between modulation regimes.

3.2.4. Hybrid observer operation

This section outlines the operation of the hybrid observer at transition points, and at the harshest regimes. Hybrid observe operation at transition points are shown in Fig. 3.11.

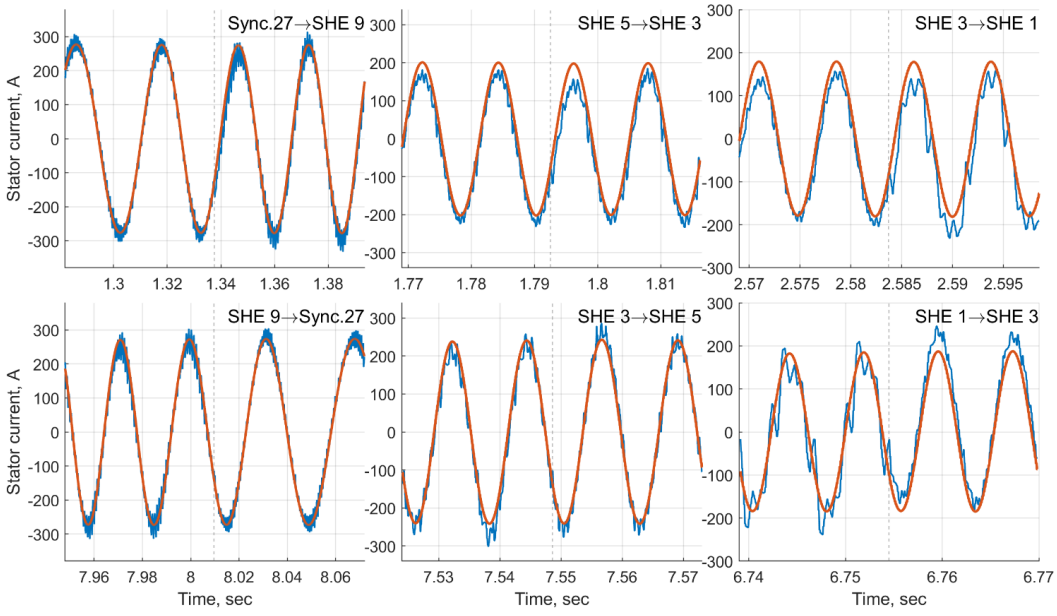

Fig. 3.11. Hybrid observer operation in transition regimes.

Fig. 3.11 is almost identical to the Fig. 3.10 with the overlay of the observer fundamental current output. The test data and time stamp values are as in Fig. 3.8. Could be seen that the tracking is consistent and accurate even at maximum acceleration rate. While at lower dynamics tracking is even better.

However, the harshest operation for the hybrid observer is the SHE 3 and SHE 1 at no-load conditions. As was described in chapter 3.1, absolute values of current harmonics do not change significantly with respect to applied load. Meaning that at no-load current harmonics with relation to fundamental are the highest. Especially with SHE 1.

Results of the hybrid observer fundamental current output with SHE 3 and SHE 1 at no-load are shown in Fig. 3.12. Could be seen that even with such low switching frequency hybrid observer is able to track the fundamental waveform's phase and amplitude.

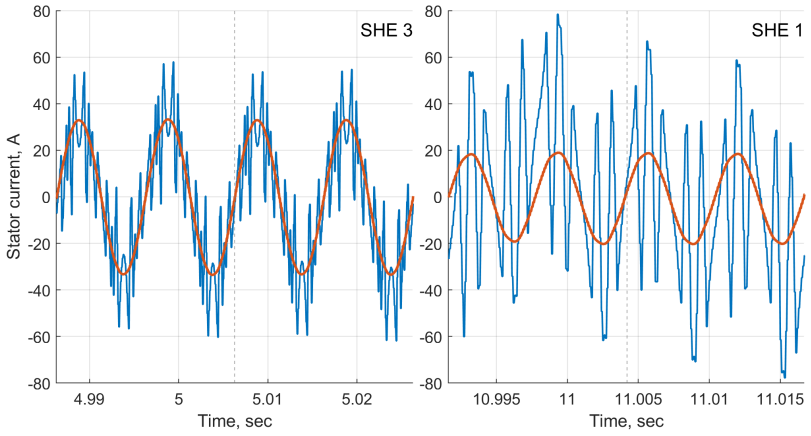

Fig. 3.12. Hybrid observer operation at no-load with SHE 3 and SHE 1.

However, could be concluded that SHE 1 operation is extremely noisy, with harmonics exceeding the fundamental, thus the operation at no-load if possible is not advisable. Requiring adaptive hybrid PWM transition scheme.

3.2.5. Reaction to load

The last test is reaction of the system to the disturbance insertion, in this case loading of the motor with step torque at specific speed.

Three speed reference points with safety margin were considered for this test:

- 0 RPM, 900 Nm, asynchronous PWM $f_{sw} = 820\ Hz$
- 2140 RPM, 2184 Nm, SHE 5
- 4780 RPM, 673 Nm, SHE 1

A value lower than the traction characteristic limit at the corresponding speed is selected to provide a safety margin for the controller to react.

Results of the test are shown in Fig. 3.13 with the numeric summary in Table 3.9. Figure consists of three columns depicting each test, and three rows each depicting rotor speed in RPM, output torque in Nm, and RMS voltage of the fundamental harmonic respectively.

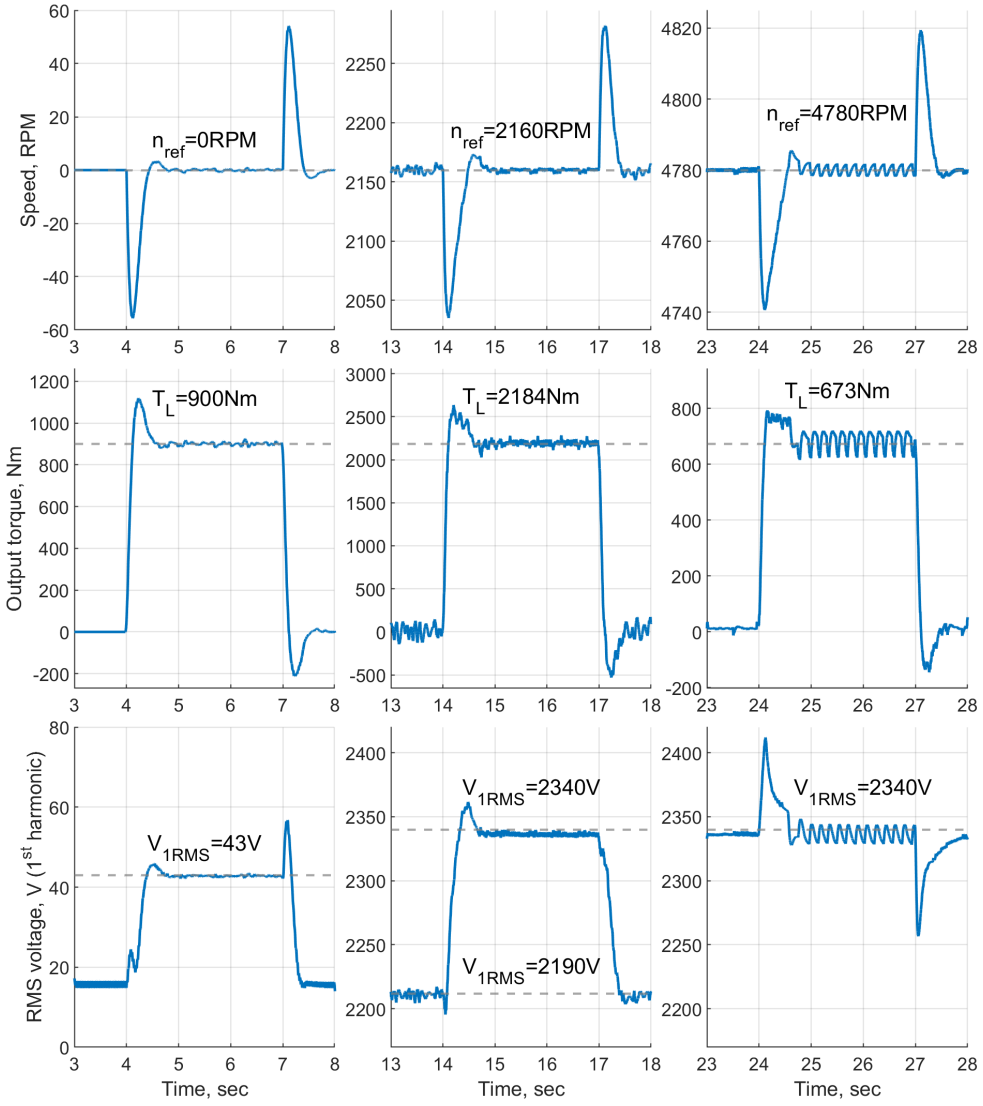

Fig. 3.13. Application of torque.

Table 3.9 shows the voltage at no-load and at load, maximum speed and minimum speed during load application and load removal.

The second reference point was selected in such a way that at no-load RMS voltage is below limit, while at full load reaches the limit and goes into the field-weakening without change in speed.

Table 3.9 Summary of the Performance Indicators

	Reference speed	0 RPM	2160 RPM	4780 RPM
	Reference torque	900 Nm	2184 Nm	673 Nm
	Voltage at no-load	16 V	2190 V	2340 V
	Voltage at load	43 V	2340 V	2340 V
Load application	Max. speed / Δn	3.1 / 3.1	2173.2 / 13.2	4785.5 / 5.5
	Min. speed / Δn	–55.6 / –55.6	2035.1 / –124.9	4740.6 / –39.4
Load removal	Max. speed / Δn	54.1 / 54.1	2282.0 / 122	4819.4 / 39.4
	Min. speed / Δn	–3.1 / –3.1	2151.4 / –8.6	4777.6 / –2.4

From the results, it can be seen that the magnitude of the absolute error changes is based on the magnitude of the applied torque. In conclusion, it can be stated that the control system operates properly at defined speed reference points when applying external disturbance in a step manner.

3.3. Control system performance with EMU

The next test is the verification of the operation of the developed system with an EMU model. The test consists of 2 reference points:

- at 2 seconds, the speed reference is set to 120 km/h;
- at 80 seconds, the speed reference is set to 0 km/h.

This test checks how the system performs with the hybrid PWM and fundamental hybrid observer in maximum effort acceleration till maximum operating speed and then deceleration till the full stop. During both acceleration and deceleration, the system follows the pre-established transition pattern. Test results are summarized in two graphs shown in Fig. 3.14 and Fig. 3.15.

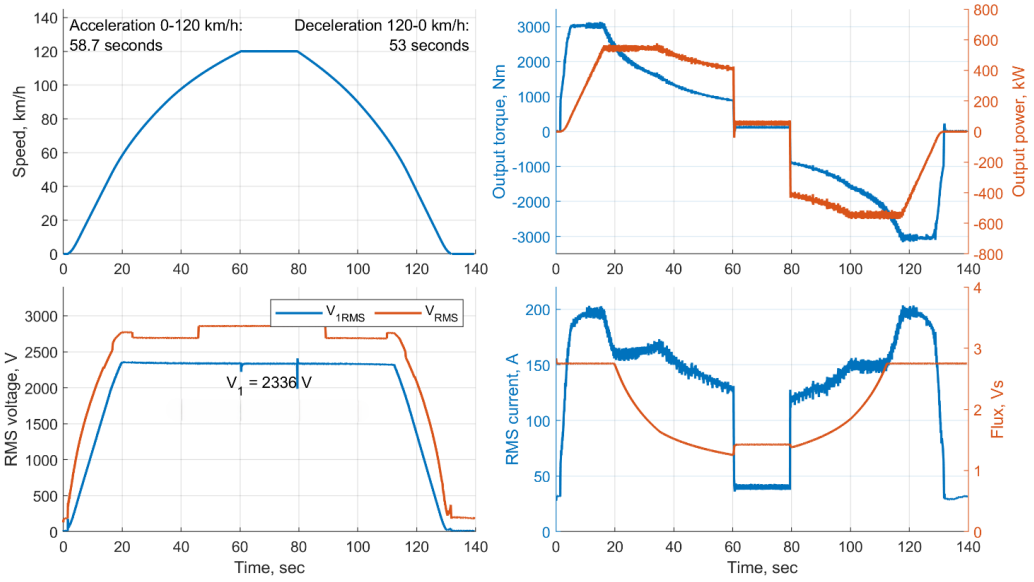

Fig. 3.14. EMU acceleration-deceleration. main performance indicators.

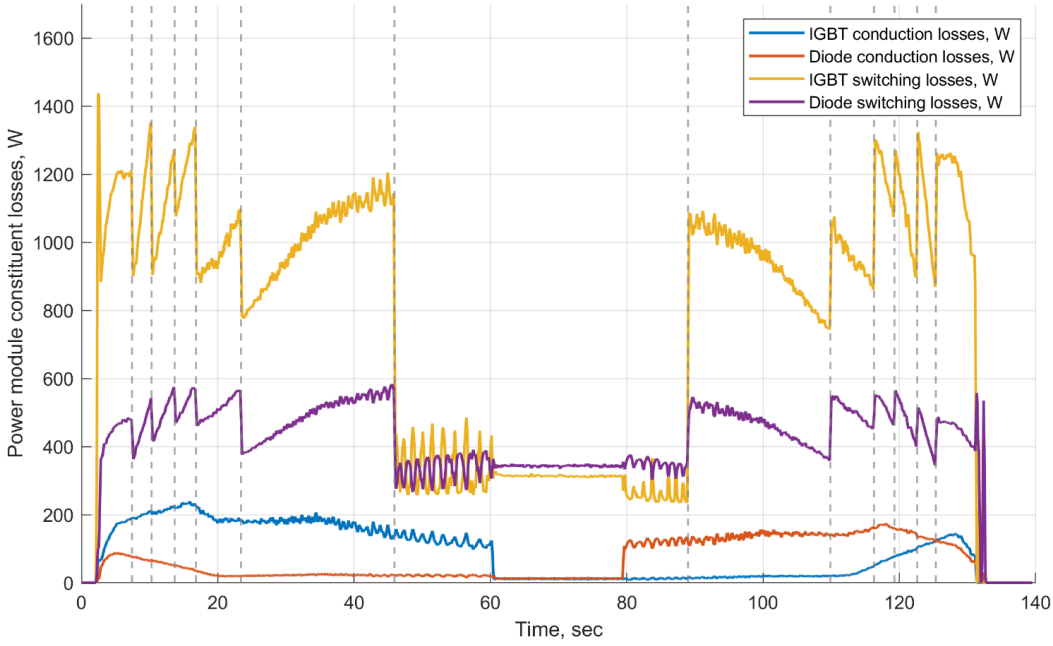

Fig. 3.15 Distribution of power module constituent losses.

From the Fig. 3.14, it can be seen that the train takes 58.7 seconds to reach the maximum speed, and 53 seconds to reach the full stop. Time to accelerate is almost identical to the theoretically

calculated one of 59.4 seconds. During acceleration and deceleration there is almost no-overshoot, system reaches 120.06 km/h at peak, and when reaching 0 km/h reaches –0.05 km/h.

The bottom left section of the graph presents the RMS voltage of the system. The red line represents the actual RMS stator line voltage including all harmonics, while the blue line represents the fundamental component of the RMS stator line voltage. The fundamental component is limited to the 2340VRMS voltage of the designed traction motor.

Upper right graphs clearly present output torque and power and outlines the constant torque, constant power, and $1/v^2$ operation regions.

The bottom right graphs represent stator RMS current, and system flux. From that start of the field-wakening regime is visible.

It can be noted that the control system reliably reaches provided speed reference and has an almost critically damped response with virtually no overshoot. The same could be said for the voltage. Before reaching the pre-defined fundamental RMS voltage limit, the system adheres to the V/f criterion, and after that strictly follows the voltage limit without deviating from it.

Fig. 3.15 represents the constituent losses of the power module. All the transition points are clearly visible both in the rapid change of losses and by the markings with the dotted line. The hybrid PWM approach reliably limits losses in the power module. However, when reaching the speed reference EMU goes into the regime of maintaining speed, which requires only a little tractive effort to combat the effects of train rolling resistance. At that point, the power module losses drop significantly, which opens a possibility for further optimization of the switching pattern, depending not only on frequency but also on load. That could be an area of further research.

4. Experimental Validation of the Developed Control System

Simulation is crucial during the development phase to address and resolve most issues and problems. Once the system is stable in the model, validation on the actual setup follows. However, when working with large and expensive electric drives, testing is conducted in steps, starting with a downscaled laboratory setup.

This research validates the developed system on a small, downscaled laboratory setup with adapted system limits and parameters. This chapter describes the laboratory setup and the necessary steps for transitioning from the parameters and limitations of the control system with EMU to the laboratory deployment. It is followed by a set of validation tests and an analysis of the results. The system undergoes the same set of tests as described in chapter 3, adapted to the downscaled laboratory setup.

4.1. Description of the laboratory setup

Testing of the developed traction motor control system intended for the railway application is done on a downscaled laboratory setup. Tests are made in all operational regimes to determine stability and capabilities of the system. This subchapter describes an overview of the setup with detailed description of select parts of the stand.

4.1.1. Laboratory setup

The developed control system is tested on a laboratory setup with a 2-level inverter, photo of which is shown in Fig. 4.1 and schematic diagram of the setup is shown in Fig. 4.2, followed by the description of each constituent part. Numbers in the description correspond to numbers on Fig. 4.1.

Experimental verification was conducted at the premises of Riga Technical University, with the list of laboratory equipment provided in Appendix C.

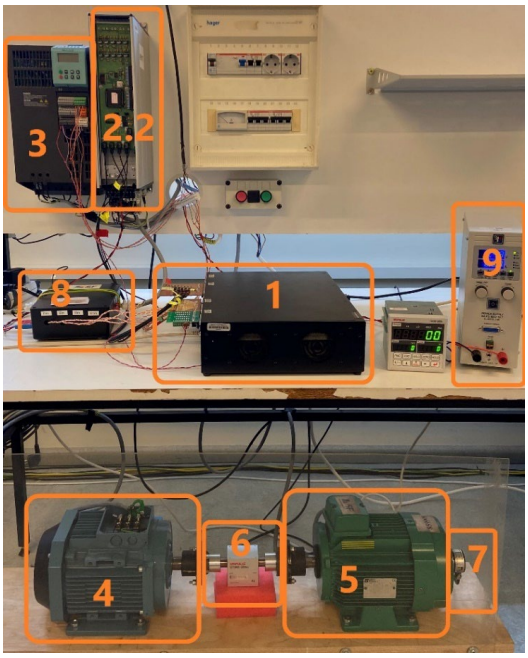

Fig. 4.1. Overview of the laboratory setup.

Where:

1. Real-time simulator: Opal-RT OP4510 (acts as a control board). More in-depth description of the capabilities of real-time simulator and of its functionality in this setup are described in chapter 4.1.2.
2. The industrial 2-level frequency inverter from Danfoss The industrial inverter from Danfoss does not use the standard control board. Instead, it has a custom interface board allowing direct access to the control signals of the inverter: signal for each phase, inverter enable, and braking resistor signals while keeping overcurrent, overvoltage and overtemperature protection. In addition to that, the interface board includes dead-time management preventing shoot-through of the transistors. The interface board accepts optical control signals.

   Pre-set limits on the inverter: instantaneous current trip limit – 15 A, DC-link voltage trip limit – 750 VDC, dead-time – 1 microsecond.
3. Inverter for a load motor – SIEMENS AFE (Active Front-End) CU240S

   Pre-set limits on the inverter: maximum fundamental frequency – 120 Hz, maximum output torque – 15 Nm.
4. Test induction motor: ABB M2AA100LB-4 3GAA102002-ADE. Developed control system requires equivalent circuit of the motor to operate properly, which is tested for further.

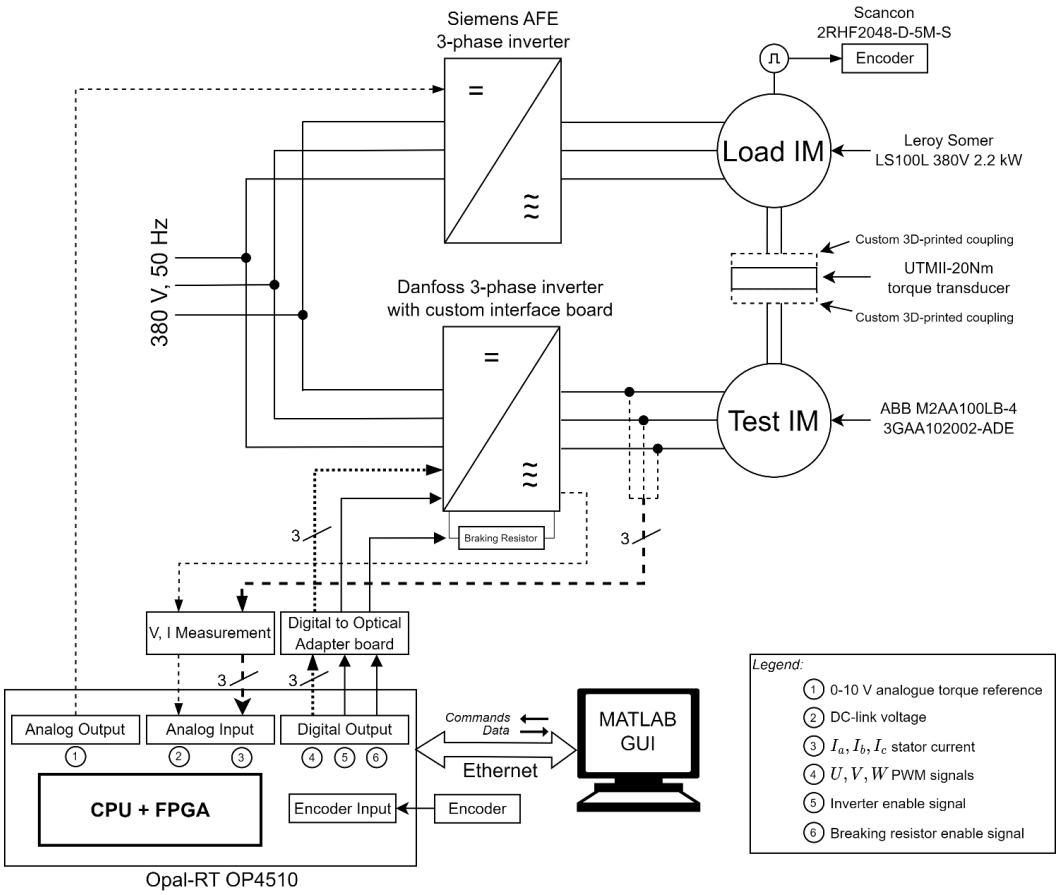

Fig. 4.2. Schematic diagram of the laboratory setup.

5. Load induction motor: Leroy Somer LS100L 380V 2.2kW. It is driven by the SIEMENS AFE inverter, equipped with a bidirectional rectifier bridge. This inverter is with a stock control system and is set in torque vector control mode. The stock control system is automatically tuned to the Leroy Somer motor based on the internal program of the Simens AFE inverter. The reference torque value is set from the OP4510 simulator.
6. Rotating torque meter: UTMII-20Nm. It measures output torque on the motor shaft and interconnects motors with backlash-free couplings.
7. Encoder: Scancon 2RHF2048-D-5M-S
8. Current and voltage measurements box. Consists of LEM LA 55-P (3x) and LEM LV 25-600. Current sensors are installed on a custom PCB, which in turn, with a voltage sensor board, are assembled into a case.
9. DC-voltage power supply with 0–32 V range for supplying supplementary electronics.

4.1.2. OP4510 real-time simulator

Real-time simulator could either be used as a part of the hardware-in-the-loop (HIL) setup, or as a control board for the actual setup running the developed control system in real-time, as it is commonly used during development phase [101]. In the case of this application OP4510 simulator is used and acts as a control board for the laboratory setup.

This section describes main idea behind real-time simulation, description of the used simulator, and its use in the current laboratory setup.

4.1.2.1. Basis of the Real-Time Simulation

Computer simulation is based on the mathematical representation of the system at hand. To solve mathematical functions and equations at a given time-step, each variable or system state is solved successively as a function of variables and states at the end of the preceding time-step. Real-time systems are simulated in fixed step discrete domain due to time constraints [102].

During a discrete-time simulation, the amount of real time required to compute all equations and functions representing a system during a given time-step may be shorter or longer than the duration of the simulation timestep. Fig. 4.3(a) and Fig. 4.3(b) represent these two possibilities. These two situations are referred to as offline simulation. In both cases, the moment at which a result becomes available is irrelevant. Typically, when performing offline simulation, the objective is to obtain results as fast as possible. The system solving speed depends on available computation power and the system's mathematical model complexity.

Conversely, during real-time simulation, the accuracy of computations not only depends upon precise dynamic representation of the system, but also on the length of time used to produce results. Fig. 4.3(c) illustrates the chronological principle of real-time simulation. For a real-time simulation to be valid, the real-time simulator used must accurately produce the internal variables and outputs of the simulation within the same length of time that its physical counterpart would. After the calculation the simulator waits until the clock ticks to the next timestep. However, if simulator operations are not all achieved within the required fixed time-step, the real-time simulation is considered erroneous. This is commonly known as an "overrun" [102].

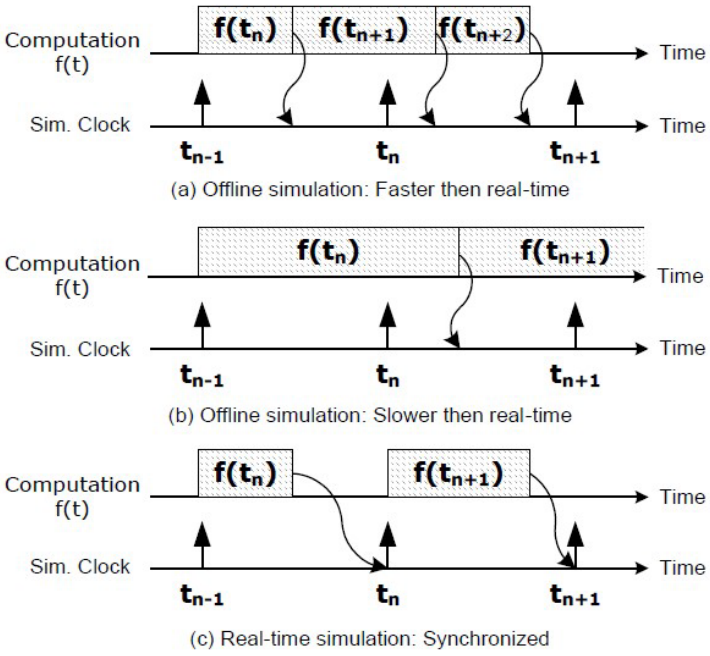

Fig. 4.3. Simulation techniques [102].

Based on these basic definitions, it can be concluded that a real-time simulator is performing as expected if the equations and states of the simulated system are solved accurately, with an acceptable resemblance to its physical counterpart, without the occurrence of overruns.

Real-time simulated systems come in various forms:

- Hardware-in-the-loop: controller design and control system are tested as a DUT, while plant is simulated [102], [103], [104].
- Rapid control prototyping: plant controller is implemented using a real-time simulator and is connected to a physical plant [102].
- Software-in-the-loop: controller design and control system are modelled and simulated in real-time, as well as plant is simulated in real-time too [102].
- Power hardware-in-the-loop: it is a variation of HIL with the addition of some components of the plant. Such as inverter is real, while vehicle is simulated (i.e. [105]).

There are some other variations, but the above-mentioned are the most common ones.

Modelling and verification in a laboratory in real-time are part of the commonly used design approach called Model-Based Design. Model-based design is a methodology based on a workflow known as the “V” diagram, example of which is shown in Fig. 4.4.

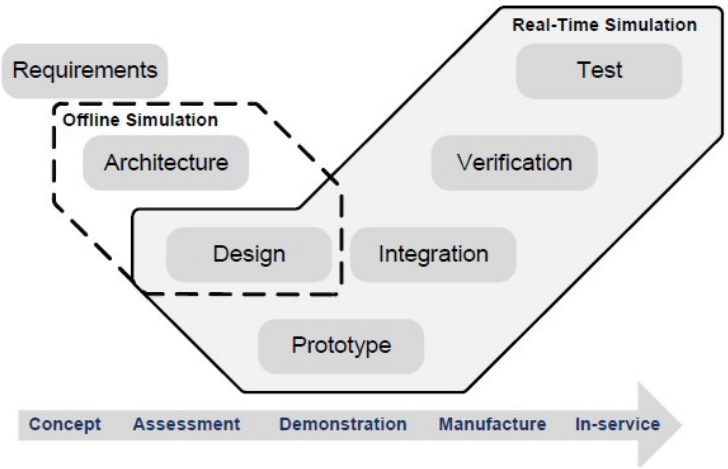

Fig. 4.4. Model-based design workflow.

Model-based design provides many advantages [102]:

- Design issues can be discovered earlier in the process, enabling required trade-offs to be determined and applied, thereby reducing development costs.
- Development cycle duration is reduced due to parallelization in the workflow.
- Testing costs can be reduced in the medium- to long-term since HIL test setups often cost less than physical setups and the real-time simulator employed can be typically used for multiple applications and projects.
- Testing results are more repeatable since real-time simulator dynamics do not change through time the way physical systems do.
- Can replace risky or expensive tests using physical test benches.

4.1.2.2. Description of the Real-Time Simulator

In the laboratory OP4510 real-time simulator by OPAL-RT is used as a control board. OP4510 is a real-time simulation platform designed for power electronics and power systems applications. It is equipped with FPGA and a high-performance CPU, which allows for high-speed, deterministic simulations. The system also includes a variety of I/O interfaces, including analogue and digital inputs and outputs, as well as an expansion slot for additional I/O modules.

The system in use has standard configuration [106]:

- FPGA: Kintex-7 FPGA, 325T, 326,080 logic cells, 840 DSP slice (Multiplier- adder)
- Computer: Full simulator equipped with Intel Xeon E3 v5 CPU (4 core, 8MB cache, 2.1 or 3.5GHz), 16G B RAM, 128 GB SSD

– I/O modules: 2x16 digital input modules, 2x16 digital output modules, 1x16 analogue input module, and 1x16 analogue output module
– RS422 connector, in this modification 2x differential encoder inputs and outputs module
– Connection to the host PC over Ethernet

Below in the Fig. 4.5 is the system architecture of the OP4510, with main components described in above paragraph.

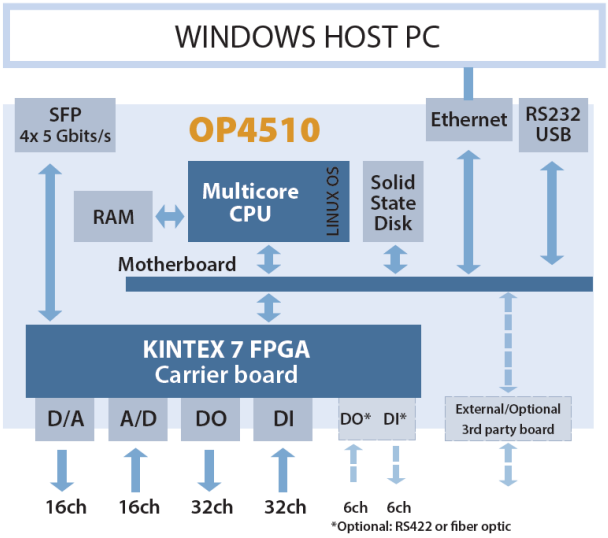

Fig. 4.5. OP4510 system architecture in standard configuration [106].

Specific use of the real-time simulator in this laboratory setup is described in the following part of the chapter.

4.1.2.3. Use as a control board in the setup

OPAL-RT OP4510 is used as a control board for the main motor and for setting reference values of torque for the Siemens AFE which drives load motor. This setup is used for the initial stage of development as with Simulink and custom libraries from OPAL-RT control system deployment and testing takes considerably less time, compared to a custom-made control board.

Different signals act as inputs and outputs to and from OP4510. Below are the signals classified by their type:

1. Digital outputs produce five signals: three PWM signals of each inverter IGBT leg, enable and breaking resistor activation signals, which are fed to the Danfoss inverter. Signals go through a custom intermediary board. It converts the electrical digital outputs of the OP4510 to optical signals, which are sent to the input of the Danfoss inverter.

2. Analogue output is a single signal which is fed to the analogue input of the Siemens converter which is set up to control output torque reference from 0 Nm to 15 Nm at 0 V and 10 V respectively.
3. Analogue inputs are three current and one voltage measurement signals with a shunt resistor and a torque signal from a torque meter with a low pass filter based on the torque meter producer documentation.
4. The signal from the rotary encoder is read by an OPAL-RT RS422 differential encoder expansion board. This board allows for reading and generating encoder signals with very high precision and resolution.

The developed control system development was initially done in MALTAB 2022b-2023b versions, while deployment to the OP4510 was done in MATLAB 2019b with Opal-RT custom libraries and RT-LAB v2020.1.0.327 software. The developed control system is exported from MATLAB 2023b to 2019b and imported into the project for Opal-RT without any changes, while assisting and communication blocks necessary for correct OP4510 communication were added.

Fig. 4.6 shows the console part of the system during deployment to the OP4510. It allows for the live modifications of pre-set parameters and overview of system signals through scopes and displays. Console consists of 9 distinct sections:

- Left most part: scopes and displays for visualisations of measured/estimated signals
- "Recording triggers": triggers the recording of the data
- "Controller parameters": allows for modification of controller parameters
- "Observer settings": allows for modification of observer parameters
- "FAULTS parameters": allows reset of the fault flag and modification of trip limits. These are only for OPAL use, Danfoss inverter has non modifiable limits
- "References and PWM mod parameters": manual input of reference points, rate limiters, and different transition schemes in both manual and automatic regimes
- "Tests presets – spd, trq, mode": allows for switches between test presets
- "Load value": manually sets the torque reference and rate limiter
- Right most part: testing of DO signals, enabling of inverter and enabling of Braking Resistor, as well as creation of bus to go to the deployed model

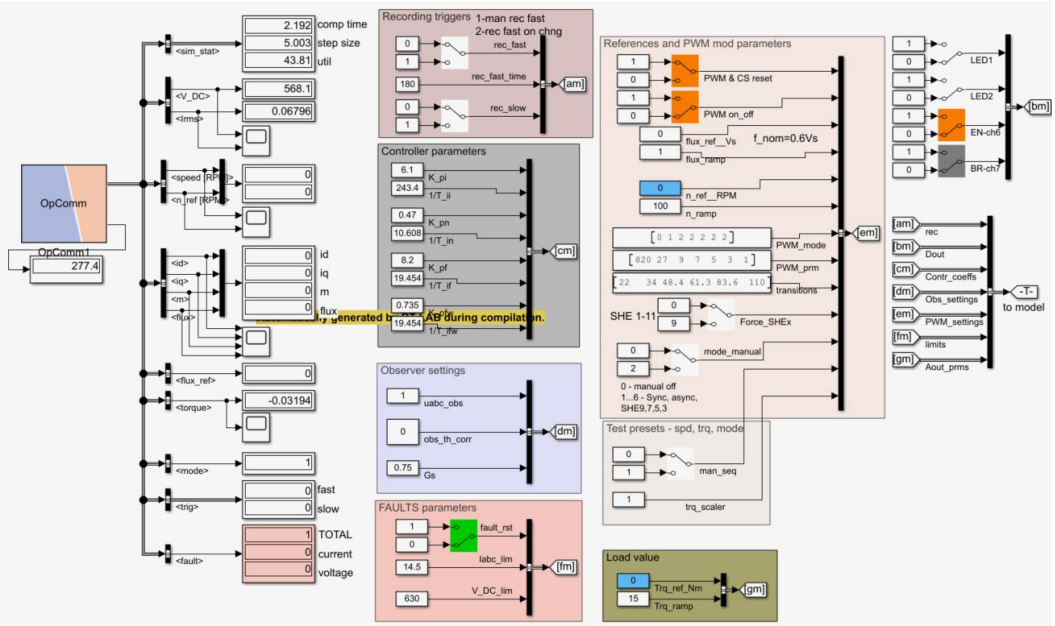

Fig. 4.6. Overview of the RT.LAB control console.

The system tailored for the Opal-RT is set to run with a fixed step of 5 us ('step size'), with CPU utilization of 40 %–45 % ('util') and no overruns during extended run time periods.

On demand data recording is set up with a high resolution of 50 kHz for a short period of time ('rec_fast'), and with a down sampled resolution of 2 kHz for an extended amount of time ('rec_slow').

4.2. Control system transition: from train to lab

An actual control system is being developed for the EMU implementation. However, the testing is carried out on a downscaled laboratory setup, thus necessitating adjustment of all control system parameters.

4.2.1. Induction motor parameters

Induction motor used for testing is ABB M2AA100LB-4 3GAA102002-ADE [107]. It is a 3-phase, 2 pole pair motor. The main parameters from the producer's datasheet for the continuous operation (S1) are shown in Table 4.1.

Table 4.1 S1 Working Point Parameters

Parameter name	*Units*	*Value*
Output power (on shaft)	kW	3
Stator voltage LL (V_{1rms})	V	380
Stator current	A	6.58
Power factor	-	0.85
Frequency	Hz	50
Slip	%	4.67
Rotational speed	RPM	1430
Mechanical torque	Nm	20
Maximum torque	Nm	58
Efficiency	%	85.0
Current, slip=0	A	2.74

For the proper operation of the control system, an equivalent circuit of the test motor is necessary. Testing and equivalent circuit extraction are done in accordance with IEC 60034-28 standard.

Motor was tested at 30, 40, 50, and 60 Hz, where 50 and 60 Hz are nominal voltages from the nameplate, while testing at lower frequencies is done to go further into saturation of the motor. At nominal voltages it is not possible to go above nominal voltage, as the laboratory stand is limited to a rectified 3 phase 380 Vrms grid voltage with overmodulation at $m = 1.15$ due to the fact as DC-link voltage is $V_{DC} = 545\ V$.

At each frequency no-load, blocked rotor, and load curve tests were carried out, with at least 10 measurement points. Stator resistance was measured directly with micro-ohmmeter.

Table 4.2 summarises the results of equivalent circuit tests. Table 4.2 shows the nominal value of the magnetizing inductance at nominal flux and frequency, while the non-linear curve is shown in Fig. 4.7. Magnetizing inductance is shown as a function of stator line voltage normalised to nominal frequency of 50 Hz.

Table 4.2 Equivalent Circuit Parameters

Parameter name	*Units*	*Value*
Stator resistance at 20°C	mΩ	1817
Rotor resistance at 20°C	mΩ	1478
Magnetizing inductance	mH	230
Leakage inductance ($L_{\sigma s} = L_{\sigma r}$)	mH	9.5
Inertia of the rotor	kgm^2	0.022
Viscous friction coefficient	Nms/rd	0.002

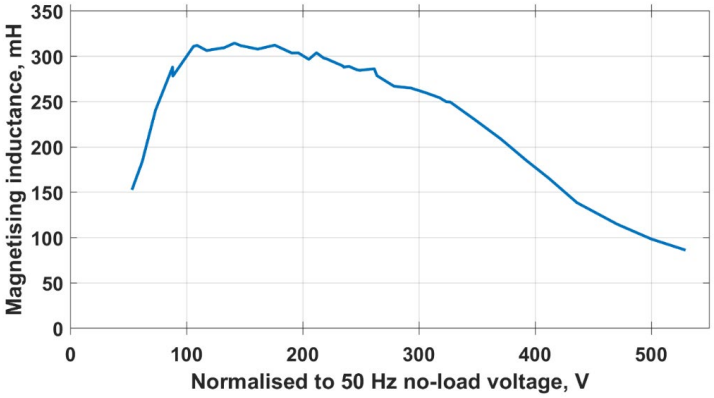

Fig. 4.7. Magnetising inductance curve of the test motor.

4.2.2. Controller coefficients

Following updated motor parameters control system coefficients are recalculated based on the approach outlined in chapter 2.5.4. Recalculated PI controller coefficients and respective parameters are shown in Table 4.3.

Table 4.3 Summary of the Controller Coefficients

Controller	T_i	$k_i = \frac{k_p}{T_i}$	k_p	Rise time	Settling time	Overshoot
d-/q- current	4.1 ms	1488	6.1	4.3 ms	12.5 ms	4.9 %
Speed	94.3 ms	5.0	0.47	50.3 ms	313 ms	22.8 %
Flux	45.5 ms	250	11.4	46.4 ms	215 ms	13.7 %
Field-weakening	45.5 ms	16.3	0.74			

For the speed controller damping factor of $\xi = 0.707$ and bandwidth of $\omega_n = 15\, rad/s$ are used. While for the flux controller damping factor of $\xi = 0.707$ and bandwidth of $\omega_n = 22.5\, rad/s$ are used. The bandwidth values are different from EMU control system as to have both controller time constant and rise time be at least 10 times larger than d-/q- current controller values.

4.2.3. Traction limiting characteristic

Traction limiting characteristic is adjusted based on the motor capabilities and on the loading capabilities of the coupled motor and its inverter. The output torque limit, which is able to limit electromagnetic torque, is reduced proportionally to the traction characteristic of the large traction motor.

It is downscaled based on torque in a constant torque region from 3000 Nm to 20 Nm by a factor of 150. Transition points between regimes 1)–2) and 2)–3) are kept the same for consistency, while the transition point between 3)–4) is changed according to the 15 A instantaneous current limit of the frequency converter. As was described before in chapter 2.2.2 traction characteristic is tailored not only based on motor limitation but also based on limitation of the inverter.

Additionally, the maximum speed is reduced to 120 Hz, or approximately 3450–3600 RPM depending on the slip. The loading inverter is locked to 120 Hz of maximum fundamental frequency, and mechanical coupling and mechanical alignment have been designed for speeds only up to 4000 RPM.

Traction characteristic has the following regions:

1) 0–350 RPM: gradual increase of torque from 6.7 Nm to 20 Nm. It is kept to be consistent with a large traction motor.
2) 350–1720 RPM: constant torque region limited by $T_{out} = 20\ Nm$.
3) 1720–2600 RPM: constant power region limited by $P_{out} = 3.6\ kW$.
4) 2600–3600 RPM (max speed): $T_{elm}\omega_m \cong constant$ or $T_{em} \propto \frac{1}{\omega_s^2}$ region.

Fig. 4.8 shows the reference torque limit set in control system for observer calculated electromagnetic torque. Load torque limit is 75 % of the control system limits as the inverter is limited to 15 Nm to give a safety margin for the control system not to go into saturation. In addition, many tests are carried out at 50 % of the load torque limit.

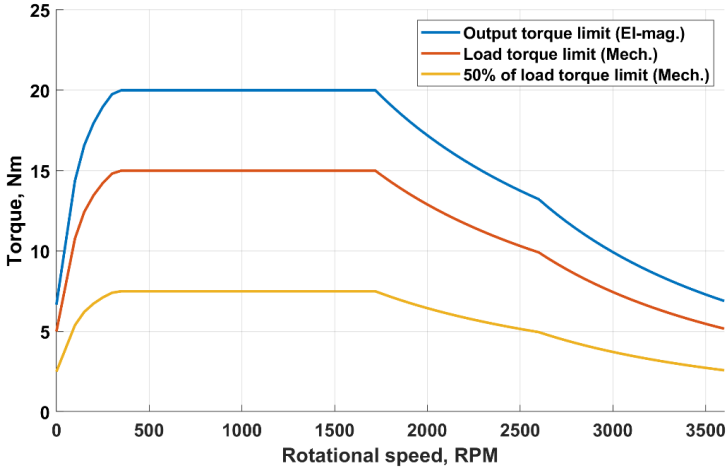

Fig. 4.8. Reference traction characteristic of the laboratory IM.

4.2.4. PWM transition scheme

All tests have identical hybrid PWM transition types and points of transition. Parameters of each PWM modulation mode are summarized in Table 4.4 and Fig. 4.9 showing the hybrid PWM transitions scheme in visual form. Used in laboratory testing, the transition scheme is mostly identical to the one used during modelling, with the only difference being that the SHE 3 to SHE 1 transition point is shifted down, so it is in the speed range.

Table 4.4 Hybrid PWM Transitions Scheme

PWM mode	**Switching frequency**	**Fundamental frequency range**
Asynchronous	820 Hz	0…22 Hz
Synchronous 27	594…918 Hz	22…34 Hz
SHE 9, solution 1	646…919.6 Hz	34…48.4 Hz
SHE 7, solution 1	726…919.5 Hz	48.4…61.3 Hz
SHE 5, solution 1	674.3…919.6 Hz	61.3…83.6 Hz
SHE 3, solution 1	585.2…770 Hz	83.6…110 Hz
SHE 1	330…360 Hz	110…120 Hz

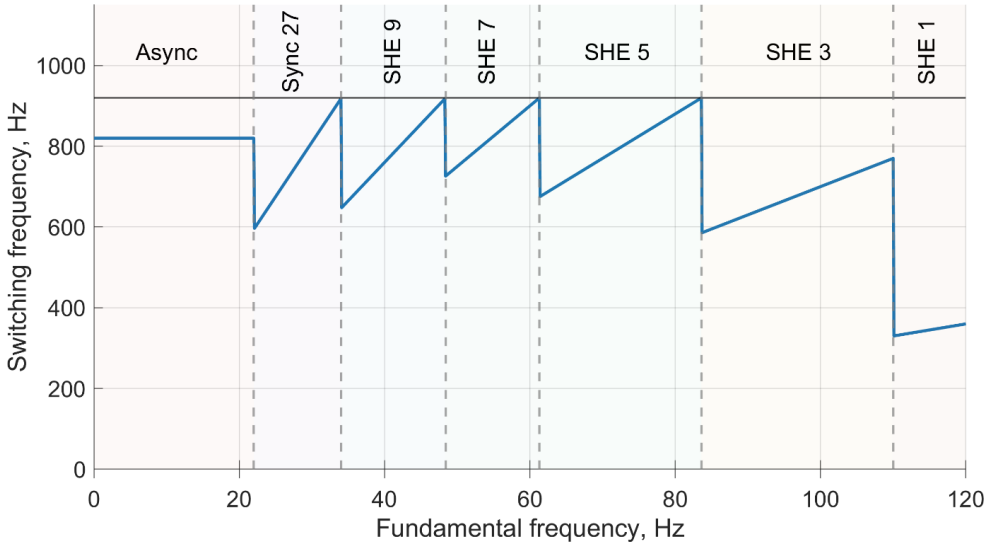

Fig. 4.9. Hybrid PWM transitions scheme (used in laboratory).

Additional overarching parameters:

- PWM transitions hysteresis band: 1 Hz;
- hybrid observer G_s gain: 0.75;
- reference nominal flux: 0.6 Vs;

– minimum allowed flux in field-weakening regime: 10 % of nominal – 0.06 Vs;
– field-weakening modulation index limit – $m = 1.09$, which at 550 VDC corresponds to 367 V_{1RMS}.

4.3. Analysis of stator current harmonic content and motor losses

This subchapter focuses on the harmonic analysis of the induction motor stator current and induction motor losses during static operation. Modelling addresses losses in the power module, while laboratory tests allow for direct measurement of motor losses and efficiency. However, converter losses cannot be measured directly. Several tests were carried out to depict the THD, WTHD, and converter losses, while outlining the differences between modulation modes.

The sets of tests are designed to be as close as possible to the modelling ones. Speeds are maintained at predefined levels with reference torques scaled down. All calculations and data post-processing are performed in the same way as in the modelling phase. Harmonic analysis is conducted according to the methodology provided in chapter 3.1.

4.3.1. Overview of modulation performance in static regime

The first test is an overview of PWM in each mode. Table 4.5 provides an overview of used reference point, where TrChar is the load limit reference provided in Fig. 4.8.

Table 4.5 Overview of Reference Points

PWM mode	**Reference speed, RPM**	**Reference torque, Nm | Switching frequency, Hz**					
		No-load (A)		0.5 TrChar (B)		TrChar (C)	
Asynchronous (1)	600	0	820	7.5	820	15	820
Synchronous 27 (2)	900	0	812	7.5	834	15	858
SHE 9 (3)	1200	0	762	7.5	778	15	794
SHE 7 (4)	1650	0	827	7.5	841	15	860
SHE 5 (5)	2100	0	772	6.14	786	12.28	805
SHE 3 (6)	3000	0	702	3.72	714	7.45	733
SHE 1 (7)	3450	0	346	2.82	351	5.63	360

Table 4.6 provides the stator current performance indicators, with Fig. 4.10 providing harmonic values at integer harmonic orders in relation to the fundamental frequency. Fig. 4.10 excludes the 1st harmonic as it is significantly different between no-load and fully loaded regime. While current waveforms in each regime and under each loading condition are shown in Appendix D.

It can be seen that each regime on the laboratory setup works as intended with expected harmonics appearing in each regime.

Asynchronous PWM as expected has harmonics at $f_{sw} - 2 \cdot f_0$, $f_{sw} + 2 \cdot f_0$, $2 \cdot f_{sw} - f_0$, $2 \cdot f_{sw} + f_0$ etc [86], which corresponds at no-load to 780, 860, 1620, and 1660 Hz respectively, and harmonic order of 39th, 43rd, 81st, and 83rd.

Synchronous PWM with the ratio of $m_f = 27$ has the most prominent harmonics at $m_f \pm 2$ and at $2 \cdot m_f \pm 1$ [86], which is 25th, 29th, 53rd and 55th harmonics respectively.

Selective harmonic elimination has harmonics eliminated as outlined in Table 1.1 with next odd non-triplen boosted harmonics annotated in Fig. 4.10.

It can be seen that SHE 1 has poor harmonic performance especially at no-load, where it is only the case when harmonic current is higher than fundamental, which is evident from the waveform in Fig. D.1. As was noted previously, SHE 1 and/or square wave modulation should be avoided if possible. However, the control system is able to accurately track the speed of the motor at no-load and loaded conditions even in SHE 1.

Table 4.6 Summary of the Stator Current Indicators

Mode	**THD, %**			**WTHD, %**			I_1			$I_{2\ldots50}$		
/ Load	(A)	(B)	(C)	(A)	(B)	(C)	(A)	(B)	(C)	(A)	(B)	(C)
(1)	11.44	10.64	8.82	1.78	2.30	2.09	3.46	4.82	7.41	0.40	0.51	0.65
(2)	22.21	17.61	13.56	2.21	2.00	1.86	3.49	4.92	7.50	0.77	0.87	1.02
(3)	42.94	29.81	20.14	2.94	2.14	2.03	3.51	4.99	7.60	1.51	1.49	1.53
(4)	29.85	20.67	12.89	3.51	2.78	1.63	3.41	5.03	8.31	1.02	1.04	1.07
(5)	48.70	26.59	15.71	6.10	3.53	2.44	2.54	4.72	8.42	1.23	1.25	1.32
(6)	55.29	24.82	13.37	11.03	5.11	2.95	1.84	4.15	8.04	1.02	1.03	1.08
(7)	155.55	72.57	38.94	33.25	15.79	8.57	1.77	3.79	7.26	2.76	2.75	2.83

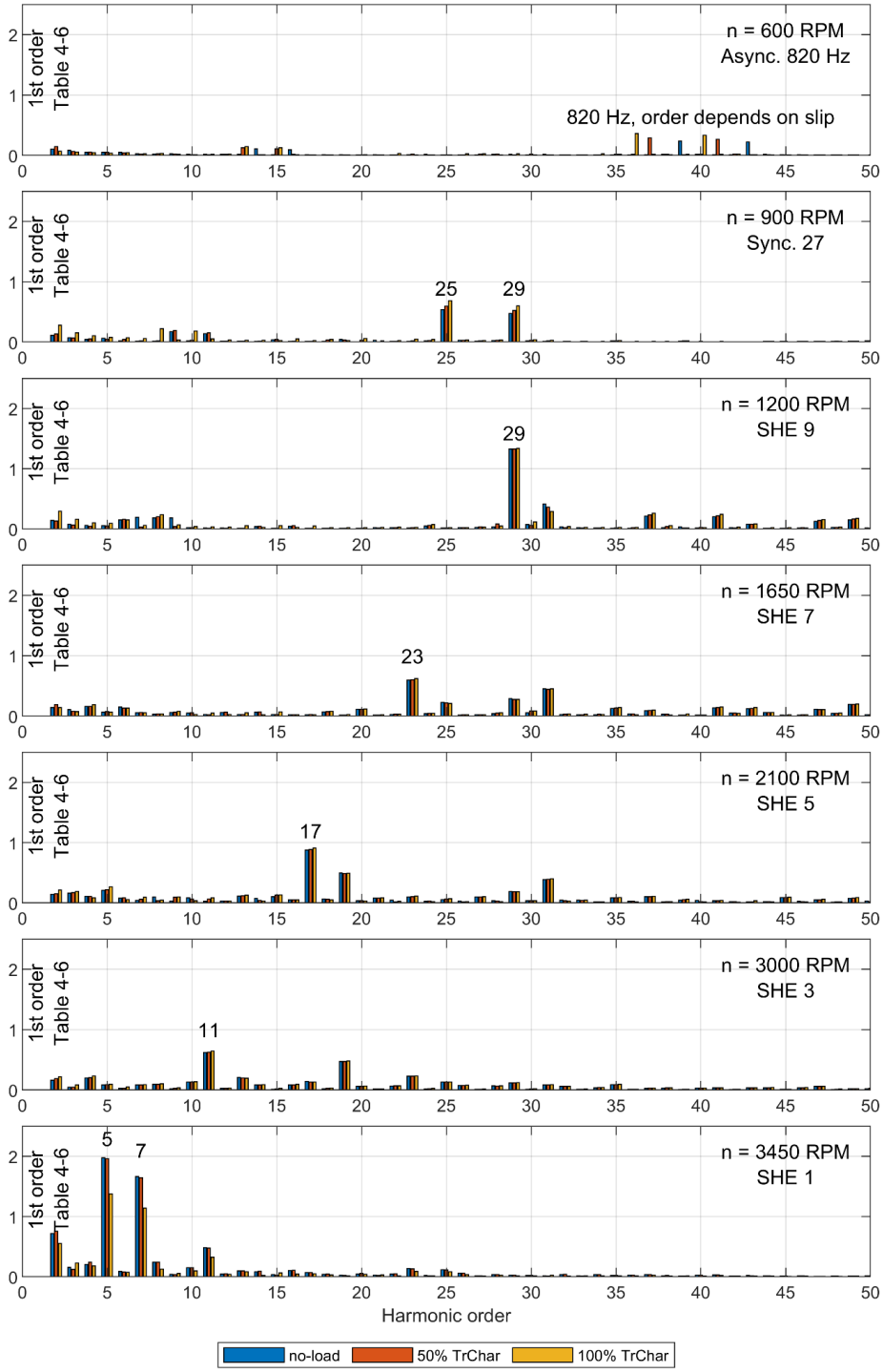

Fig. 4.10. FFT in each regime (excludes 1st harmonic).

4.3.2. Comparison of synchronous and SHE PWM

The following set of tests revolves around comparison of the synchronous PWM and SHE PWM performance in different conditions.

4.3.2.1. At the same switching frequency

The first test is done according to the Table 4.7 reference points. This test outlines the difference between synchronous and SHE PWM, as was done in chapter 3.1.2.1.

Table 4.7 Overview of Reference Points

PWM mode	**Reference speed, RPM**	**Switching frequency, Hz**		
		No-load (A)	7.5 Nm (B)	15 Nm (C)
Synchronous 23 (1)	900	692	710	730
SHE 11 (2)				
Synchronous 19 (3)		571	587	604
SHE 9 (4)				
Synchronous 15 (5)		451	463	477
SHE 7 (6)				
Synchronous 23 (7)	1140	876	895	915
SHE 11 (8)				
Synchronous 19 (9)		724	739	756
SHE 9 (10)				
Synchronous 15 (11)		571	584	597
SHE 7 (12)				

Table 4.8 summarises the stator current performance indicators, while Table 4.9 summarises motor input power, output power, total losses and efficiency.

Table 4.8 Summary of the Stator Current Indicators

Mode / n-ref	**THD, %**			**WTHD, %**			I_1			$I_{2\ldots50}$		
	(A)	(B)	(C)	(A)	(B)	(C)	(A)	(B)	(C)	(A)	(B)	(C)
(1)	42.83	32.14	22.68	2.47	2.38	1.81	3.50	4.92	7.51	1.50	1.58	1.70
(2)	56.04	41.47	28.73	2.97	2.62	1.73	3.52	4.93	7.51	1.97	2.04	2.16
(3)	51.31	38.49	27.32	2.83	2.81	2.31	3.51	4.90	7.47	1.80	1.88	2.04
(4)	57.65	42.16	29.03	2.75	2.50	2.14	3.52	4.90	7.47	2.03	2.07	2.17
(5)	67.05	50.04	35.29	4.05	3.44	2.72	3.52	4.90	7.46	2.36	2.45	2.63
(6)	68.60	50.18	34.38	3.45	2.94	2.41	3.52	4.91	7.47	2.42	2.46	2.57
(7)	39.26	29.16	20.85	2.87	2.31	1.94	3.51	4.97	7.58	1.38	1.45	1.58
(8)	48.06	34.60	23.55	2.96	2.31	1.86	3.52	4.98	7.57	1.69	1.72	1.78
(9)	46.75	34.99	25.02	3.06	2.75	2.47	3.52	4.95	7.55	1.64	1.73	1.89
(10)	44.88	32.03	21.59	2.73	2.19	2.09	3.52	4.95	7.55	1.58	1.59	1.63
(11)	60.33	44.74	31.75	4.27	3.51	2.86	3.53	4.95	7.54	2.13	2.22	2.40
(12)	53.32	38.07	25.63	3.10	2.48	2.30	3.53	4.95	7.55	1.88	1.89	1.93

Table 4.9 Summary of the Motor Power Indicators

Mode / n-ref	P_{in}, W			P_{out}, W			P_{loss}, W			η, %		
	(A)	(B)	(C)	(A)	(B)	(C)	(A)	(B)	(C)	(A)	(B)	(C)
(1)	88	833	1690	46	726	1401	41.9	107.0	288.2	52.5	87.2	82.9
(2)	101	845	1698	46	726	1401	54.8	119.1	297.1	45.9	85.9	82.5
(3)	98	845	1703	47	728	1406	51.0	116.6	297.2	48.0	86.2	82.5
(4)	108	853	1711	47	728	1406	60.8	124.3	305.1	43.6	85.4	82.2
(5)	121	868	1732	47	728	1406	74.1	139.7	326.3	38.7	83.9	81.2
(6)	129	876	1734	47	728	1406	82.4	147.8	327.7	36.1	83.1	81.1
(7)	132	1059	2110	78	933	1796	53.9	126.4	313.6	59.3	88.1	85.1
(8)	133	1059	2105	79	933	1796	54.8	125.6	309.0	59.0	88.1	85.3
(9)	136	1065	2125	78	935	1802	58.3	130.6	323.0	57.2	87.7	84.8
(10)	135	1060	2114	78	935	1801	56.9	125.7	312.3	57.8	88.1	85.2
(11)	155	1085	2147	79	935	1802	76.8	150.1	345.0	50.6	86.2	83.9
(12)	149	1073	2128	78	934	1801	70.3	138.4	326.9	52.7	87.1	84.6

In this test pairs of synchronous and SHE PWM were analysed and tested for current THD/WTHD as well as for motor losses, which are measured directly with the help of torque transducer.

It can be seen based on the results that at lower m_f ratios both WTHD and motor losses are substantially lower, while at higher speeds and/or higher m_f ratios WTHD is comparable.

Combining modelling results and laboratory measurements, it can be concluded that SHE, compared with the synchronous PWM at the same switching frequency, provides comparable results at the no-load condition, while lower power module and motor losses at loaded conditions.

4.3.2.2. At traction characteristic reference

This subchapter covers the comparison of operation with mode transition scheme utilizing SHE and synchronous PWM with the same switching frequency. Instead of SHE 9, 7, 5, 3, and 1, synchronous PWM was selected with switching to a fundamental frequency ratio of 19, 15, 11, 7, and 3, such that the switching frequency pattern stays consistent with the original SHE PWM scheme.

Results covering output torque, switching frequency, total motor losses, THD, and WTHD are shown in Fig. 4.11.

The first thing should be noted that the system with synchronous PWM was tested up to 3300 RPM, up to the transition to the ratio of 3, because the system was unstable and could not operate with the m_f ratio of 3, while with SHE 1 the system was operational, however having very high THD.

Based on the test results it can be concluded that SHE 9/sync. 19 results are comparable. However, the higher speed / lower m_f ratio clearly shows the comparative advantage of the SHE, as both losses and THD/WTHD are superior compared to the synchronous, as well as the system being stable and operational at SHE 1.

Maximum motor loss difference is 98 W at 2700 RPM or up to 15 %.

- In the 3rd phase, SHE, on average, has 6 % higher losses.
- In the 4th phase, SHE, on average, has 2 % lower losses.
- In the 5th–6th phase, SHE, on average, has 10 % lower losses.

At the same time, in all phases, synchronous PMW has higher THD and higher WTHD.

It can be concluded that below $m_f = 19$, it is advisable to use pre-programmed PWM as in this case SHE-PWM. These results show that both THD/WTHD and motor losses are superior, while modelled power module losses show slight benefit in the use of SHE with no detriment.

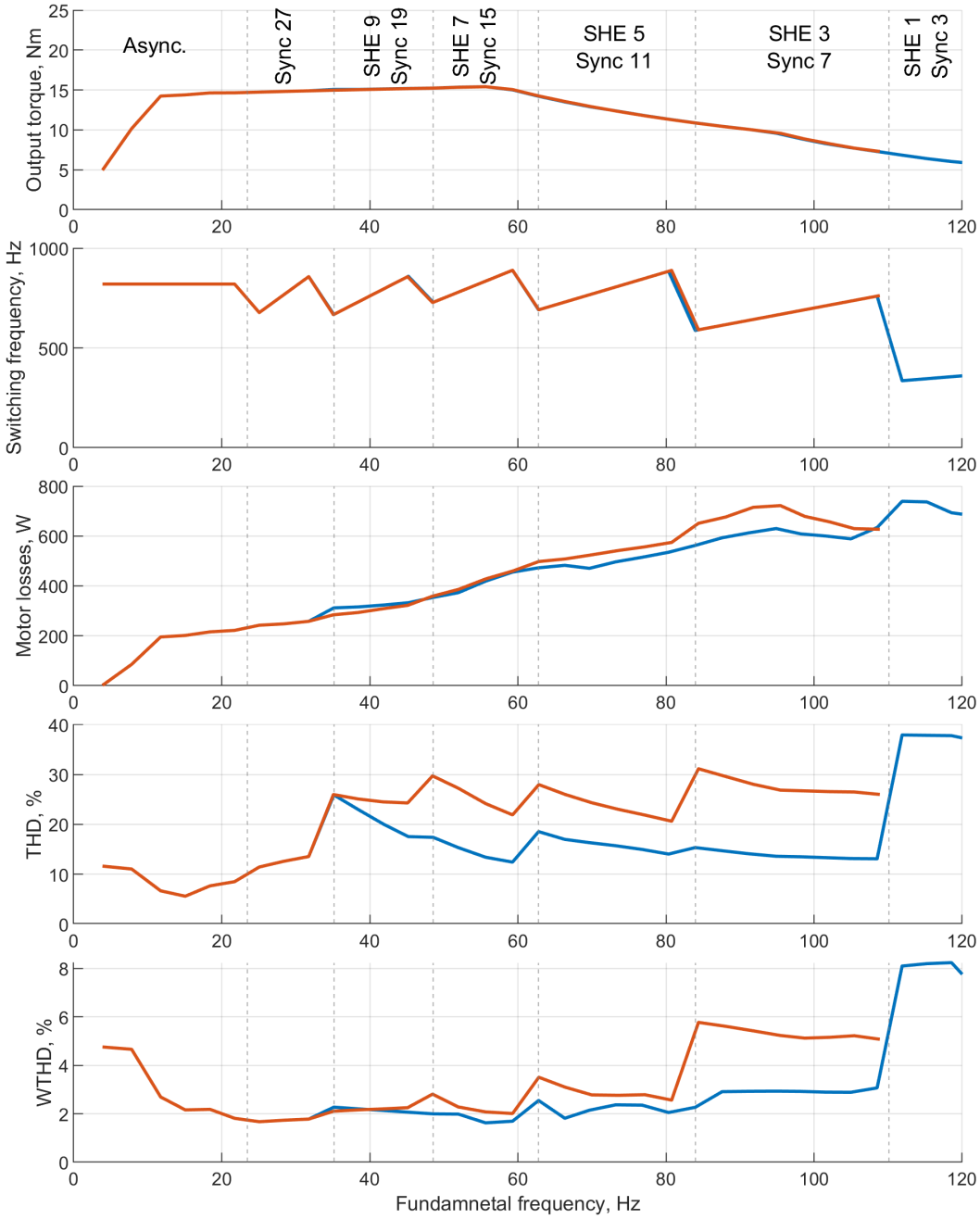

Fig. 4.11. Comparison of SHE and Synchronous PWM.

4.3.3. Comparison of different SHE solutions

The next test is the comparison of SHE solutions. A single point at 900 RPM is measured under four sets of solutions at three loading conditions. An overview of reference points is shown in Table 4.10.

Table 4.10 Overview of Reference Points

PWM mode	**Reference speed, RPM**	**Switching frequency, Hz | Modulation index**					
		No-load (A)		7.5 Nm (B)		15 Nm (C)	
SHE 9, Solution 1 (9–1)	900	572	0.608	588	0.645	605	0.689
SHE 9, Solution 2 (9–2)							
SHE 9, Solution 3 (9–3)							
SHE 9, Solution 4 (9–4)							
SHE 7, Solution 1 (7–1)		451		464		477	
SHE 7, Solution 2 (7–2)							
SHE 7, Solution 3 (7–3)							
SHE 7, Solution 4 (7–4)							

Results are presented in the same way as in previous sections with current performance indicators in Table 4.11, and motor power indicators in Table 4.12.

Table 4.11 Summary of the Stator Current Indicators

Mode / n-ref	**THD, %**			**WTHD, %**			I_1			$I_{2...50}$		
	(A)	(B)	(C)	(A)	(B)	(C)	(A)	(B)	(C)	(A)	(B)	(C)
(9–1)	60.19	44.30	30.86	2.90	2.33	2.48	3.51	4.92	7.48	2.12	2.18	2.31
(9–2)	57.55	42.13	29.21	2.88	2.26	2.42	3.51	4.92	7.49	2.02	2.07	2.19
(9–3)	66.69	49.50	34.73	3.52	2.66	2.61	3.53	4.93	7.48	2.35	2.44	2.60
(9–4)	63.69	47.04	32.89	3.11	2.51	2.49	3.51	4.93	7.49	2.24	2.32	2.46
(7–1)	68.80	50.03	34.63	3.60	2.70	2.70	3.51	4.93	7.50	2.42	2.47	2.60
(7–2)	73.84	54.16	37.67	3.69	2.78	2.76	3.52	4.93	7.50	2.60	2.67	2.82
(7–3)	84.04	61.83	43.25	4.42	3.16	2.99	3.53	4.95	7.50	2.97	3.06	3.24
(7–4)	78.48	57.59	40.14	4.07	2.94	2.85	3.52	4.94	7.50	2.77	2.85	3.01

Table 4.12 Summary of the Motor Power Indicators

Mode / n-ref	P_{in}, W			P_{out}, W			P_{loss}, W			$\eta, \%$		
	(A)	(B)	(C)	(A)	(B)	(C)	(A)	(B)	(C)	(A)	(B)	(C)
(9–1)	117	869	1734	47	729	1409	70.3	139.9	324.8	40.0	83.9	81.3
(9–2)	118	868	1734	47	730	1409	71.2	138.9	325.2	39.7	84.0	81.3
(9–3)	129	880	1749	47	730	1409	82.1	150.2	340.0	36.3	82.9	80.6
(9–4)	125	876	1741	47	730	1409	78.3	146.1	331.9	37.5	83.3	80.9
(7–1)	138	890	1756	48	731	1411	90.5	159.2	345.2	34.6	82.1	80.3
(7–2)	144	896	1767	48	731	1411	96.3	165.0	355.9	33.1	81.6	79.9
(7–3)	166	921	1793	48	731	1410	117.8	190.1	382.6	28.9	79.4	78.7
(7–4)	156	909	1778	48	731	1410	108.1	178.0	367.6	30.7	80.4	79.3

It can be seen that there is a substantial difference in WTHD and total power loss with different SHE solutions. WTHD has the lowest WTHD/motor losses with SHE 9–2 and SHE 7–1 and the highest with SHE 9–3 and 7–3 and differences ranging from 8 % to 20 %, while motor losses change in accordance with WTHD. Lower the WTHD and lower the losses of the motor, with the difference in losses ranging from 5 % to 30 %.

Based on modelling and testing results, it can be concluded that each SHE solution has slightly different performance in regard to WTHD, power module losses, and motor losses. Due to that, it is possible to optimize WTHD and losses in traction operation for EMU both in acceleration-deceleration (under load) and in maintaining speed (low load).

4.4. Control system performance

The next set of laboratory tests is done to evaluate the control system's performance with the developed control system. The set of tests is done in the same way or closely resembling the ones in the modelling section.

4.4.1. Flux response

The first test is induction motor magnetization, in other words performance of the flux loop. Test is conducted by applying reference flux of $\psi_{nom} = 0.6\,Vs$ with the ramp close to the step response of $8 \cdot \psi_{nom} = 4.8\,Vs/second$ and with the ramp of $2 \cdot \psi_{nom} = 1.2\,Vs/second$.

The test results with estimated motor flux and magnetising current (i_d) are shown in Fig. 4.12. Could be seen that motor flux closely resembles the calculated value of the motor flux, however, slightly worse compared to the modelled version (Fig. 3.7). That is likely due to the fact of non-linear

nature of magnetisation inductance and simplification during calculation process, as calculation uses only nominal value of magnetising inductance.

Both results provide reliable results and could be seen that system reaches nominal flux value with fast ramp with 18% overshoot and with ramp of 0.5 second with only 3% overshoot. Based on the flux PI regulator performance the results are within expected margins. However, during testing 0.5 second ramp is used to minimise overshoot, as that is not time critical.

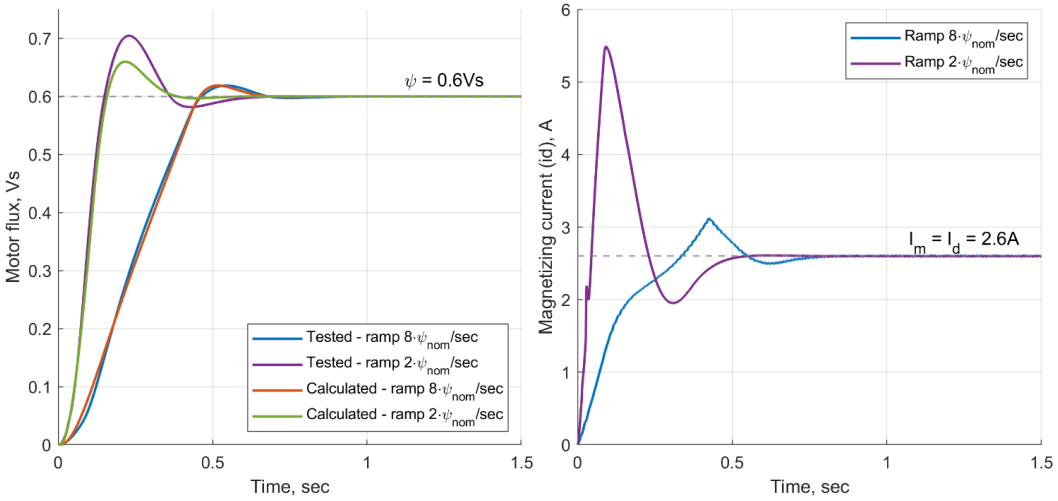

Fig. 4.12. Flux response: tested and calculated.

4.4.2. Speed response

The next test is the response of the system to the change in reference speed. Two sets of tests were carried out:

1. Acceleration 0–3600 RPM (n max) with the only limiter being traction characteristic. Results are shown in Fig. 4.13. Only acceleration is tested for as at rapid deceleration even with used braking resistor DC-link voltage rises significantly with very fast ramp / or no-limiter. Therefore, it was decided to exclude this test for the safety of equipment. In addition, hybrid observer struggles with very fast dynamics, as is shown in 4.4.4.
2. Acceleration and deceleration 0–3600 (n max)–0 RPM with 500 RPM/s^2 rate limiter. Results are shown in Fig. 4.14.

Each of the figures shows the same set of plots:

- Left upper: motor speed, RPM
- Right upper: output shaft torque, Nm (blue), electromagnetic torque, Nm (estimated by the hybrid observer) (red).
- Left lower: 1st RMS harmonic of the stator voltage, V (blue)

– Right lower: RMS stator current, A (blue), motor flux, Vs (estimated by the hybrid observer) (red)

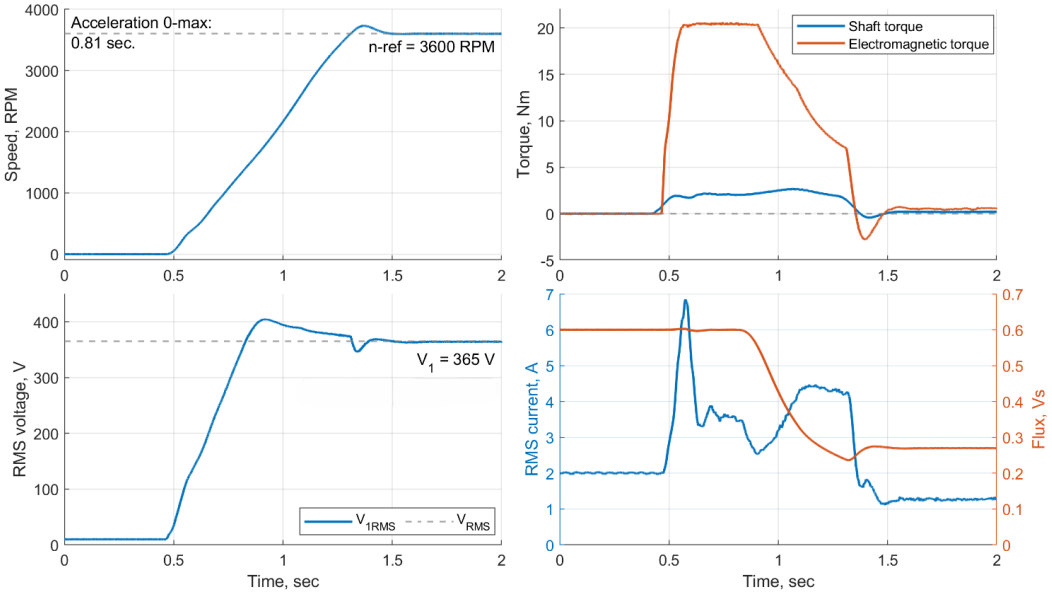

Fig. 4.13. Motor acceleration at traction characteristic.

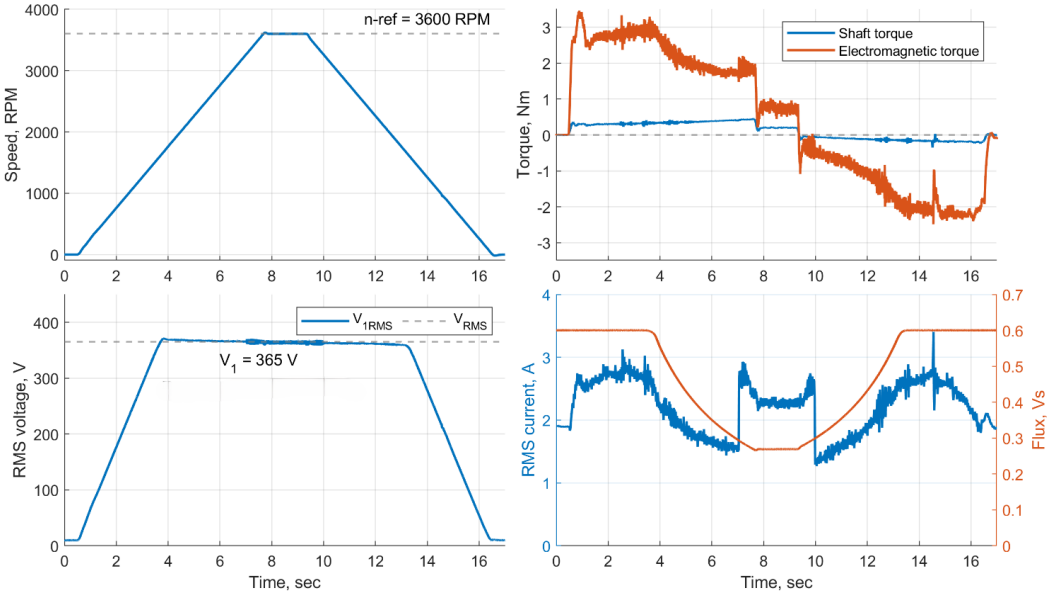

Fig. 4.14. Motor acceleration and deceleration at 500 RPM/s^2 ramp.

Performance indicators of the test results are summarised in the table below. The reasoning for the 500 RPM/s^2 rate limiter is the same as was outlined in chapter 3.2.2.

Table 4.13 Summary of Performance Indicators

	TrChar rate limiter	500 RPM/s^2 rate limiter
Speed overshoot, acceleration	130 RPM / 3.6 % overshoot	17.7 RPM / 0.5 % overshoot
Speed overshoot, deceleration	-	–9 RPM
Feedback-based voltage limiter 365 Vrms limit	40 Vrms / 11.0 % overshoot	6 Vrms / 1.6 % overshoot
Acceleration time	0.81 seconds ≈4400 RPM/s^2	7.2 seconds
Deceleration time	-	7.2 seconds

It can be seen that the system is stable and successfully reaches the reference speed with both ramps while also smoothly transitioning between regimes of modulation, following a pre-defined transition scheme.

Acceleration time is substantially faster at the traction characteristic limit (0.81 seconds instead of 2.41 seconds) due to the substantial inertia difference of 360 times (8 kgm^2 and 0.022 kgm^2), while the traction characteristic ratio between large and small motors is 150 times. In addition, the reference speed is 3600 RPM instead of 4780 RPM in the model.

While for the 500/s^2 limited acceleration/deceleration speed overshoot is the same, and voltage overshoot is slightly lower.

4.4.3. Transitions between PWM modes

This section shows the transition between PWM modes. Current waveforms are taken from the motor acceleration-deceleration test with 1500 RPM/s^2 outlined in the previous subchapter.

Select number of transitions in acceleration and deceleration regimes are presented in Fig. 4.15. Transitions are selected in the same way as during the modelling phase to highlight how the system performs on a real system. The dotted lines show exact moment when the transition happens.

Could be concluded that the modulation transitions happen smoothly even with high rates of acceleration.

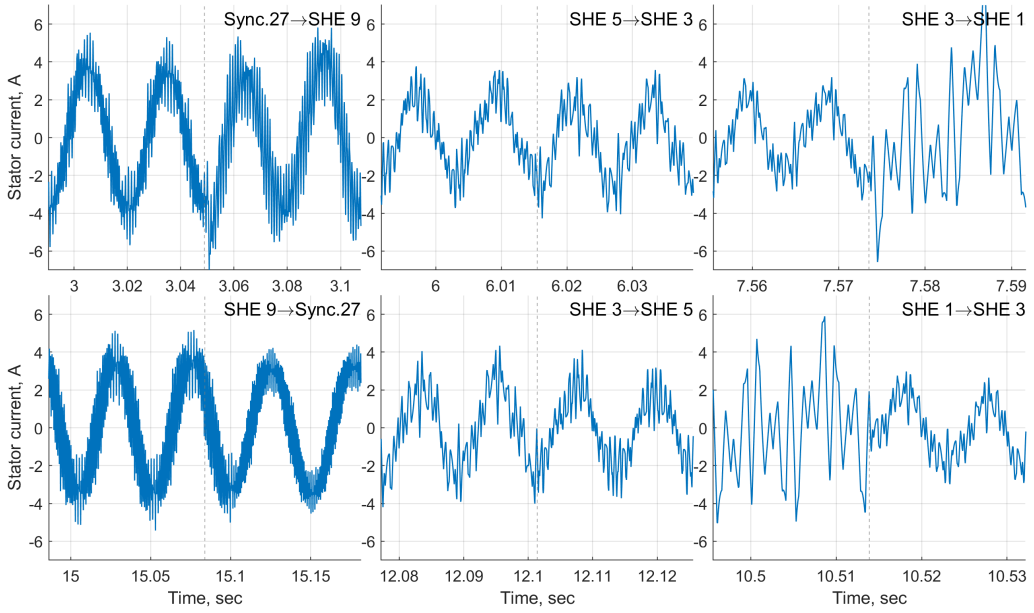

Fig. 4.15. Transitions between modulation regimes (500 RPM/s^2 limit).

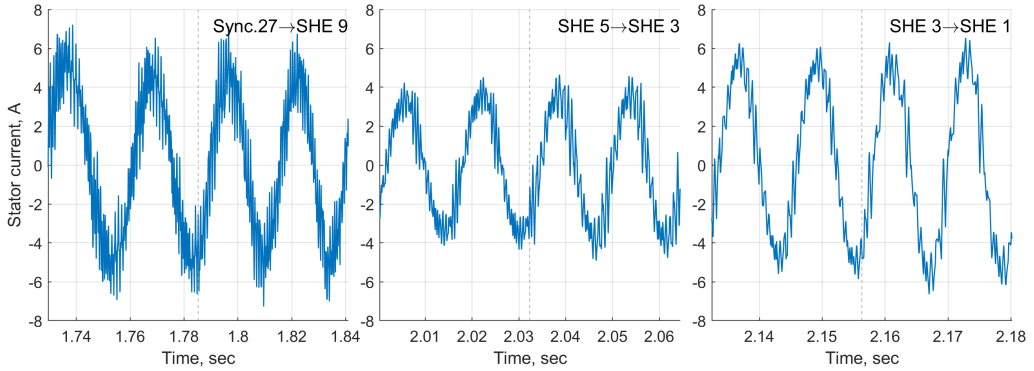

Fig. 4.16. Transition between modulation regimes (TrChar limit).

4.4.4. Hybrid observer operation

This section outlines fundamental current hybrid observer tracking performance. In Fig. 4.17/Fig. 4.18 is the same set of waveforms as in the Fig. 4.15/Fig. 4.16, with the former one showing phase A stator current I_α, while this one showing one of the phases after the $\alpha\beta$-transformation I_α and its estimated value $\widehat{I_\alpha}$.

It can be seen that with 500/s^2 rate as seen in Fig. 4.17 tracking is accurate in dynamic regime. However, at the traction characteristic limit, which amounts to approximately 4400 RPM/s^2 acceleration, the observer struggles to accurately track the stator current. That shows that there is a

practical limit on the performance of the observer. For this implementation, this dynamic is more than enough as 500 RPM/s^2 is already 4 times faster than the fastest acceleration of the train under consideration.

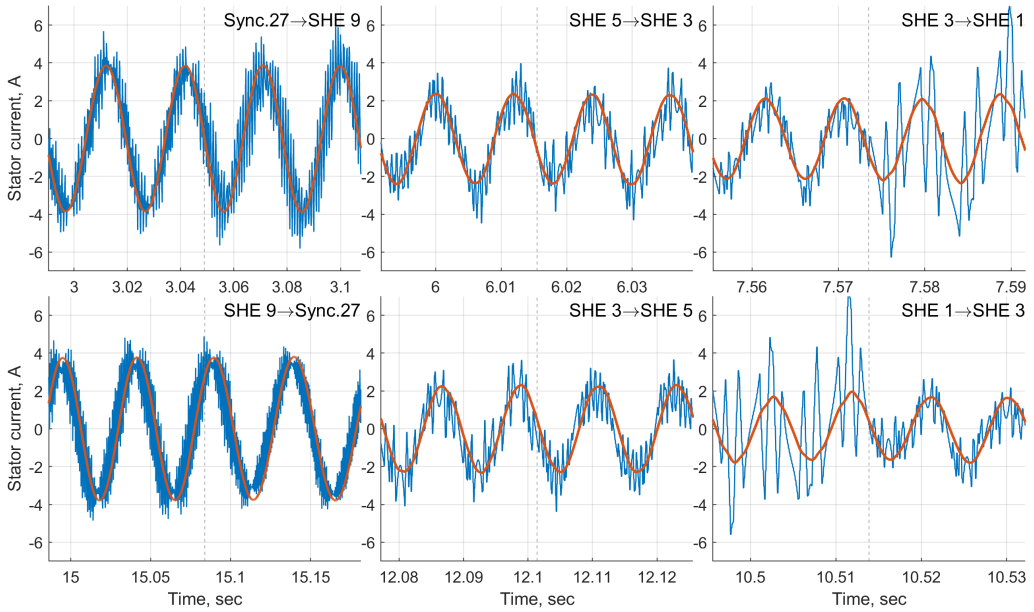

Fig. 4.17. Hybrid observer operation in transition regimes (500 RPM/s^2 limit).

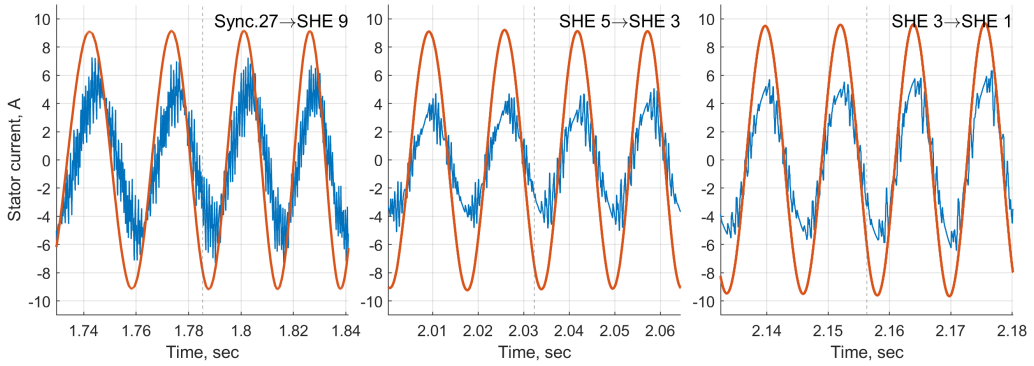

Fig. 4.18. Hybrid observer operation in transition regimes (TrChar limit).

An additional test was conducted at 3000 RPM with SHE 3 and at 3450 RPM with SHE 1 in no-load condition to outline the observer tracking in the most challenging regimes. Results of the observer tracking are shown in Fig. 4.19.

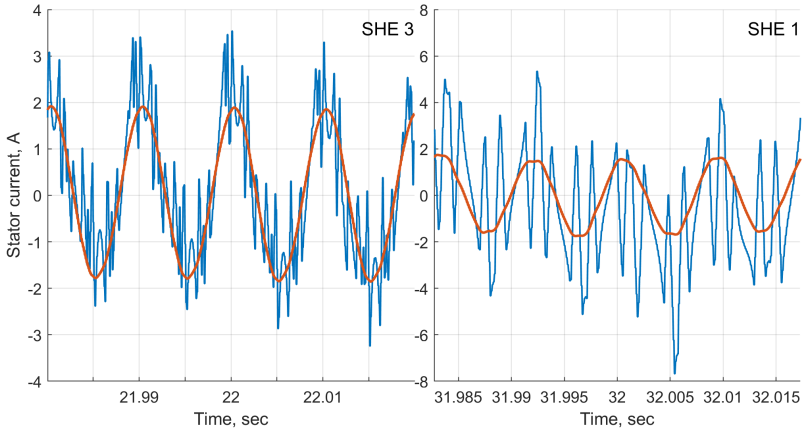

Fig. 4.19. Hybrid observer operation at no-load with SHE 3 and SHE 1.

Based on the results, it can be stated that the observer successfully tracks the fundamental current, even at SHE 1. However, with SHE 1, it is difficult to state visually as harmonics exceed the value of fundamental, and there is even harmonic at such a low m_f ratio. However, FFT analysis shows that the amplitude of the actual and tracked fundamental harmonics is equal.

4.4.5. Reaction to load

The last test is the reaction of the system to the disturbance, in this case loading of the motor. Three different point are selected:

- 0 RPM, 5 Nm, asynchronous PWM $f_{sw} = 820\ Hz$ (reaction at standstill);
- 1500 RPM, 15 Nm reference, SHE 7 (reaction at speed near the voltage limit at no-load);
- 3600 RPM, 5.17 Nm, SHE 1 (point at maximum speed).

First point represents reaction at standstill, second point represents reaction at speed near the voltage limit in no-load conditions, and the last point at maximum speed.

Results of tests are shown in Fig. 4.20 outlining motor speed, mechanical and electromagnetic torque, and the 1st RMS harmonic of the stator line voltage. With additional summary of the key indicators in the Table 4.14.

Table 4.14 in addition to the parameters in the modelling section provides measured mechanical torque and electromagnetic torque. It can be seen that the reference and actual torque differ slightly due to the error margin of the loading inverter.

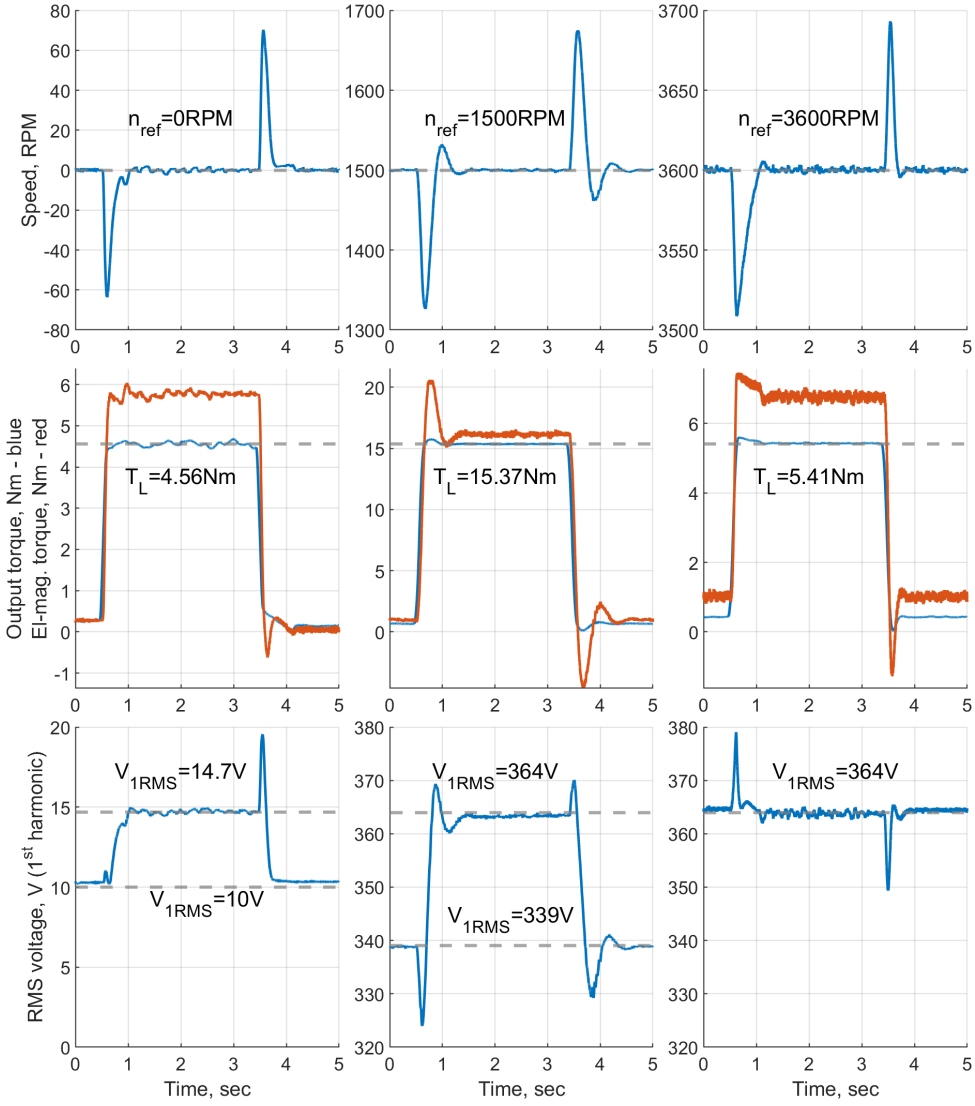

Fig. 4.20. Application of torque.

Table 4.14 Summary of the Performance Indicators

	Reference speed	0 RPM	1500 RPM	3600 RPM
	Reference torque	5 Nm	15 Nm	5.17 Nm
	Measured mechanical torque	4.56 Nm	15.37 Nm	5.41 Nm
	Electro-magnetic torque, Nm	5.82 Nm	16.08 Nm	6.69 Nm
	Electro-magnetic torque limit, Nm	6.7 Nm	20 Nm	6.9 Nm
	Voltage at no-load	10 V	339 V	364 V
	Voltage at load	14.7 V	364 V	364 V
Load application	Max. speed / Δn	2.3 / 2.3	1532.2 / 32.2	3606 / 6
	Min. speed / Δn	–63.6 / –63.6	1326.1 / –173.9	3508.5 / –91.5
Load removal	Max. speed / Δn	70.3 / 70.3	1675.2 / 175.2	3693.1 / 93.1
	Min. speed / Δn	–1 / –1	1461.9 / 38.1	3594.9 / 5.1

In conclusion, it can be stated that the control system operates properly at defined speed reference points when applying external disturbance in a step manner.

Conclusions

Due to the characteristics of power modules used in power converters of high-power medium voltage electric drives for railway applications, they are limited to switching frequencies of usually no more than 1 kHz, therefore necessitating a special hybrid pulse-width modulation (PWM) approach.

The developed hybrid PWM approach consists of conventional asynchronous and synchronous PWM and pre-programmed PWM – in the case of this research, it is selective harmonic elimination (SHE) PWM. Due to the inherent properties of the SHE PWM, it requires some version of the fundamental current estimator to reliably operate with a field-oriented control (FOC) system.

This research details a step-by-step methodology for the creation and validation of a traction drive control system specifically designed for railway applications with low switching frequency.

During the development process, an in-depth exploration of the hybrid PWM approach was conducted, encompassing its integration into the control system. This involved extensive research, algorithmic formulation, implementation on the control board, and subsequent evaluation on a downscaled laboratory setup.

The developed control system was initially simulated in Simulink, where it went through extensive testing and finetuning before being deployed into a real-time machine OPAL-RT OP4510 acting as a control board for downscaled laboratory setup. The subsequent phase involved the adaptation of all coefficients and limitations onto the laboratory setup with a set of similar tests to the model phase.

The following key conclusions can be drawn based on the research:

1) The optimized Newton–Raphson algorithm for solving SHE and selective harmonic mitigation (SHM) problems for 2-/3-level inverters demonstrates faster convergence and reduced computational effort compared to standard solvers. Such computational improvements are especially important for higher-order harmonics, complex solution spaces, iterative minimizations in cases of SHM and advanced optimization tasks.
2) FOC system utilizing hybrid observer and hybrid PWM transition scheme tested at the low switching frequency, limited to a maximum of 920 Hz, with an average of 735 Hz, exhibits stable performance.
3) Hybrid observer provides stable and accurate tracking with at least 500 RPM/s^2 acceleration and at no-load with lowest m_f ratios.
4) SHE provides lower measured motor losses – up to 16 %, with an average of 8 %, as well as lower calculated power module losses – up to 7 %, with an average of 1 %. These

results, however, are highly dependent on the load compared to an equivalent switching frequency with synchronous PWM for SHE 1, 3, 5, and 7. SHE 9 and 11 provide similar results to synchronous PWM, as the harmonics are far enough from the fundamental frequency to have a significant effect.

5) Many SHE stages have several unique sets of solutions. Each solution at the same modulation index eliminates the same harmonics while providing different WTHD and losses. Experimental testing has shown that motor losses vary by up to 30 %, with an average of 15 %, while simulations have indicated that power module losses vary by up to 6 %, with an average of 2.9 % between best and worst-performing SHE solutions. While these findings indicate that certain SHE solutions are more effective under specific conditions, this study does not establish a single universally optimal SHE solution set for a real EMU. The most suitable choice would likely depend on the particular operational profile, design constraints, and performance targets of the specific EMU application.

In summary, as initially hypothesized, the traction drive control system with the FOC system can reliably operate at low switching frequencies while staying within power converter loss limitations to avoid exceeding junction temperatures.

Additionally, it was established that SHE has a substantial advantage over synchronous PWM with the same equivalent frequency in terms of WTHD, power module losses, and motor losses. These differences are especially prominent at low switching-to-fundamental frequency ratios and under loaded conditions.

However, at high m_f ratios, the advantages of SHE diminish, making synchronous PWM easier to use. Moreover, at high numbers of eliminated harmonics, there are many unique solutions and angle calculations become a time-consuming process. The most significant effects of SHE were found with SHE 3, 5, and 7, with SHE 9 also being considered. However, with a higher number of switches, the advantages of SHE become negligible in this application, or synchronous PWM performs better, especially at low or no load.

The main novelty of this research is the development of a methodology for the creation, tuning, and testing of the traction drive FOC system with a hybrid PWM. Additionally, the research includes the development of an optimized Newton–Raphson method for solving the SHE/SHM problem for 2-/3-level inverters.

Future research could be extended to the following areas:

- Development of the selection criteria for transition points specific to power module/motor configurations.
- Optimization of the hybrid PWM transition scheme based not only on frequency but also on output torque.
- Selection of specific SHE solutions to further optimize WTHD, power module and motor losses.
- Emulation of EMU operation in a laboratory setup, as demonstrated by P. Fajri, V. Prabhala, and M. Ferdowsi in 2016 [108].

List of References

[1] 'Motor Catalogue', Alstom, Feb. 2015.

[2] 'Rail Vehicles | TSA - Traktionssysteme Austria', TSA. Accessed: Apr. 05, 2024. [Online]. Available: https://www.tsa.at/rail/

[3] 'Traction systems for locomotives and high-speed applications', ABB, 2018. Accessed: Jan. 26, 2024. [Online]. Available: https://library.e.abb.com/public/896cf517fcce4406b7a4facb6d6b7d0c/Traction_systems_high%20power_RevB_180916_web.pdf

[4] G. Abad, Ed., *Power electronics and electric drives for traction applications*. Chichester, West Sussex, United Kingdom: Wiley, 2017.

[5] S. P. Shenoy and O. Solis, 'Medium Voltage Integrated Drive and Motor', Calnetix Technologies, Cerritos, CA (United States), DOE-CALNETIX-7251, Mar. 2022. doi: 10.2172/1881305.

[6] S. P. Shenoy, J. Wei, and O. Solis, 'Silicon carbide power inverter/rectifier for electric machines', Calnetix Technologies, LLC, Cerritos, CA (United States), 10,910,957, Feb. 2021. Accessed: Jan. 22, 2024. [Online]. Available: https://www.osti.gov/biblio/1805485

[7] 'BORDLINE® CC750 DC_1500V For regional trains (EMU) with 1500 Vdc grid voltage', ABB, Product data sheet, Feb. 2020. Accessed: Apr. 05, 2024. [Online]. Available: https://search.abb.com/library/Download.aspx?DocumentID=3BHS262330%20ZAB%2005&LanguageCode=en&DocumentPartId=&Action=Launch

[8] M. Adamowicz and J. Szewczyk, 'SiC-Based Power Electronic Traction Transformer (PETT) for 3 kV DC Rail Traction', *Energies*, vol. 13, no. 21, Art. no. 21, Jan. 2020, doi: 10.3390/en13215573.

[9] 'EMU ELF2 Project Data Sheet.', Ingeteam, Jul. 2017. Accessed: Apr. 05, 2024. [Online]. Available: https://www.ingeteam.com/Portals/0/Catalogo/Sector/Documento/SSE_2793_Archivo_ref-t15-elf2-emu.pdf

[10] I. T. AG, 'Silicon Carbide (SiC) - Infineon Technologies'. Accessed: Apr. 05, 2024. [Online]. Available: https://www.infineon.com/cms/en/product/technology/silicon-carbide-sic/

[11] 'Silicon Carbide (SiC) Power Modules | Semikron Danfoss'. Accessed: Apr. 05, 2024. [Online]. Available: https://www.semikron-danfoss.com/innovation-technology/silicon-carbide-power-modules.html

[12] 'CoolSiC(TM) General presentation Part 2 - Why SiC from Infineon?', Infineon, Mar. 2024. Accessed: Apr. 08, 2024. [Online]. Available: https://www.infineon.com/cms/en/product/power/mosfet/silicon-carbide/

[13] C. S. Goli, S. Essakiappan, P. Sahu, M. Manjrekar, and N. Shah, 'Review of Recent Trends in Design of Traction Inverters for Electric Vehicle Applications', in *2021 IEEE 12th International Symposium on Power Electronics for Distributed Generation Systems (PEDG)*, Jun. 2021, pp. 1–6. doi: 10.1109/PEDG51384.2021.9494164.

[14] E. Robles, A. Matallana, I. Aretxabaleta, J. Andreu, M. Fernández, and J. L. Martín, 'The role of power device technology in the electric vehicle powertrain', *International Journal of Energy Research*, vol. 46, no. 15, pp. 22222–22265, 2022, doi: 10.1002/er.8581.

[15] Yole Development, ‘Power SiC 2022’, Product Brochure, 2022. Accessed: Apr. 05, 2024. [Online]. Available: https://medias.yolegroup.com/uploads/2022/03/Power-SiC-2022-Product_Brochure.pdf

[16] L. Diao, J. Tang, P. C. Loh, S. Yin, L. Wang, and Z. Liu, ‘An Efficient DSP–FPGA-Based Implementation of Hybrid PWM for Electric Rail Traction Induction Motor Control’, *IEEE Transactions on Power Electronics*, vol. 33, no. 4, pp. 3276–3288, Apr. 2018, doi: 10.1109/TPEL.2017.2707639.

[17] T. Jing, A. Maklakov, A. Radionov, V. Gasiyarov, and Y. Liang, ‘Formulations, Solving Algorithms, Existing Problems and Future Challenges of Pre-Programmed PWM Techniques for High-Power AFE Converters: A Comprehensive Review’, *Energies*, vol. 15, no. 5, Art. no. 5, Jan. 2022, doi: 10.3390/en15051696.

[18] J. Napoles, J. I. Leon, R. Portillo, L. G. Franquelo, and M. A. Aguirre, ‘Selective Harmonic Mitigation Technique for High-Power Converters’, *IEEE Transactions on Industrial Electronics*, vol. 57, no. 7, pp. 2315–2323, Jul. 2010, doi: 10.1109/TIE.2009.2026759.

[19] G. Nalcaci, D. Yildirim, I. Cadirci, and M. Ermis, ‘Selective Harmonic Elimination for Variable Frequency Traction Motor Drives Using Harris Hawks Optimization’, *IEEE Transactions on Industry Applications*, vol. 58, no. 4, pp. 4778–4791, Jul. 2022, doi: 10.1109/TIA.2022.3174828.

[20] ‘BORDLINE® CC750 MS (1 kVDC and 11 kVAC/16.7 Hz) Propulsion and auxiliary converter for dual-voltage multiple unit trains’, ABB, Product data sheet, 2012. Accessed: Apr. 05, 2024. [Online]. Available: https://library.e.abb.com/public/1219655d9aadccd7c1257a040063b32c/PDS%20BORDLINE%20CC750%20MS_3BHS262330%20ZAB%20E09%20Rev%20A.pdf

[21] J. Chivite-Zabalza, M. A. Rodríguez Vidal, P. Izurza-Moreno, G. Calvo, and D. Madariaga, ‘A Large Power, Low-Switching-Frequency Voltage Source Converter for FACTS Applications With Low Effects on the Transmission Line’, *IEEE Transactions on Power Electronics*, vol. 27, no. 12, pp. 4868–4879, Dec. 2012, doi: 10.1109/TPEL.2012.2192753.

[22] Janusz Biliński, Sylwester Buta, Emil Gmurczyk, and Jerzy Kaska, ‘Nowoczesny asynchroniczny napęd z hamowaniem odzyskowym produkcji MEDCOM do zmodernizowanych elektrycznych zespołów trakcyjnych serii EN57AKŁ’, MEDCOM, Apr. 2012. Accessed: Apr. 22, 2024. [Online]. Available: https://yadda.icm.edu.pl/baztech/element/bwmeta1.element.baztech-article-BPK6-0021-0081/c/Bilinski.pdf

[23] ‘BORDLINE® CC750 AC_15-25kV For regional trains (EMUs) with 15/25 kVac line voltage’, ABB, Product data sheet, Mar. 2018. Accessed: Apr. 05, 2024. [Online]. Available: https://library.e.abb.com/public/2a3a5170c8ed4550a661a6b1533ce968/BORDLINE%20CC750%20AC_15-25kV_M_700%20RevC%20EN.pdf

[24] A. Hughes, *Electric motors and drives: fundamentals, types, and applications*, Fourth Edition. Amsterdam: Elsevier/Newnes, 2013.

[25] H. Li and K. W. Klontz, ‘An investigation of current harmonic influence on induction motor in hybrid electric vehicle application’, in *2017 IEEE International Electric Machines and Drives Conference (IEMDC)*, May 2017, pp. 1–6. doi: 10.1109/IEMDC.2017.8002201.

[26] M. Steczek, P. Chudzik, and A. Szeląg, ‘Combination of SHE- and SHM-PWM Techniques for VSI DC-Link Current Harmonics Control in Railway Applications’, *IEEE Transactions on Industrial Electronics*, vol. 64, no. 10, pp. 7666–7678, Oct. 2017, doi: 10.1109/TIE.2017.2694357.

[27] J. I. Leon, S. Kouro, L. G. Franquelo, J. Rodriguez, and B. Wu, 'The Essential Role and the Continuous Evolution of Modulation Techniques for Voltage-Source Inverters in the Past, Present, and Future Power Electronics', *IEEE Transactions on Industrial Electronics*, vol. 63, no. 5, pp. 2688–2701, May 2016, doi: 10.1109/TIE.2016.2519321.

[28] A. Birda, J. Reuss, and C. M. Hackl, 'Simple Fundamental Current Estimation and Smooth Transition Between Synchronous Optimal PWM and Asynchronous SVM', *IEEE Transactions on Industrial Electronics*, vol. 67, no. 8, pp. 6354–6364, Aug. 2020, doi: 10.1109/TIE.2019.2938490.

[29] A. Birda, J. Reuss, and C. M. Hackl, 'Synchronous Optimal Pulsewidth Modulation for Synchronous Machines With Highly Operating Point Dependent Magnetic Anisotropy', *IEEE Trans. Ind. Electron.*, vol. 68, no. 5, pp. 3760–3769, May 2021, doi: 10.1109/TIE.2020.2984460.

[30] J. Holtz and N. Oikonomou, 'Estimation of the Fundamental Current in Low-Switching-Frequency High Dynamic Medium-Voltage Drives', *IEEE Transactions on Industry Applications*, vol. 44, no. 5, pp. 1597–1605, Sep. 2008, doi: 10.1109/TIA.2008.2002212.

[31] N. Mohan, T. M. Undeland, and W. P. Robbins, *Power electronics: converters, applications and design*, 3rd ed. Hoboken, NJ: John Wiley & Sons, 2003.

[32] D. G. Holmes and T. A. Lipo, *Pulse width modulation for power converters: principles and practice*. Hoboken, NJ: John Wiley, 2003.

[33] J.-S. Yim, S.-K. Sul, B.-H. Bae, N. R. Patel, and S. Hiti, 'Modified Current Control Schemes for High-Performance Permanent-Magnet AC Drives With Low Sampling to Operating Frequency Ratio', *IEEE Transactions on Industry Applications*, vol. 45, no. 2, pp. 763–771, Mar. 2009, doi: 10.1109/TIA.2009.2013600.

[34] R. P. Aguilera *et al.*, 'Closed-loop SHE-PWM technique for power converters through Model Predictive Control', in *IECON 2015 - 41st Annual Conference of the IEEE Industrial Electronics Society*, Nov. 2015, pp. 005261–005266. doi: 10.1109/IECON.2015.7392928.

[35] L. G. Franquelo, J. Napoles, R. C. P. Guisado, J. I. Leon, and M. A. Aguirre, 'A Flexible Selective Harmonic Mitigation Technique to Meet Grid Codes in Three-Level PWM Converters', *IEEE Transactions on Industrial Electronics*, vol. 54, no. 6, pp. 3022–3029, Dec. 2007, doi: 10.1109/TIE.2007.907045.

[36] D. Chatterjee, A. Szeląg, and M. Steczek, 'Analysis of disturbing effect of 3 kV DC supplied traction vehicles equipped with two-level and three-level VSI on railway signalling track circuits', *Bulletin of the Polish Academy of Sciences: Technical Sciences; 2017; 65; No 5 (Special Section on Multilevel Converters); 663-674*, 2017, Accessed: Apr. 05, 2024. [Online]. Available: https://journals.pan.pl/dlibra/publication/121389/edition/105775

[37] J. E. Huber and A. J. Korn, 'Optimized Pulse Pattern modulation for Modular Multilevel Converter high-speed drive', in *2012 15th International Power Electronics and Motion Control Conference (EPE/PEMC)*, Sep. 2012, pp. LS1a-1.4-1-LS1a-1.4-7. doi: 10.1109/EPEPEMC.2012.6397383.

[38] T. Geyer and N. Oikonomou, 'Model predictive pulse pattern control with very fast transient responses', in *2014 IEEE Energy Conversion Congress and Exposition (ECCE)*, Sep. 2014, pp. 5518–5524. doi: 10.1109/ECCE.2014.6954157.

[39] V. Spudic, T. Geyer, and N. Oikonomou, 'Optimized Pulse Patterns for Mmc Control', EP3142236A1, Mar. 15, 2017

[40] M. Sharifzadeh, H. Vahedi, A. Sheikholeslami, P.-A. Labbé, and K. Al-Haddad, 'Hybrid SHM–SHE Modulation Technique for a Four-Leg NPC Inverter With DC Capacitor Self-Voltage

Balancing', *IEEE Transactions on Industrial Electronics*, vol. 62, no. 8, pp. 4890–4899, Aug. 2015, doi: 10.1109/TIE.2015.2405059.

[41] M. Sharifzadeh *et al.*, 'Hybrid SHM-SHE Pulse-Amplitude Modulation for High-Power Four-Leg Inverter', *IEEE Transactions on Industrial Electronics*, vol. 63, no. 11, pp. 7234–7242, Nov. 2016, doi: 10.1109/TIE.2016.2538204.

[42] M. Sharifzadeh *et al.*, 'Hybrid SHM-PWM for Common-Mode Voltage Reduction in Three-Phase Three-Level NPC Inverter', *IEEE Journal of Emerging and Selected Topics in Power Electronics*, vol. 9, no. 4, pp. 4826–4838, Aug. 2021, doi: 10.1109/JESTPE.2020.3037283.

[43] H. S. Patel and R. G. Hoft, 'Generalized Techniques of Harmonic Elimination and Voltage Control in Thyristor Inverters: Part I–Harmonic Elimination', *IEEE Transactions on Industry Applications*, vol. IA-9, no. 3, pp. 310–317, May 1973, doi: 10.1109/TIA.1973.349908.

[44] H. S. Patel and R. G. Hoft, 'Generalized Techniques of Harmonic Elimination and Voltage Control in Thyristor Inverters: Part II — Voltage Control Techniques', *IEEE Transactions on Industry Applications*, vol. IA-10, no. 5, pp. 666–673, Sep. 1974, doi: 10.1109/TIA.1974.349239.

[45] J. N. Chiasson, L. M. Tolbert, K. J. McKenzie, and Z. Du, 'A complete solution to the harmonic elimination problem', *IEEE Transactions on Power Electronics*, vol. 19, no. 2, pp. 491–499, Mar. 2004, doi: 10.1109/TPEL.2003.823207.

[46] K. Yang, Z. Yuan, R. Yuan, W. Yu, J. Yuan, and J. Wang, 'A Groebner Bases Theory-Based Method for Selective Harmonic Elimination', *IEEE Transactions on Power Electronics*, vol. 30, no. 12, pp. 6581–6592, Dec. 2015, doi: 10.1109/TPEL.2014.2388077.

[47] J. N. Chiasson, L. M. Tolbert, K. J. McKenzie, and Z. Du, 'Elimination of harmonics in a multilevel converter using the theory of symmetric polynomials and resultants', *IEEE Transactions on Control Systems Technology*, vol. 13, no. 2, pp. 216–223, Mar. 2005, doi: 10.1109/TCST.2004.839556.

[48] M. I. Mohd Rashid, A. Hiendro, and M. Anwari, 'Optimal HE-PWM inverter switching patterns using differential evolution algorithm', in *2012 IEEE International Conference on Power and Energy (PECon)*, Dec. 2012, pp. 32–37. doi: 10.1109/PECon.2012.6450232.

[49] M. A. Memon, M. D. Siddique, S. Mekhilef, and M. Mubin, 'Asynchronous Particle Swarm Optimization-Genetic Algorithm (APSO-GA) Based Selective Harmonic Elimination in a Cascaded H-Bridge Multilevel Inverter', *IEEE Transactions on Industrial Electronics*, vol. 69, no. 2, pp. 1477–1487, Feb. 2022, doi: 10.1109/TIE.2021.3060645.

[50] Y. Jiang, X. Li, C. Qin, X. Xing, and Z. Chen, 'Improved Particle Swarm Optimization Based Selective Harmonic Elimination and Neutral Point Balance Control for Three-Level Inverter in Low-Voltage Ride-Through Operation', *IEEE Transactions on Industrial Informatics*, vol. 18, no. 1, pp. 642–652, Jan. 2022, doi: 10.1109/TII.2021.3062625.

[51] M. Steczek, W. Jefimowski, and A. Szeląg, 'Application of Grasshopper Optimization Algorithm for Selective Harmonics Elimination in Low-Frequency Voltage Source Inverter', *Energies*, vol. 13, no. 23, Art. no. 23, Jan. 2020, doi: 10.3390/en13236426.

[52] C. Buccella, C. Cecati, M. G. Cimoroni, and K. Razi, 'Analytical Method for Pattern Generation in Five-Level Cascaded H-Bridge Inverter Using Selective Harmonic Elimination', *IEEE Transactions on Industrial Electronics*, vol. 61, no. 11, pp. 5811–5819, Nov. 2014, doi: 10.1109/TIE.2014.2308163.

[53] A. Janabi, B. Wang, and D. Czarkowski, 'Generalized Chudnovsky Algorithm for Real-Time PWM Selective Harmonic Elimination/Modulation: Two-Level VSI Example', *IEEE*

Transactions on Power Electronics, vol. 35, no. 5, pp. 5437–5446, May 2020, doi: 10.1109/TPEL.2019.2945684.

[54] S. Padmanaban, C. Dhanamjayulu, and B. Khan, 'Artificial Neural Network and Newton Raphson (ANN-NR) Algorithm Based Selective Harmonic Elimination in Cascaded Multilevel Inverter for PV Applications', *IEEE Access*, vol. 9, pp. 75058–75070, 2021, doi: 10.1109/ACCESS.2021.3081460.

[55] S. Kouro, B. La Rocca, P. Cortes, S. Alepuz, B. Wu, and J. Rodriguez, 'Predictive control based selective harmonic elimination with low switching frequency for multilevel converters', in *2009 IEEE Energy Conversion Congress and Exposition*, Sep. 2009, pp. 3130–3136. doi: 10.1109/ECCE.2009.5316041.

[56] A. M. Hava, R. J. Kerkman, and T. A. Lipo, 'A high-performance generalized discontinuous PWM algorithm', *IEEE Transactions on Industry Applications*, vol. 34, no. 5, pp. 1059–1071, Sep. 1998, doi: 10.1109/28.720446.

[57] I. M. Alsofyani and K.-B. Lee, 'Simple Capacitor Voltage Balancing for Three-Level NPC Inverter Using Discontinuous PWM Method With Hysteresis Neutral-Point Error Band', *IEEE Transactions on Power Electronics*, vol. 36, no. 11, pp. 12490–12503, Nov. 2021, doi: 10.1109/TPEL.2021.3074957.

[58] H. Khan, 'Optimised space vector modulation for variable speed drives', phdthesis, Université Blaise Pascal - Clermont-Ferrand II, 2012. Accessed: Dec. 16, 2022. [Online]. Available: https://theses.hal.science/tel-00999475

[59] H. Neudorfer, 'Elektrische Bahnen Teil 1, Theorie', Technische Universität Darmstadt, Mar. 2021. Accessed: Apr. 26, 2024. [Online]. Available: https://www.ew.tu-darmstadt.de/media/ew/rd/ew_vorlesungen/lv_bahnen/Skript_EB_2021.pdf

[60] 'Europe rail electrification map'. Accessed: Apr. 29, 2024. [Online]. Available: https://commons.wikimedia.org/wiki/File:Europe_rail_electrification_en.svg

[61] 'Electric Multiple Units | NEWAG SA', Newag - en. Accessed: Apr. 24, 2024. [Online]. Available: https://www.newag.pl/en/offer/impuls/

[62] 'SKM - Tabor - Dane techniczne pojazdów - EZT 35 WE'. Accessed: Apr. 24, 2024. [Online]. Available: https://web.archive.org/web/20140301103132/http:/www.skm.warszawa.pl/ezt-35-we.html#

[63] 'Power Electronics for Public Transport Vehicles, EMUs & DMUs', MEDCOM, 2022. Accessed: Apr. 24, 2024. [Online]. Available: https://www.medcom.com.pl/do-pobrania

[64] 'Niskopodłogowy elektryczny zespół trakcyjny - 27WE', Pesa. Accessed: Apr. 24, 2024. [Online]. Available: https://zasoby.enkol.pl/prospekty/elf_skm.pdf

[65] 'Niskopodłogowy elektryczny zespół trakcyjny - ELF', Pesa. Accessed: Apr. 24, 2024. [Online]. Available: https://zasoby.enkol.pl/prospekty/elf_slask.pdf

[66] 'Ingetrac Power Converters - Medium Power', Ingeteam, Jun. 2018. Accessed: Apr. 24, 2024. [Online]. Available: https://www.ingeteam.com/en-us/railway-traction/traction-system/p18_35_586/ingetrac-traction-power-converters.aspx

[67] Tomáš Kuchta and Jaromír Pernička, 'RegioPanter EMUs', Jan. 2013. Accessed: Apr. 24, 2024. [Online]. Available: https://web.archive.org/web/20180122071857/http://railway-publish.com/upload/site1/files/ragiopanter.pdf

[68] M. Dudek, ‘Vývojové trendy trakčních motorů’, Bachelor Thesis, Západočeská univerzita v Plzni, 2014. Accessed: Apr. 24, 2024. [Online]. Available: http://dspace5.zcu.cz/handle/11025/14193

[69] ‘Civia trains’. Accessed: Apr. 24, 2024. [Online]. Available: https://www.renfe.com/es/en/renfe-group/renfe-group/fleet-of-trains/civia

[70] ‘Unidad S465 | Rodajes Cercanías Madrid’. Accessed: Apr. 24, 2024. [Online]. Available: https://www.renfe.com/es/es/cercanias/cercanias-madrid/rodajes/unidad-465

[71] Stadler, ‘Stadler wins tender for up to 510 FLIRT trains for Switzerland’, Oct. 2021. Accessed: Jul. 24, 2024. [Online]. Available: https://stadlerrail.com/media/pdf/2021_1005_media%20release_stadler%20wins%20tender%20for%20up%20to%20510%20flirt%20trains%20for%20switzerland_en.pdf

[72] Stadler, ‘More Capacity in Local and Long-Distance Transport: Öbb Orders Another 35 New Double-Decker Multiple Units From Stadler’, Stadler Rail. Accessed: Jul. 24, 2024. [Online]. Available: https://stadlerrail.com/en/media/article/more-capacity-in-local-and-long-distance-transport-oebb-orders-another-35-new-double-decker-multiple-units-from-stadler/1440/

[73] ‘Elektrischer Hochflurtriebzug FLIRT für PKP Intercity, Polen’, Stadler, Aug. 2014. Accessed: Apr. 24, 2024. [Online]. Available: https://web.archive.org/web/20160304193608/http://www.stadlerrail.com/media/uploads/F3PKP0814d.pdf

[74] ‘Elektrischer Niederflurtriebzug FLIRT für die Region Łódź , Polen’, Stadler, May 2013. Accessed: Apr. 24, 2024. [Online]. Available: https://web.archive.org/web/20160304111635/http://www.stadlerrail.com/media/uploads/F3L0513d.pdf

[75] ‘Elektrischer Doppelstocktriebzug KISS (Aeroexpress, Moskau)’, Stadler, May 2013. Accessed: Apr. 23, 2024. [Online]. Available: https://stadlerrail.com/media/pdf/kiss_ae0513d.pdf

[76] *IEC 60034-28:2012 Rotating electrical machines - Part 28: Test methods for determining quantities of equivalent circuit diagrams for three-phase low-voltage cage induction motors*, International Standard 60034–28, Dec. 13, 2012. Accessed: Apr. 25, 2024. [Online]. Available: https://webstore.iec.ch/publication/133

[77] F. Giri, Ed., *AC electric motors control: advanced design techniques and applications*. Chichester, West Sussex, United Kingdom: John Wiley & Sons Inc, 2013.

[78] A. Sciarretta and A. Vahidi, *Energy-Efficient Driving of Road Vehicles: Toward Cooperative, Connected, and Automated Mobility*. in Lecture Notes in Intelligent Transportation and Infrastructure. Cham: Springer International Publishing, 2020. doi: 10.1007/978-3-030-24127-8.

[79] V. Burenin, ‘Research and Development of Electrical Drive Control System for Electrical Vehicle in Urban Environment’, Master Thesis, Riga Technical University, 2020.

[80] В. Е. Розенфельд, *Теория электрической тяги*, 3rd ed. Москва: Транспорт, 1995.

[81] T. Ogawa, S. Manabe, G. Yoshikawa, Y. Imamura, and M. Kageyama, ‘Method of Calculating Running Resistance by the Use of the Train Data Collection Device’, *Quarterly Report of RTRI*, vol. 58, no. 1, pp. 21–27, 2017, doi: 10.2219/rtriqr.58.1_21.

[82] A. Wintrich, U. Nicolai, W. Tursky, and T. Reimann, *Application manual power semiconductors*, 2nd revised edition. Ilmenau: ISLE Verlag, 2015.

[83] ‘5SNA 0600G650100’. Nov. 2015. Accessed: Jun. 21, 2024. [Online]. Available: https://search.abb.com/library/Download.aspx?DocumentID=5SYA1558-04&LanguageCode=en&DocumentPartId=&Action=Launch

[84] ‘ABB Library - 5SNA 0600G650100_IGBT_XML’. Accessed: Jun. 21, 2024. [Online]. Available: https://library.abb.com/d/5SNA%200600G650100_IGBT_XML

[85] ‘ABB Library - 5SNA 0600G650100_Diode_XML’. Accessed: Jun. 21, 2024. [Online]. Available: https://library.abb.com/d/5SNA%200600G650100_Diode_XML

[86] S.-H. Kim, *Electric motor control: DC, AC, and BLDC motors*. 2017.

[87] А. С. Анучин, *Системы управления электроприводов*. Москва: МЭИ, 2015.

[88] D. Ronanki, S. A. Singh, and S. S. Williamson, ‘Comprehensive Topological Overview of Rolling Stock Architectures and Recent Trends in Electric Railway Traction Systems’, *IEEE Transactions on Transportation Electrification*, vol. 3, no. 3, pp. 724–738, Sep. 2017, doi: 10.1109/TTE.2017.2703583.

[89] M. Aguirre, C. Calleja, A. Lopez-de-Heredia, J. Poza, A. Aranburu, and T. Nieva, ‘FOC and DTC comparison in PMSM for railway traction application’, in *Proceedings of the 2011 14th European Conference on Power Electronics and Applications*, Aug. 2011, pp. 1–10. Accessed: Dec. 20, 2024. [Online]. Available: https://ieeexplore.ieee.org/document/6020397?denied=

[90] H. Hu and Y. Li, ‘Applications of induction motor drive based on DTC in railway traction’, in *Proceedings. International Conference on Power System Technology*, Oct. 2002, pp. 2285–2289 vol.4. doi: 10.1109/ICPST.2002.1047191.

[91] Y. Zhang and H. Yang, ‘Model Predictive Torque Control of Induction Motor Drives With Optimal Duty Cycle Control’, *IEEE Transactions on Power Electronics*, vol. 29, no. 12, pp. 6593–6603, Dec. 2014, doi: 10.1109/TPEL.2014.2302838.

[92] H. Miranda, P. Cortes, J. I. Yuz, and J. Rodriguez, ‘Predictive Torque Control of Induction Machines Based on State-Space Models’, *IEEE Transactions on Industrial Electronics*, vol. 56, no. 6, pp. 1916–1924, Jun. 2009, doi: 10.1109/TIE.2009.2014904.

[93] J. Holtz, ‘Pulsewidth modulation for electronic power conversion’, *Proceedings of the IEEE*, vol. 82, no. 8, pp. 1194–1214, Aug. 1994, doi: 10.1109/5.301684.

[94] B. Akin and M. Bhardwaj, ‘Sensored Field Oriented Control of 3-Phase Induction Motors’. Texas Instruments Incorporated, 2013.

[95] B. K. Bose, *Modern power electronics and AC drives*. Upper Saddle River, NJ: Prentice Hall, 2002.

[96] R. S. Burns, *Advanced control engineering*. Oxford ; Boston: Butterworth-Heinemann, 2001.

[97] T. Pérez Soriano and J. Fernández Martínez, ‘Low Speed Open Loop Field Oriented Control for Permanent Magnet Machines’, Master Thesis, Aalborg University, 2011. [Online]. Available: https://kbdk-aub.primo.exlibrisgroup.com/discovery/fulldisplay?docid=alma9921564406405762&context=L&vid=45KBDK_AUB:DDPB&lang=en&search_scope=Projekter&adaptor=Local%20Search%20Engine&tab=ProjekterSpecialer&query=any,contains,3954a0f4-9734-484d-b587-be63843b9840&offset=0

[98] M. P. Kaźmierkowski, R. Krishnan, and F. Blaabjerg, Eds., *Control in power electronics: selected problems*. in Academic Press series in engineering. Amsterdam ; New York: Academic Press, 2002.

[99] A. Anttila, L. Aarniovuori, M. Niemela, M. Zaheer, P. Lindh, and J. Pyrhonen, 'Active Power Analysis of PWM-driven Induction Motor in Frequency Domain', in *2021 XVIII International Scientific Technical Conference Alternating Current Electric Drives (ACED)*, Ekaterinburg, Russia: IEEE, May 2021, pp. 1–6. doi: 10.1109/ACED50605.2021.9462308.

[100] *IEC 61000-4-7:2002 Electromagnetic compatibility (EMC) - Part 4-7: Testing and measurement techniques - General guide on harmonics and interharmonics measurements and instrumentation, for power supply systems and equipment connected thereto*, 2002. Accessed: Jan. 13, 2023. [Online]. Available: https://webstore.iec.ch/publication/4226

[101] D. Tarnapowicz, T. Zaleski, Z. Matuszak, and M. Jaskiewicz, 'Energy Optimization of Marine Drive Systems with Permanent Magnet Synchronous Motors', *Energies*, vol. 17, no. 1, Art. no. 1, Jan. 2024, doi: 10.3390/en17010031.

[102] J. Bélanger, P. Venne, and J.-N. Paquin, 'The what, where, and why of real-time simulation.', Planet RT, 2010. [Online]. Available: https://blob.opal-rt.com/medias/L00161_0436.pdf

[103] 'Basics of Hardware-in-the-Loop simulation - MATLAB & Simulink - MathWorks Nordic'. Accessed: Apr. 03, 2023. [Online]. Available: https://se.mathworks.com/help/simscape/ug/what-is-hardware-in-the-loop-simulation.html

[104] 'What Is Hardware-in-the-Loop?' Accessed: Apr. 03, 2023. [Online]. Available: https://www.ni.com/en/solutions/transportation/hardware-in-the-loop/what-is-hardware-in-the-loop-.html

[105] K. Etzold *et al.*, 'Function Development With an Electric-Machine-in-the-Loop Setup: A Case Study', *IEEE Transactions on Transportation Electrification*, vol. 5, no. 4, pp. 1419–1429, Dec. 2019, doi: 10.1109/TTE.2019.2952288.

[106] 'OP4510 Compact Desktop - Hardware Products Documentation - Confluence'. Accessed: Apr. 03, 2023. [Online]. Available: https://opal-rt.atlassian.net/wiki/spaces/PHDGD/pages/144687790/OP4510+Compact+Desktop

[107] ABB, 'Drive Low Voltage General Purpose Motors: Aluminium motor section'. ABB, Sep. 2003. Accessed: Jul. 18, 2024. [Online]. Available: https://library.e.abb.com/public/2652441d9397714dc1257b1300571151/General%20Purpose%20Motors%20Aluminium%20GB%20092003.pdf

[108] P. Fajri, V. A. K. Prabhala, and M. Ferdowsi, 'Emulating On-Road Operating Conditions for Electric-Drive Propulsion Systems', *IEEE Transactions on Energy Conversion*, vol. 31, no. 1, pp. 1–11, Mar. 2016, doi: 10.1109/TEC.2015.2481180.

Appendix A : SHE solutions for 3-level inverter

The algorithm applied to the 3-level inverter SHE/SHM problem employs the same fundamental principles as the 2-level version, although the quarter-wave symmetrical coefficients of the FFT function differ slightly, as outlined in the equation below:

$$\begin{cases} \frac{4}{n_1\pi}[\cos(n_1\alpha_1) - \cos(n_1\alpha_2) + \cdots \mp \cos(n_1\alpha_N)] = M_1 \\ \frac{4}{n_2\pi}[\cos(n_2\alpha_1) - \cos(n_2\alpha_2) + \cdots \mp \cos(n_2\alpha_N)] = 0 \\ \vdots \\ \frac{4}{n_N\pi}[\cos(n_N\alpha_1) - \cos(n_N\alpha_2) + \cdots \mp \cos(n_N\alpha_N)] = 0 \end{cases}$$

The comprehensive derivation of this function and its partial derivatives is omitted here, given that the 3-level inverter is not the primary focus of this research. A full description can be found in foundational literature on harmonic elimination [43].

After executing the algorithm, the solutions identified for the 3-level inverter are summarized in Table A.1.

Table A.1 Number of Solutions for 3-Level Inverter

SHE angles	Number of solution ranges
3	2
5	4
7	7
9	13
11	21
13	>30

A notable distinction in solution ranges between the 2-level and 3-level inverter SHE problems is evident. While the 2-level inverter exhibits continuous solutions across the entire modulation index range ($m_1 = 0.01 - 1.15$), the 3-level inverter typically presents only one continuous solution for the entire range, with others being partial. Table A.2 through Table A.6 detail the solution ranges for each analysed SHE variation.

Table A.2 SHE 3 Solution Ranges

Solution number	Solution range
1	0.01–1.15
2	0.65–1.15

Table A.3 SHE 5 Solution Ranges

Solution number	Solution range
1	0.01–1.15
2	0.01–0.62 (T)
3	0.657–0.999
4	0.674–1.15

Table A.4 SHE 7 Solution Ranges

Solution number	Solution range	Solution number	Solution range
1	0.01–1.15	5	0.729–1.15
2	0.01–0.633 (T)	6	0.589–0.595
3	0.639–1.15	7	0.661–0.898
4	0.658–1.15		

Table A.5 SHE 9 Solution Ranges

Solution number	Solution range	Solution number	Solution range
1	0.01–1.15	8	0.595–1.04
2	0.01–0.586 (T)	9	0.596–0.605
3	0.01–0.589	10	0.596–0.638 (T)
4	0.01–0.641 (T)	11	0.661–1.031
5	0.671–1.15 (1)	12	0.663–0.842 (T)
6	0.671–1.15 (2)	13	0.802–0.870
7	0.775–1.15		

Table A.6 SHE 11 Solution Ranges

Solution number	Solution range	Solution number	Solution range
1	0.01–1.15	12	0.602–0.644 (Tx2)
2	0.01–0.5926 (T)	13	0.602–0.868
3	0.01–0.597	14	0.603–0.612
4	0.01–0.647 (T)	15	0.662–0.949
5	0.582–1.15	16	0.664–0.809 (T)
6	0.600–1.15	17	0.664–0.835
7	0.661–1.15	18	0.868–0.957
8	0.706–1.15	19	0.5834–0.5996
9	0.707–1.15	20	0.5834–0.5856
10	0.813–1.15	21	0.5838–0.5854 (T)
11	0.826–1.15		

Here, (T) denotes a “twisted” solution, characterized by a single continuous solution range that comprises multiple angle value sets for a given modulation index. Examples of such solutions are

depicted in Fig. A.1 (a) and (c). Other solution ranges, as shown in Fig. A.1 (b) and (d) are highly non-linear.

Particularly at higher SHE levels, some solutions appear only within very narrow modulation index ranges, such as SHE 9 solution 9 or the even narrower SHE 11 solutions 19–21. Only one solution range for each analysed SHE variation remains fully continuous across the entire modulation index range, as demonstrated in Fig. A.2 through Fig. A.5.

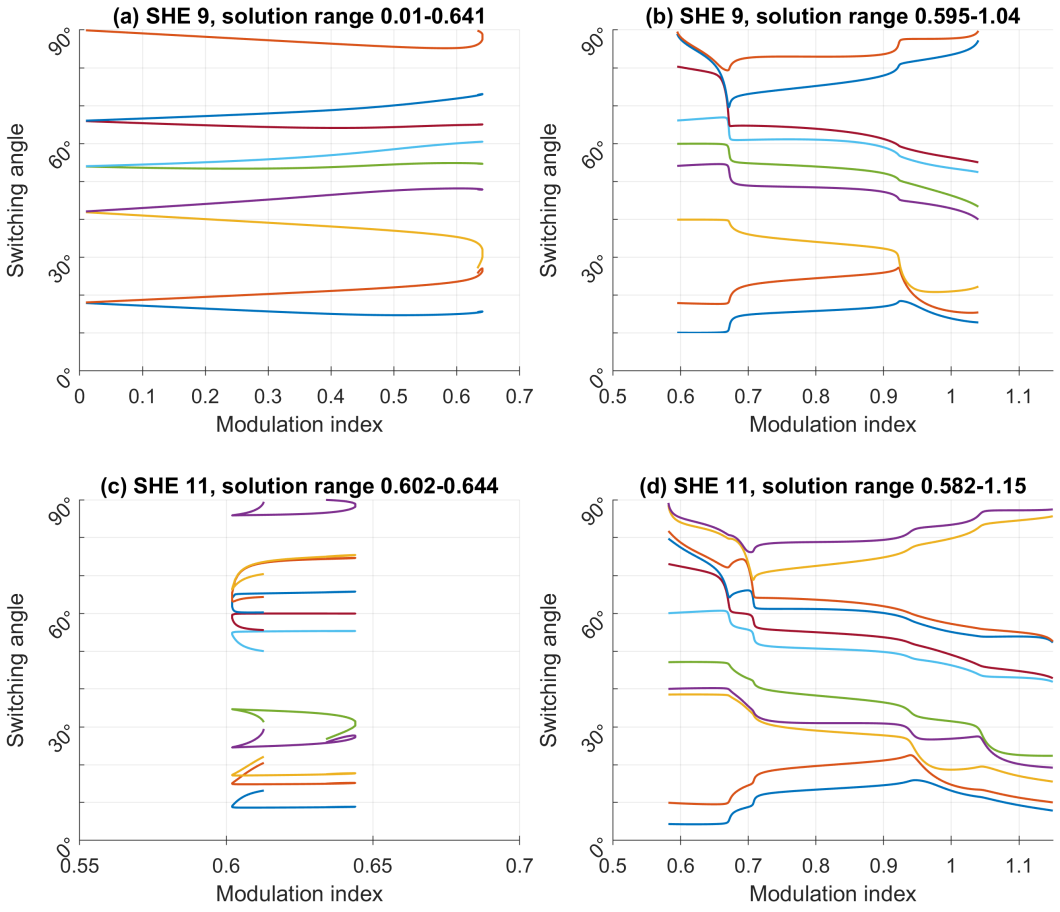

Fig. A.1. Twisted and non-linear solution ranges for (a), (b) SHE 9 and (c), (d) SHE 11.

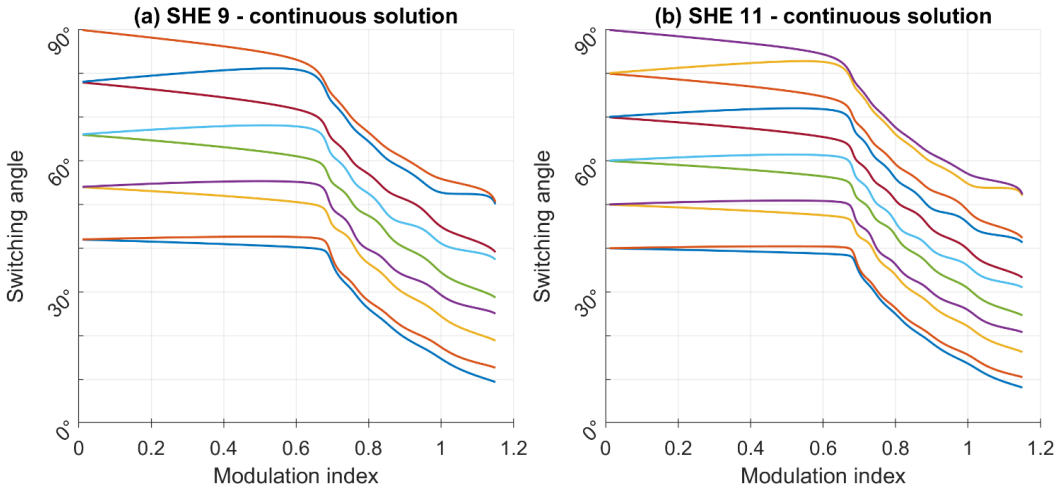

Fig. A.2. Continuous solution ranges for (a) SHE 9 and (b) SHE 11.

The narrower solutions are generally impractical for real-world applications, and the twisted solutions complicate interpolation efforts due to the indeterminacy they introduce when multiple points on the modulation index lead to differing outputs.

Fig. A.3, Fig. A.4, and Fig. A.5 represent different sets of unique solutions for SHE 3 and SHE 4. Each figure illustrates two solution ranges for each SHE scenario, showing both the single pulse train period and the harmonic content of the pulse train at a reference point modulation index.

Although solutions for SHE 7 through SHE 13 have been identified, they are not included due to the complexity of presenting many solutions.

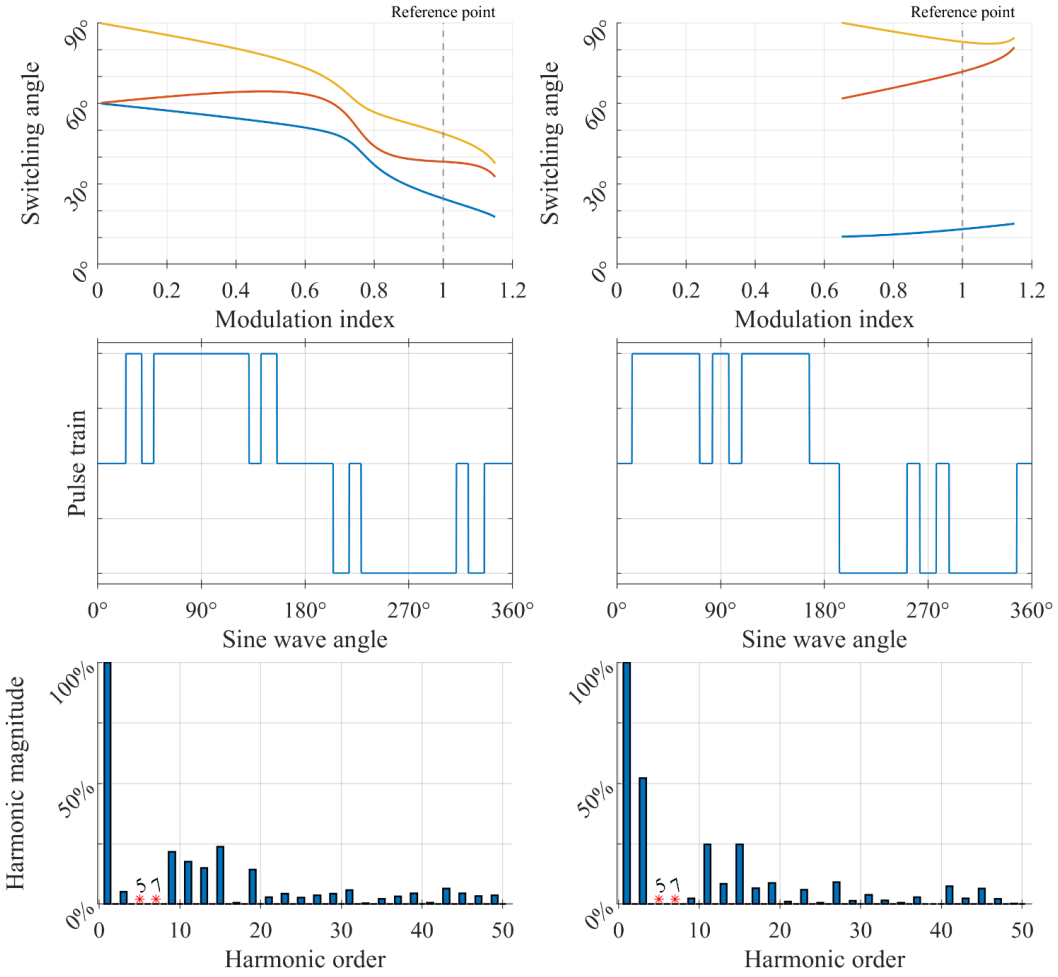

Fig. A.3. Solution ranges for SHE 3, pulse train and FFT.

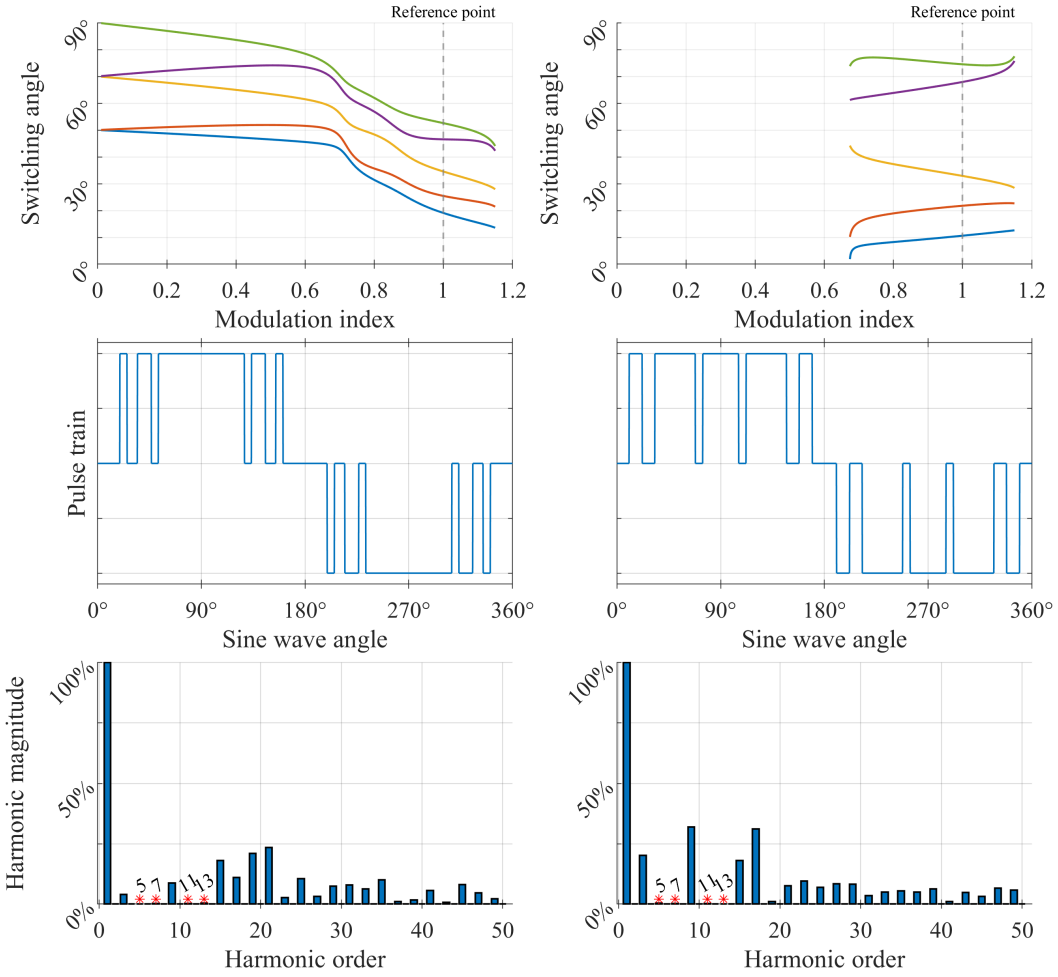

Fig. A.4. Solution ranges for SHE 5, pulse train and FFT (1).

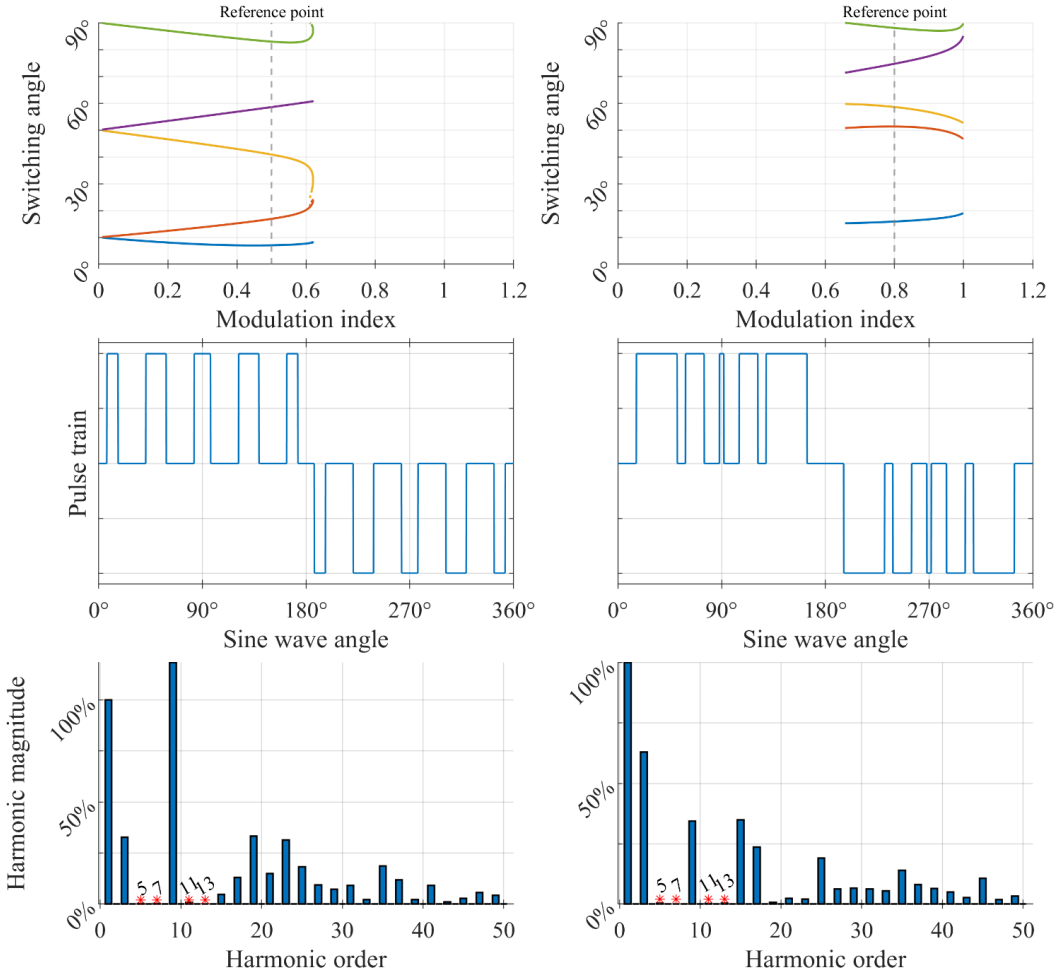

Fig. A.5. Solution ranges for SHE 5, pulse train and FFT (2).

The harmonic analysis of these pulse trains (corresponding to phase voltage) consistently verifies the complete elimination of targeted harmonics, similar to the 2-level problem. Typically, the harmonic immediately following the highest eliminated one shows an increase, which is expected.

For performance metrics, the settings detailed in Chapter 1.5.1 were employed to allow for a fair comparison. However, the actual solution values presented were calculated with a higher resolution (0.002 instead of 0.01) to accurately capture the highly non-linear nature of many 3-level solutions.

Table A.7 3-Level SHE Problem Solving Performance

SHE angles	Computation time, s	Total num. iterations	Total num. fcn eval-s	Median num. iterations	Mean num. iterations	Standard deviation
3	9.1	23’970	409’049	1	1.05	0.23
5	22.7	37’974	1’307’362	1	1.66	1.18
7	62.7	171’933	8’082’741	5	7.51	7.99
9	201.6	1’013’082	50’087’626	27	44.24	52.20
11	1630.5	7’730’167	384’378’602	233	337.56	306.65
13	4643.3	18’505’053	916’366’488	1001	808.08	312.14

Performance metrics indicate a higher number of iterations compared to the 2-level system (referenced in Table 1.6), suggesting that more guesses and/or iterations are necessary to converge to a viable solution. Convergence and success rates, detailed in Table A.8, show slightly lower convergence for the 3-level system. The success rate, particularly at higher SHE levels, is challenging to precisely determine since nearly all solutions are partial and many exist within very narrow ranges, thus the reported success rate is approximate.

Table A.8 Convergence and Success Rate for a 3-Level SHE Problem

# SHE angles	Convergence rate	Success rate
3	100.0 %	100.0 %
5	100.0 %	100.0 %
7	100.0 %	100.0 %
9	100.0 %	100.0 %
11	91.5 %	≈ 99.8 %
13	85.4 %	≈ 99.1 %

Appendix B : Modelled current waveforms

Stator current waveforms at different speeds, loads and in different regimes of PWM modulation.

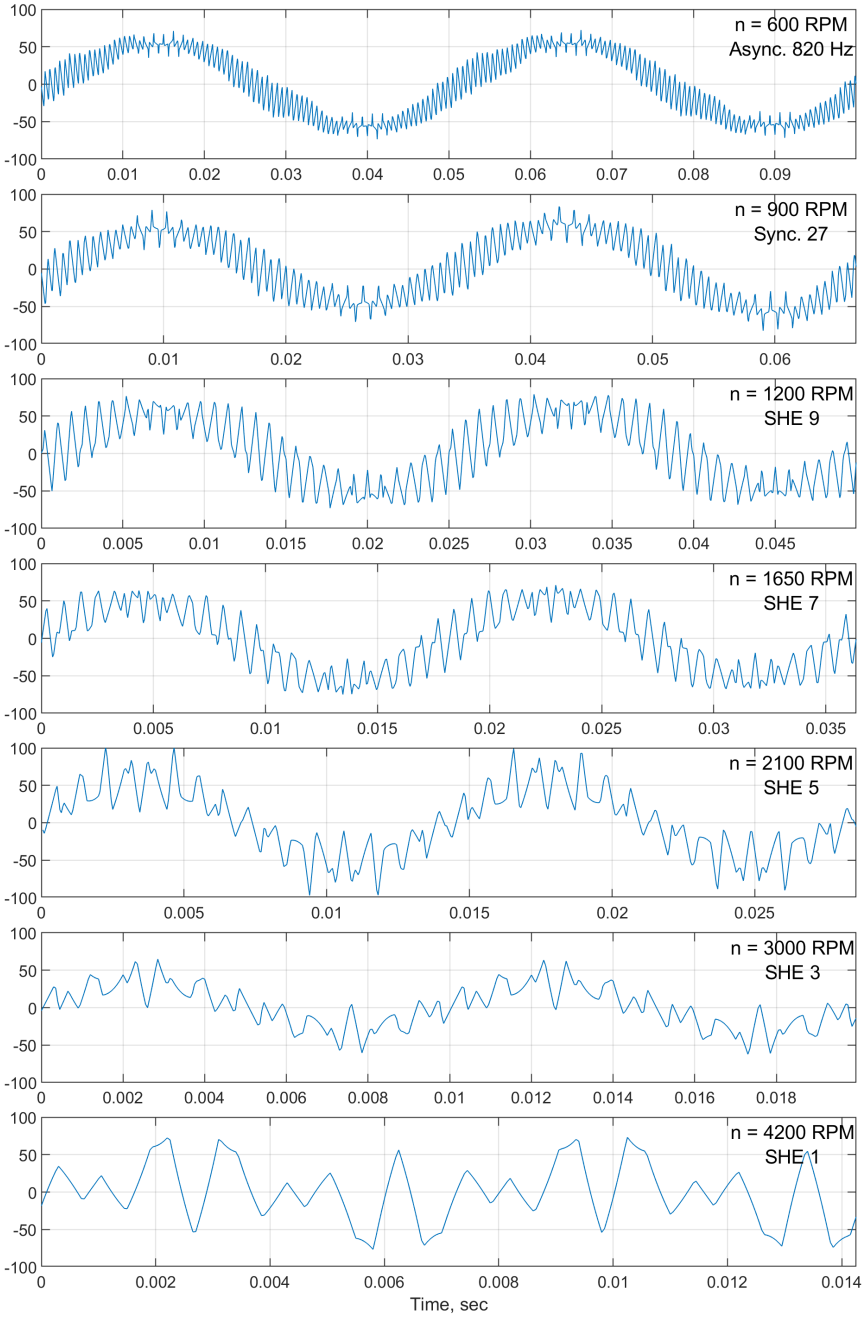

Fig. B.1. Stator current waveforms, no-load.

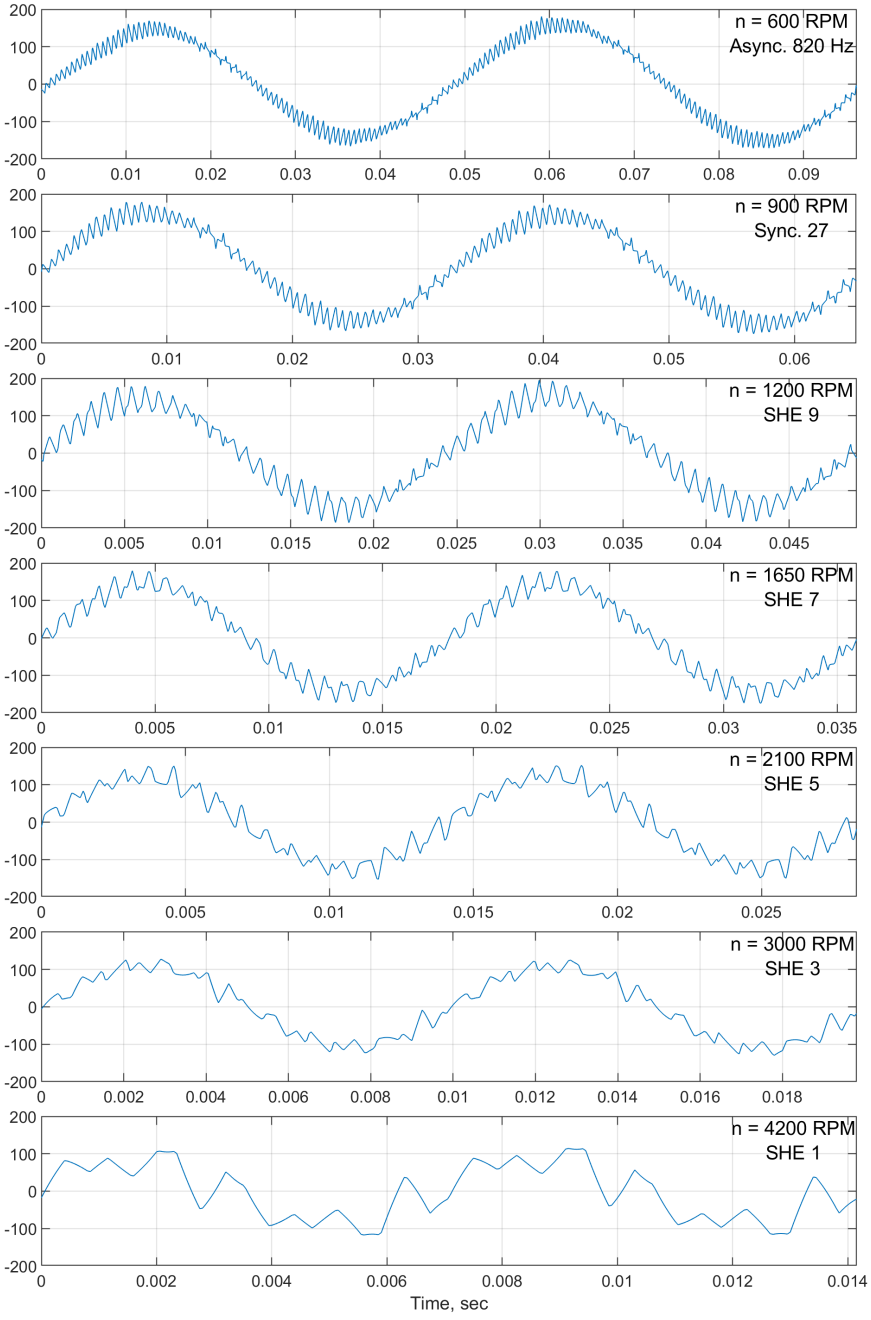

Fig. B.2. Stator current waveforms, 0.5 of traction characteristic load.

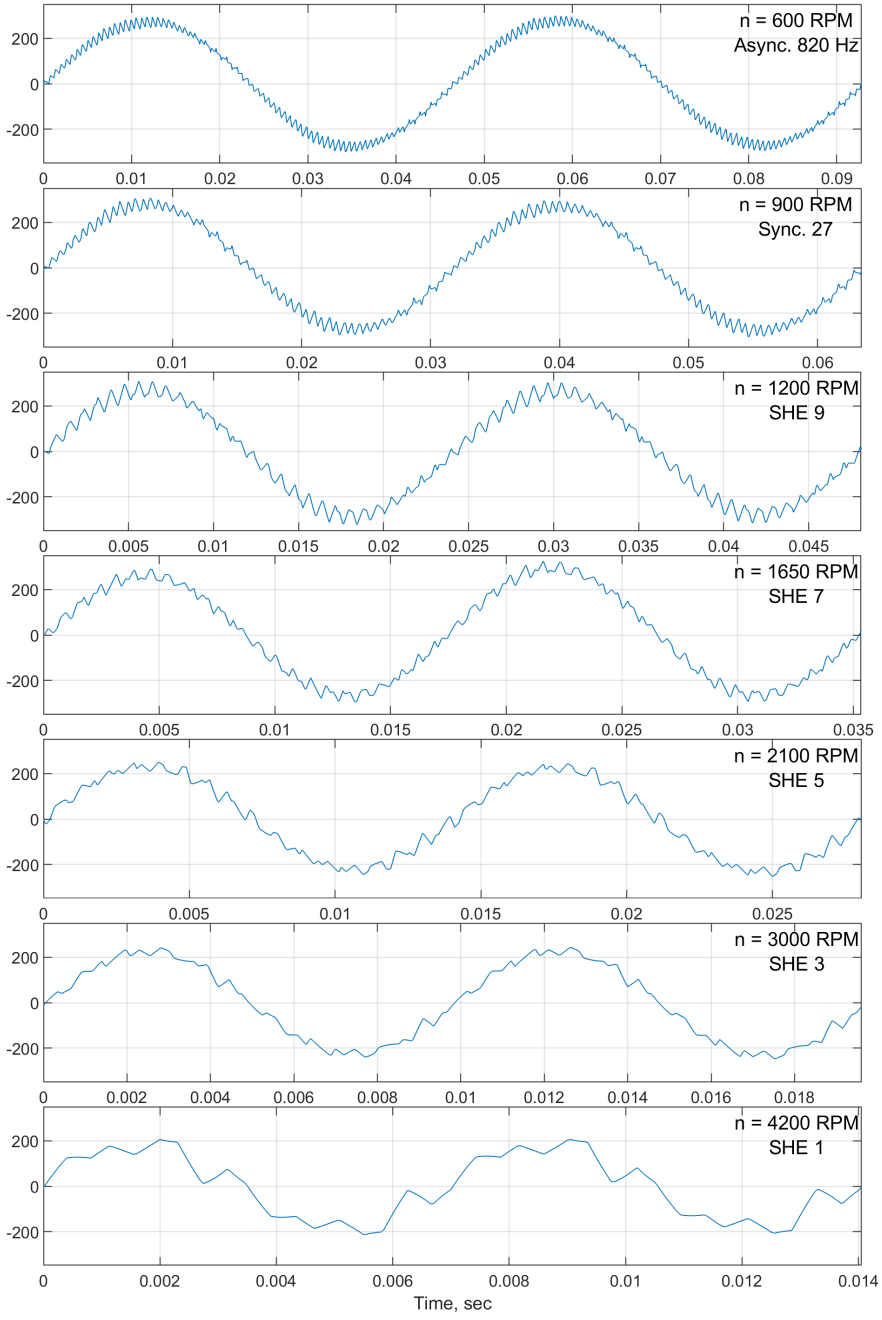

Fig. B.3. Stator current waveforms, traction characteristic load.

Appendix C : Laboratory equipment

Laboratory testing is done at the premises of RTU. Below in the Table C.1 is the list of laboratory equipment.

Table C.1 Laboratory Equipment

Name of laboratory equipment	**Type**	**Measuring range**
Real-time simulator	OPAL OP4510	Multirange
Inverter	Danfoss VLT 5004 3x380 Vin	Multirange
Torque meter	UTM II – 20 Nm	Rated 0…±20 Nm
Voltage sensor board	LV 25-600	0…±900 V
Current sensor	LA 55-P	0…±70 A
Micro-ohmmeter	MPK 253	0…200 Ohm
Digital oscilloscope	Rigol DC4012	Multirange
Power supply	EA-PS 8032-10 T	0…32 V 0…10 A
Rotary encoder	Scancon 2RHF2048-D-5M-S	2048 ppr, 12000 RPM max

Appendix D : Measured current waveforms

Stator current waveforms at different speeds, loads and in different regimes of PWM modulation.

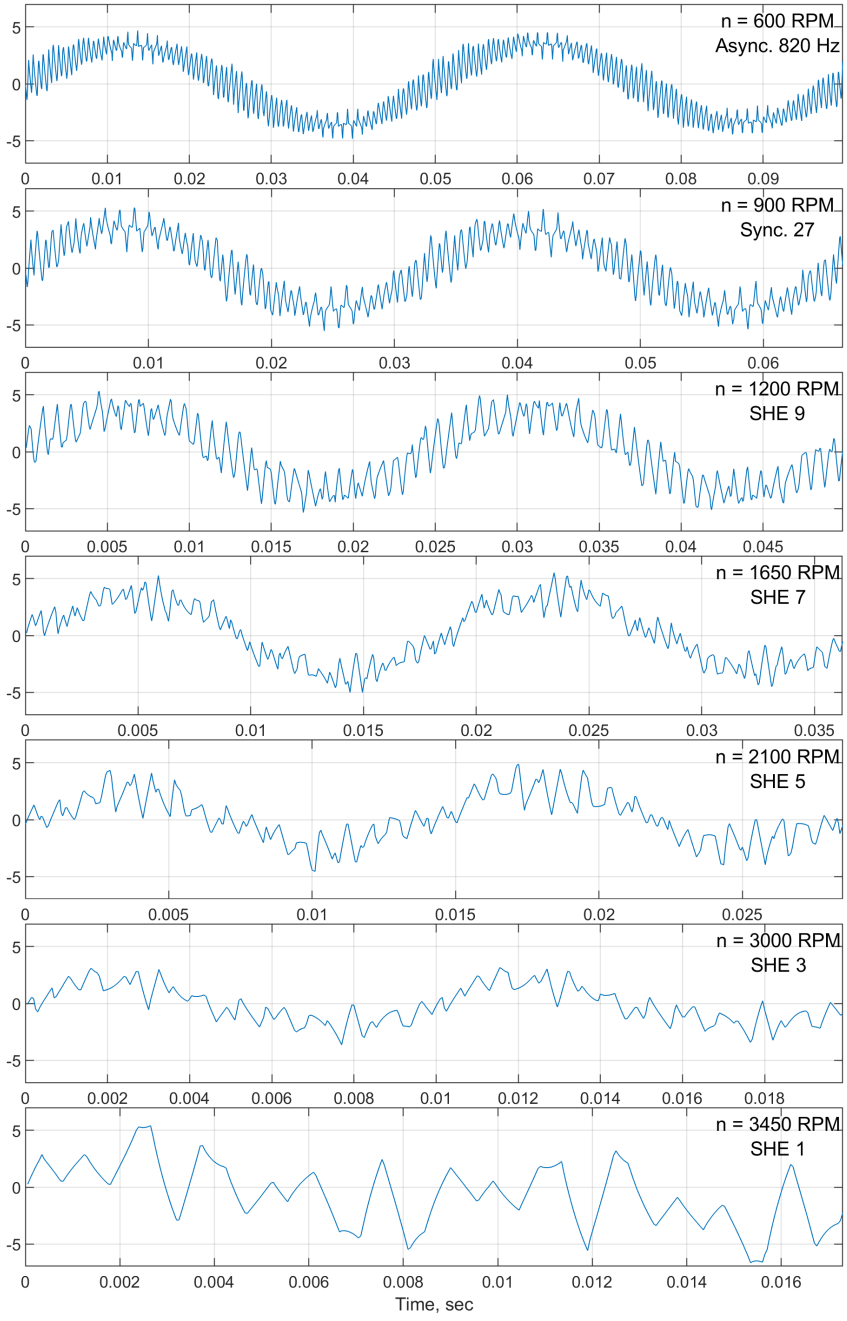

Fig. D.1. Stator current waveforms, no-load.

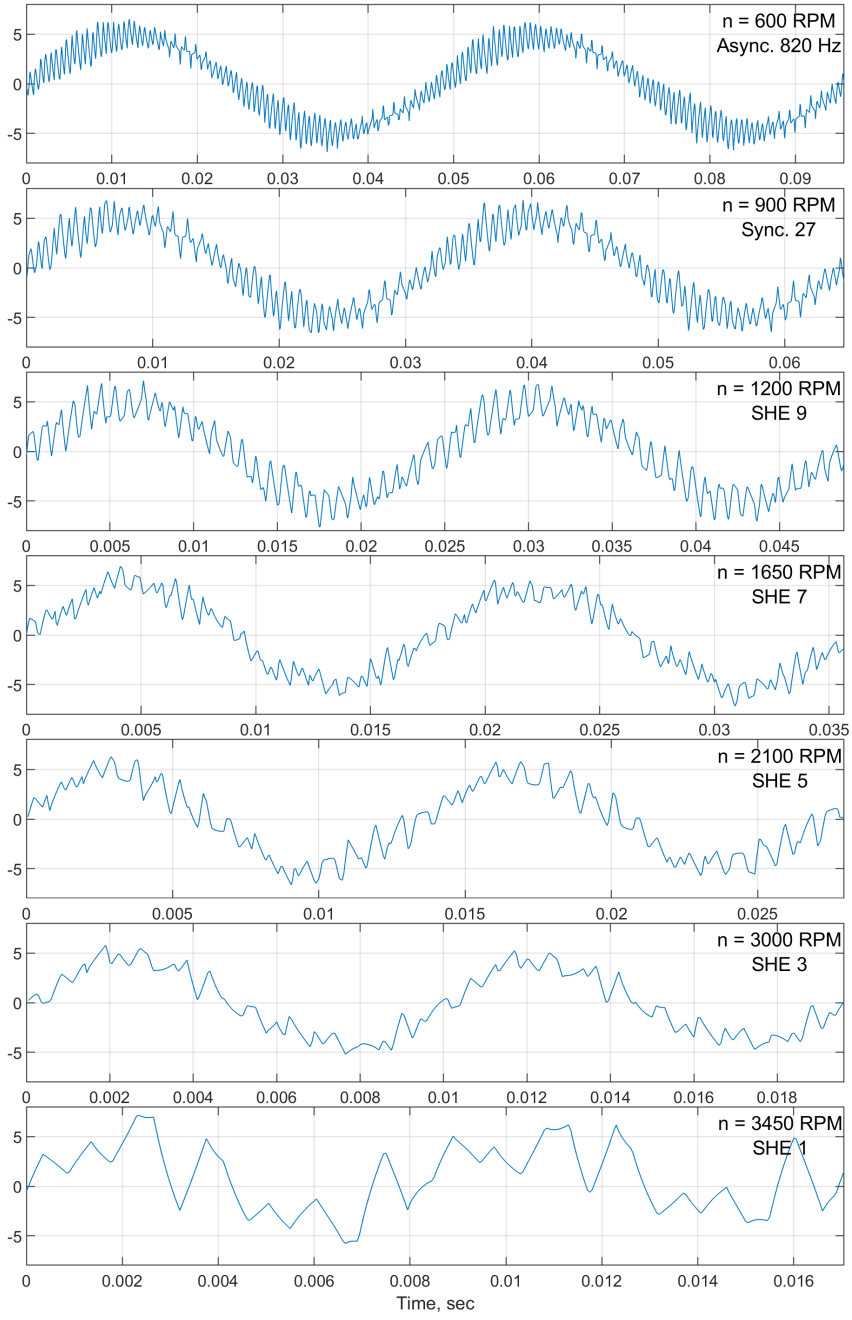

Fig. D.2 . Stator current waveforms, 0.5*0.75 of traction characteristic load.

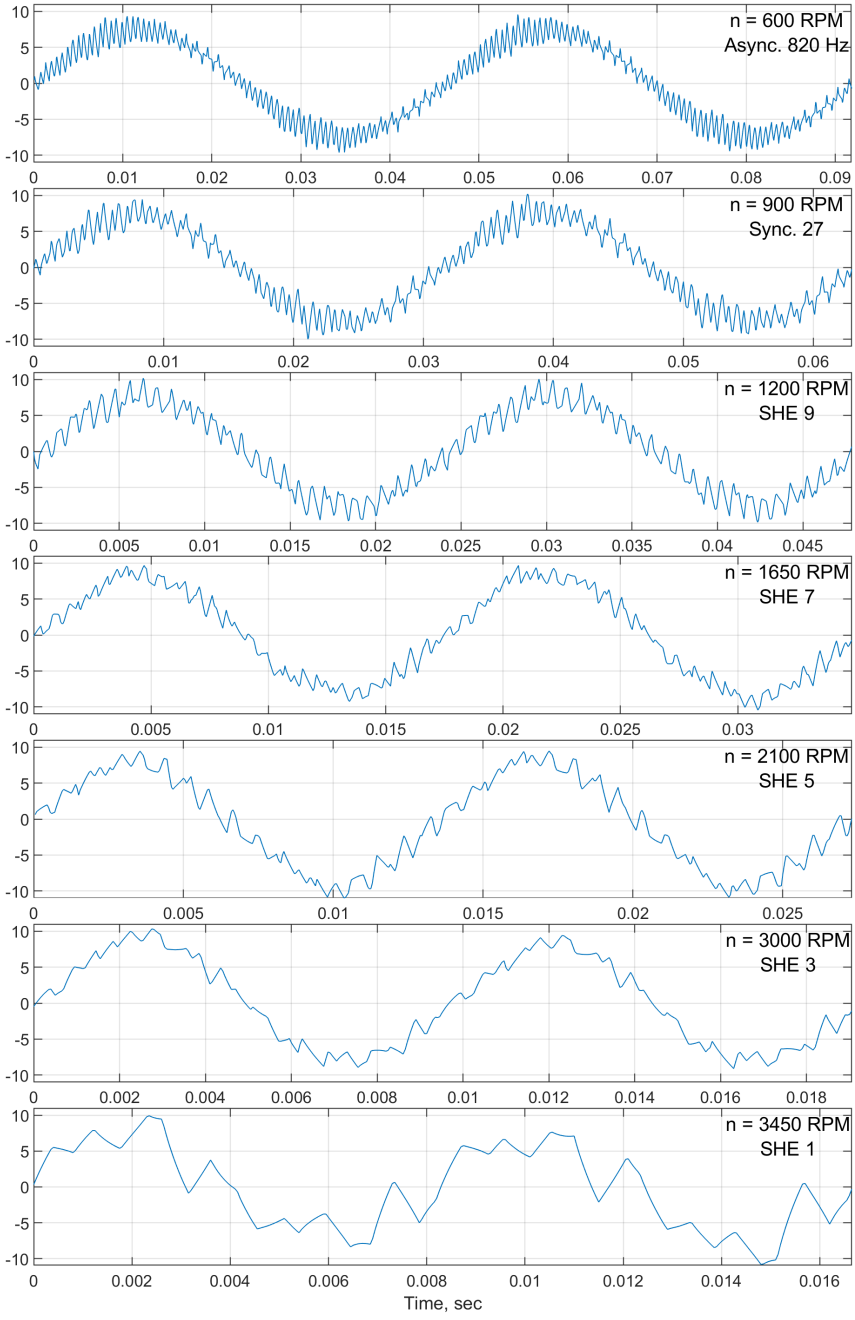

Fig. D.3. Stator current waveforms, 0.75 of traction characteristic load.

Vsevolod Burenin was born in 1996 in Pskov, Russia. He received a degree of Bachelor of Engineering (2018) and a degree of Master of Engineering (2020) in Electrical Engineering from Riga Technical University, Riga, Latvia. Since 2019, he has been employed as a software engineer in the Department of Power Electronics at JSC "Riga Electrical Machinery Factory". His research interests include the design, control, and testing of electrical motors and traction drives.